WROCŁAW UNIVERSITY
OF SCIENCE AND TECHNOLOGY

DOCTORAL THESIS

Statistical modelling of corneal OCT speckle

Marcela NIEMCZYK

Supervisors:
D. Robert ISKANDER
David ALONSO CANEIRO

Wrocław University
of Science and Technology

European Funds
Knowledge Education Development

Wrocław University
of Science and Technology

European Union
European Social Fund

Doctoral thesis co-financed by the European Union
under the European Social Fund,
project no POWR.03.02.00-00-I003/16D.

"The journey of a thousand miles begins with a single step."

Lao Tzu

Abstract

The goal of this thesis is to propose methods of the statistical analysis of corneal optical coherence tomography (OCT) speckle and validate their usability for detection of changes in corneal properties connected with intraocular pressure (IOP). Two approaches to speckle analysis, parametric and non-parametric, are considered in this work. The parametric approach involves estimation of distributional parameters based on pixel values in OCT images. A set of eight distributions is analyzed in terms of fitting to empirical distribution of pixel values. In the non-parametric approach three statistical distances are proposed to compare empirical distribution of speckle amplitude with benchmark Rayleigh distribution with constant value of its scale parameter. Also, values of contrast ratio are considered in this approach. The described methods of speckle analysis are presented on OCT images from three studies. The first study is performed on phantoms made of epoxy resin, containing different concentrations of scattering particles. The second study includes two experiments *ex-vivo* on porcine eyeballs. In the first experiment eyeballs are subjected to increasing IOP. The second experiment is analogous but with IOP maintained at a constant level. In the third study human corneas are examined *in-vivo* using OCT and IOP is also measured. The relation between speckle statistics and concentration of scattering particles in examined medium is evaluated in the phantom study. In the study on porcine and human corneas, speckle statistics are linked to changes in IOP, which is supposed to affect corneal properties. Additionally, the thesis considers corneal speckle analysis using spatial maps of gamma distribution parameters. The influence of OCT images averaging on speckle parameters is also examined incorporating both the statistics of speckle as well as background noise. Based on these results, a new theoretical model of speckle amplitude is calculated as a product distribution of two gamma random variables. Summarizing, this work presents different approaches to statistical analysis of corneal OCT speckle and shows that they give similar results when changes in IOP are considered. It can be concluded that the development of such methods should head towards simplifying them rather than making them overly complicated.

Streszczenie

Celem niniejszej pracy jest zaproponowanie metod statystycznej analizy szumu plamkowego na obrazach optycznej tomografii koherencyjnej (OCT) rogówki oka oraz ich zastosowanie w celu wykrywania zmian właściwości rogówki wywołanych przez wzrost ciśnienia wewnątrzgałkowego (IOP). Przedstawione zostały dwa podejścia do analizy szumu plamkowego: parametryczne oraz nieparametryczne. W pierwszym z nich dla wartości pikseli na obrazach OCT rogówki estymowane są parametry ośmiu rozkładów prawdopodobieństwa, wybranych na podstawie literatury. Oceniane jest także dopasowanie tych rozkładów do empirycznego rozkładu wartości pikseli. Z kolei w podejściu nieparametrycznym zaproponowane zostały trzy miary odległości pomiędzy empirycznym rozkładem wartości pikseli na obrazie OCT a teoretycznym modelem, będącym rozkładem Rayleigha o stałej wartości parametru skali. Ponadto, analizowane są również wartości współczynnika kontrastu, obliczone na podstawie wartości pikseli na obrazie. Zaproponowane metody zastosowane zostały do analizy szumu plamkowego na obrazach OCT pochodzących z trzech badań. W pierwszym z nich obrazowane były fantomy przygotowane z żywicy epoksydowej zmieszanej z cząsteczkami niebieskiego barwnika w różnych stężeniach. W drugim badaniu przeprowadzone zostały dwa eksperymenty na świńskich gałkach ocznych *ex-vivo*. Gałki te poddawane były kontrolowanemu wzrostowi IOP w pierwszym eksperymencie, natomiast w drugim wszystkie procedury były analogiczne, jedynie ciśnienie w gałkach ocznych utrzymywane było cały czas na stałym poziomie. W ostatnim badaniu analizowane były obrazy OCT rogówki oczu ludzkich *in-vivo*. Eksperyment z wykorzystaniem fantomów umożliwił ocenę zależności pomiędzy parametrami statystycznymi szumu plamkowego a stężeniem cząsteczek rozpraszających. Badania na oczach świńskich i ludzkich pozwoliły natomiast na zbadanie wpływu IOP na zmiany parametrów szumu plamkowego. Na podstawie obrazów świńskich rogówek przygotowane zostały mapy wartości parametrów rozkładu gamma. Dodatkowo przeprowadzona została również analiza wpływu uśredniania obrazów OCT rogówki na statystykę szumu plamkowego oraz szumu tła. Na podstawie uzyskanych wyników zaproponowany został teoretyczny model szumu plamkowego, będący iloczynem dwóch zmiennych o rozkładzie gamma. Ponieważ wszystkie przedstawione w pracy podejścia dały zbliżone rezultaty, uzasadnione jest zatem w analizie statystycznej szumu plamkowego na obrazach OCT rogówki kierowanie się w stronę jak najprostszych metod.

Acknowledgements

First, I would like to express my deepest gratitude to my first supervisor, D. Robert Iskander, for making my PhD a fantastic adventure. Developing my ideas would not be possible without his guidance as well as support and endless enthusiasm at every moment. Also, I would like to specially thank my co-supervisor David Alonso Caneiro for his valuable advice, mentoring during an internship, and his help whenever I needed it.

I would like to thank all members of the Biomedical Signal Processing Group for sharing their knowledge and discussions about everything. Special thanks to Dominika Sułot for all our common experiences and for being a great companion in this adventure.

I would like to warmly thank all my family for being my source of energy. I am extremely grateful to my parents for their constant support in every life decision and for helping me as much as possible. Thanks to my sister for being my best friend. Most of all, I would like to thank my husband. Without his tremendous understanding and encouragement, it would be impossible for me to complete my PhD.

In the end, I would also like to thank my cats, for providing me during my work on PhD thesis regular breaks filled with purring.

List of publications

Journal articles

1. M. E. Danielewska, M. A. Kostyszak, P. Sareło, M. Gąsior-Głogowska, **M. Niemczyk**, P. Prządka, A. Antończyk, Z. Kiełbowicz, and D.R. Iskander, "Indirectly assessing changes in corneal properties with OCT speckle after crosslinking in porcine eyes," *Experimental Eye Research*, vol. 219, pp. 109051, 2022.

2. **M. Niemczyk** and D. R. Iskander, "Statistical analysis of corneal OCT speckle: a non-parametric approach," *Biomedical Optics Express*, vol. 12, pp. 6407–6421, 2021.

3. **M. Niemczyk**, M. E. Danielewska, M. A. Kostyszak, D. Lewandowski, and D. R. Iskander, "The effect of intraocular pressure elevation and related ocular biometry changes on corneal OCT speckle distribution in porcine eyes," *PLoS One*, vol. 16, pp. e0249213, 2021.

Conference proceedings

1. **M. Niemczyk**, "Bootstrap model selection for estimating the sum of exponentially damped sinusoids," *Innovations and developments of technologies in medicine, biology and healthcare. Proceedings of the IEEE EMBS International Student Conference (ISC)*, vol. 1360, pp. 79–86, 2021.

2. **M. Niemczyk**, M. E. Danielewska, M. A. Kostyszak, and D. R. Iskander, "The influence of IOP on the correlation of corneal speckle parameters in ex-vivo inflation experiment on porcine eyes,", Annual Meeting of the Association for Research in Vision and Ophthalmology (ARVO), *Investigative Ophthalmology & Visual Science*, vol. 62, pp. 2019, 2021.

3. **M. Niemczyk**, M. A. Kostyszak, M. E. Danielewska, and D. R. Iskander, "Influence of intraocular pressure on corneal OCT speckle distribution. An animal ex-vivo study,", Annual Meeting of the Association for Research in Vision and Ophthalmology (ARVO), *Investigative Ophthalmology & Visual Science*, vol. 61, pp. 4712, 2020.

4. M. A. Kostyszak, M. E. Danielewska, **M. Niemczyk**, and D. R. Iskander, "Relationships between corneal OCT speckle parameters, corneal deformation parameters and ocular biometrics in porcine eyes in intraocular pressure elevation study,", Annual Meeting of the Association for Research in Vision and Ophthalmology (ARVO), *Investigative Ophthalmology & Visual Science*, vol. 61, pp. 5214, 2020.

Contents

List of Figures

List of Tables

List of Abbreviations

AQD	aqueous depth
AL	axial length
BD	benchmark distribution
CCT	central corneal thickness
CDF	cumulative distribution function
CF	characteristic function
CR	contrast ratio
eCDF	empirical cumulative distribution function
eCF	empirical characteristic function
GLCM	gray-level co-occurrence matrix
GoF	goodness of fit
IOP	intraocular pressure
KDE	kernel density estimator
MLE	maximum likelihood estimation
MMD	maximum mean discrepancy
MSE	mean square error
OCT	optical coherence tomography
PBS	phosphate-buffered saline
PDF	probability density function
RMS	root mean square
ROI	region of interest
SD–OCT	spectral-domain optical coherence tomography
SS–OCT	swept source optical coherence tomography
TD–OCT	time-domain optical coherence tomography

List of Symbols

a	scale parameter of two- and three-parameter distributions
a_k	amplitude of elementary phasor
A	amplitude of speckle field
$A^{(i)}$	imaginary part of complex amplitude
$A^{(r)}$	real part of complex amplitude
$B(x, y)$	intensity point spread function
c	shape parameter of three-parameter distributions
h	bandwidth of the kernel function
I	intensity of speckle field
I'	integrated intensity
$\mathcal{K}(\cdot)$	kernel function
$K_v(\cdot)$	modified Bessel function of the second kind of order v
n	refractive index of air
n_1	standard keratometric refractive index
n_M	refractive index of scattering medium
n_0	number of speckles within scanning aperture
$\mathcal{N}(0, \sigma^2)$	normal (Gaussian) distribution with zero mean and variance σ^2
$p_X(\cdot)$	probability density function of the distribution of random variable X
r_1	radius of a light beam lateral spot
r_2	half width at $1/e$ amplitude of OCT signal
sup	supremum
V_C	coherence volume
x_M	sample median of x
X	random variable
$\beta(\cdot)$	beta function
$\Gamma(\cdot)$	gamma function
μ_k	distribution moment of kth order
ν	shape parameter of two- and three-parameter distributions
σ	scale parameter of Rayleigh distribution
σ^2	variance
σ_{MLE}	maximum likelihood estimator of parameter σ
σ_{Bayes}	Bayes estimator of parameter σ
$\hat{\sigma}_x$	sample standard deviation

ϕ	phase of speckle field
ϕ_k	phase of elementary phasor
$\langle \cdot \rangle$	ensemble average
$\lvert \cdot \rvert$	length of a vector
$\overline{x}$	sample mean of x

To my husband and son,

for being my rock and safe haven.

Preface

Speckle was formerly undesirable in optical coherence tomography (OCT) images and a number of methods were developed for its reduction to better visualize structures of imaged tissues. Nowadays, more and more researchers focus on extraction of information carried by speckle. Association of this information with properties of examined tissue allows to indirectly explore sample microstructure.

The main goal of this thesis is to develop some statistical methods of speckle analysis to indirectly assess corneal properties, which may be influenced by intraocular pressure (IOP). The motivation of this thesis results from the importance of fast detection of undesired levels of IOP and to prevent potentially harmful effects they could cause to eye structures. Moreover, elevated IOP is the main risk factor for glaucoma, a disease leading to progressive and irreversible vision loss. Obtaining indirect information about IOP from OCT images could provide a new functionality of OCT devices that would facilitate a quick screening of some pathological processes occurring in the eye.

The following scientific hypotheses are put in this work:

- Speckle in OCT images is dependent on the number of scattering particles in examined medium and can be characterized using probabilistic models.
- Changes in corneal properties, induced by intraocular pressure, may be evaluated indirectly using speckle statistics in OCT images.
- Speckle statistics can be evaluated by either distributional parameter estimation or using a non-parametric method and both these approaches are equivalent in terms of diagnostic power.

This thesis is divided into four chapters and two appendices. In the first chapter, an introduction containing the most relevant and current information based on literature review about technical realizations and applications of OCT is provided, including speckle theory, methods used for speckle analysis and basic description of the corneal structure and properties. In Chapter 2, the methodology of three studies used in this work is presented with detailed descriptions of experimental procedures and data analysis. The third chapter contains the collection of results where changes in speckle statistics connected with scatterer density and IOP are evaluated. The summary of the work, conclusions from the studies and future directions for the statistical analysis of speckle in OCT images is presented in Chapter 4.

Two appendices are also included in this work. In the first one, the statistics of speckle and background noise are considered for averaged OCT images. The second appendix contains calculations leading to the formula of probability density function of theoretical model of corneal OCT speckle. The assumed model is the product distribution of two gamma random variables. The moments of this distribution, as well as estimators of its parameters, are also computed.

Chapter 1

Introduction

1.1 Optical coherence tomography

1.1.1 Principles and technical realizations

Optical coherence tomography (OCT) is an imaging technique that enables cross-sectional imaging of a scattering medium. Since it is noninvasive and has a relatively high resolution, it is particularly suitable in biomedical applications for *in-vivo* imaging of tissues, especially when the traditional microscopy *in-vitro* is inconvenient or even impossible to be performed. For that reason, this method has been widely used in ophthalmology, optometry, dermatology, otolaryngology, dentistry, gynaecology and many other medical fields [1].

OCT origins date back to 1980s when Fercher and his group were working on the interferometric techniques that use partially coherent light for eye measurements *in-vivo* [2]. Since then, many researchers studied methods based on interferometry for eye structures imaging and finally the term "optical coherence tomography" was defined in 1991 by Huang et al. [3].

The general working principle of OCT is analogous to ultrasonography (USG), where amplitude and delay of the ultrasound beam, backreflected or backscattered from tissues with various acoustic properties, are measured. In OCT there is a near-infrared light beam instead of ultrasound wave, so the examined structures are being imaged according to their optical properties. In both methods the axial measurement of time it takes for ultrasound or light to travel back to a detector from the tissue is called A-mode scanning. Combining together multiple A-scans, the cross-section of the object, called B-scan, can be obtained. The main difference between these methods is that the speed of the sound is about 1500 m/s, while the light speed reaches $3 \cdot 10^8$ m/s. Consequently, the OCT method allows to reach better axial resolution of about 1–10 μm, which is 10–100 times finer than that of USG [4].

There are two main technical realizations of OCT. First of them is time domain OCT (TD-OCT), implemented in devices initially. A simple scheme of this method is presented in figure 1.1. The light from low-coherence source is

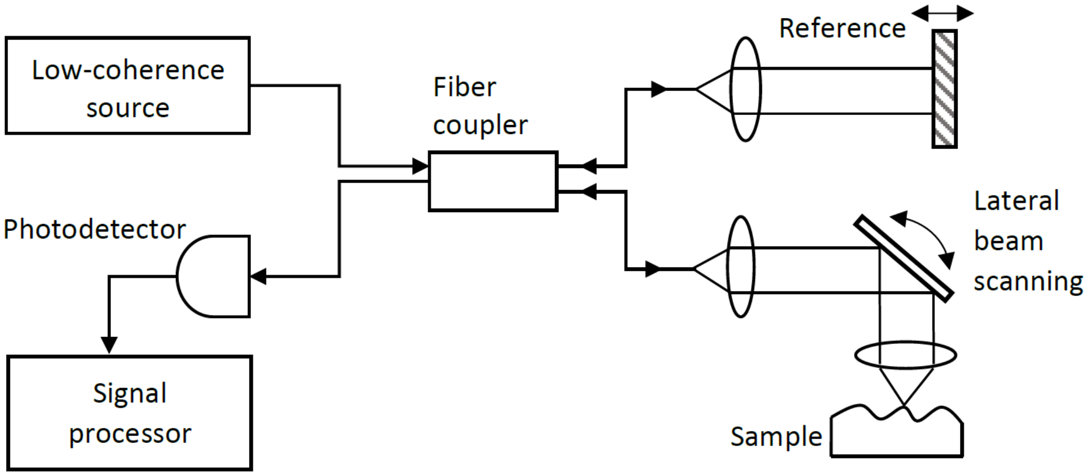

FIGURE 1.1: A scheme of a time-domain OCT system (author's own artwork based on [4]).

split into two arms. The first arm is the reference, which length is modified for depth imaging. The light backreflected in this arm is combined with the sample beam and interferes only when the optical path lengths are equal. Then it is registered by a photodetector, processed into electronic signals and as a result an A-scan is generated, presenting a depth profile of the sample reflectivity at a particular beam position [5].

Another generation of OCT technology is known as a Fourier domain OCT. It was first proposed by Fercher et al. [6] and uses spectral information to create A-scans without the mechanical modification of the optical path length. It comprises two systems: spectral domain OCT (SD-OCT), presented in figure 1.2, and swept source OCT (SS-OCT), shown in figure 1.3. In SD-OCT there is a broadband light source and the length of a reference arm is fixed. The spectral interference pattern arises from the light from the reference arm and all depths in the sample. It is then dispersed and collected on an array detector. The SS-OCT differs in the implementation of the light source, which has narrow linewidth with rapidly swept wavelength, so the spectral interference pattern is detected by a photodetector as a function of time. In both systems the sample depth-resolved structure is encoded in the spectral frequency of the interference pattern and the A-scan is generated using inverse Fourier transform [4].

The development of spectral-based OCT configurations led to over hundred times faster scan acquisition compared to TD-OCT [7]. It contributed to the improvement of OCT sensitivity and resolution, and also the reduction of noise and motion artifacts [8]–[10]. All these advantages caused the dominance of Fourier domain systems in modern OCT devices.

OCT is a coherent imaging method, which means that the OCT signal is

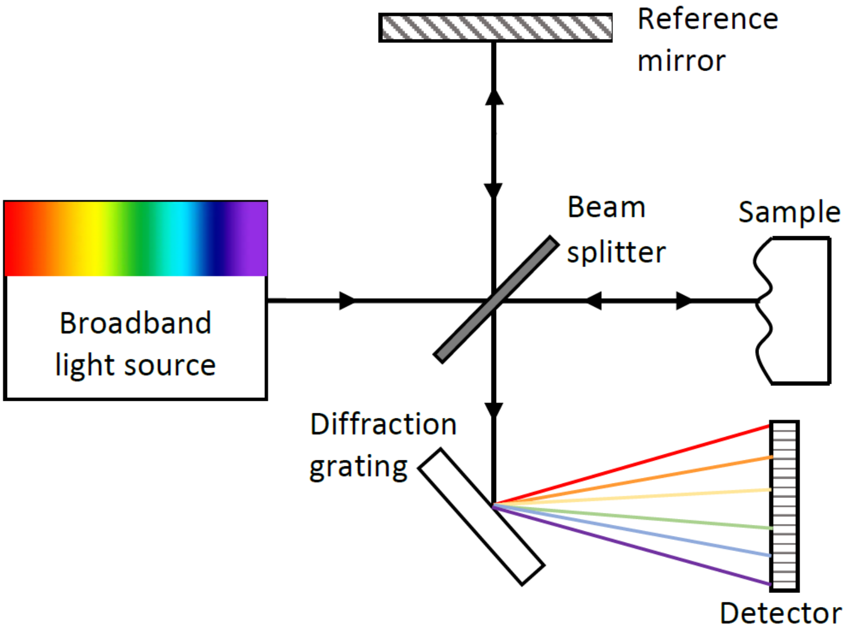

FIGURE 1.2: A scheme of a spectral domain OCT system (author's own artwork based on [5]).

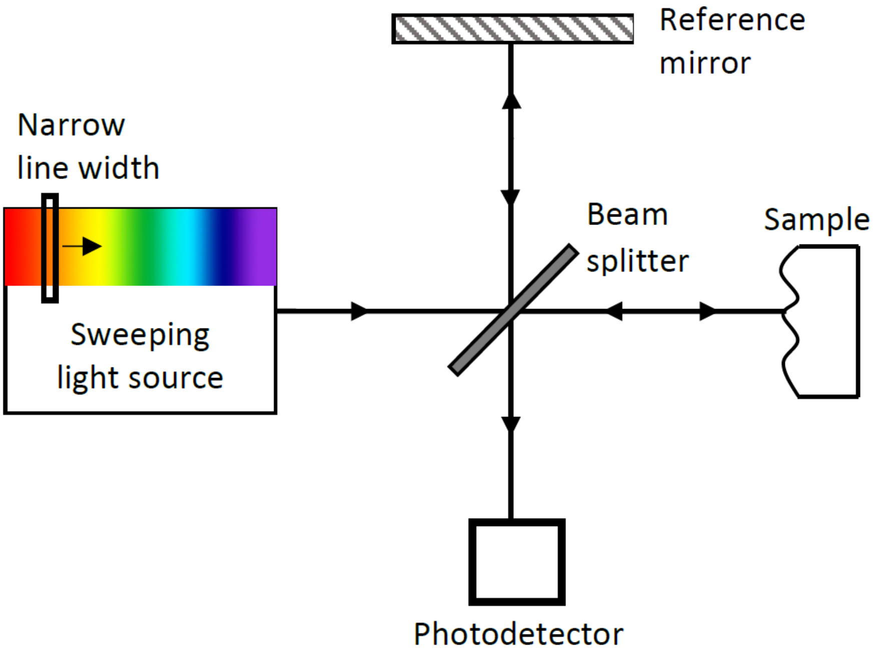

FIGURE 1.3: A scheme of a swept source OCT system (author's own artwork based on [5]).

the sum of complex amplitudes in contrary to incoherent methods, where the intensities are summed. When turbid media are imaged by coherent modalities, there is a special kind of noise observed, called speckle. It results from the composition of the turbid media imaged with OCT, which typically have high densities of sub-resolution scatterers [11].

Speckle is usually characterized as granular or mottled appearance of OCT B-scans [12]. It is usually treated as noise impeding the differentiation of sample morphological features. Thus, there is a number of works considering different speckle reduction methods [13]–[17]. Nevertheless, it can be also considered as a source of information [18]. OCT speckle is affected by the sample structure, as well as by the distribution of scatterers in the sample, so the analysis of speckle may be a valuable source of information about the sub-resolution microstructure. It is worth noting, that speckle analysis should consider that speckle is affected also by spatial extent and temporal coherence of the source of light, the aperture of the detector and also by multiple scattering in the sample volume [19].

1.1.2 Biomedical applications

The primary OCT application was ophthalmology. As a non-invasive and high-resolution imaging method it allows to precisely visualize various eye structures. It is used for imaging both the anterior and posterior parts of the eye. Besides great resolution, compared to other imaging methods used in medicine, OCT has also relatively low cost and does not employ ionizing optical radiation. Moreover, it can be construed using fiber optical components, what makes it portable and able to be incorporated into catheters or endoscopes. That allows to use OCT for imaging the structure of internal organs that are difficult to access [20]. In comparison with non-optical imaging modalities, OCT is characterized by high axial and transversal resolution and also allows contact-free and non-invasive imaging. The main disadvantage is that it has limited penetration depth in high scattering media [21].

To show the diversity of OCT applications in medicine, table 1.1 shows the exemplary publications, where the use of OCT for different organs or tissues was presented. It is clear that because of its advantages this modality has found a number of applications in different fields of medicine.

TABLE 1.1: The review of OCT applications in medicine.

Publication	Imaged tissues	Field of medicine
Hee et al. [22]	Retina, macula, optic nerve head	Ophthalmology
Grulkowski et al. [23]	Retina, anterior segment, full eye	
Manjunath et al. [24]	Choroid	
Schuman et al. [25]	Nerve fiber layer	
Haouchine et al. [26]	Macula	
Iskander et al. [27]	Cornea	
Leung et al. [28]	Anterior chamber of the eye	
Gladkova et al. [29]	Skin	Dermatology
Pagnoni et al. [30]	Skin with cutaneous changes	
Aydin et al. [31]	Nails	
Capodanno et al. [32]	Atherosclerotic plaque	Cardiology
Xu et al. [33]	Blood vessels	
Kume et al. [34]	Coronary thrombus	
Chu et al. [35]	Articular cartilage	Orthopedics
Zheng et al. [36]	Knee joint	
Djalilian et al. [37]	Tympanic membrane	Otolaryngology
Wong et al. [38]	Larynx	
Lueerssen et al. [39]	Vocal folds	
Mahmood et al. [40]	Nasal cavity	
Bouma et al. [41]	Stomach, esophagus	Gastroenterology
Sivak et al. [42]	Esophagus, stomach, colon, rectum	
Arvanitakis et al. [43]	Biliary tract	
Testoni et al. [44]	Pancreatic duct	
Gallwas et al. [45]	Uterine cervix	Gynecology
Kirillin et al. [46]	Fallopian tubes	
Hariri et al. [47]	Ovarian cancer	
Wessels et al. [48]	Vulvar cancer	
Schneider et al. [49]	Tooth decay	Dentistry
Shimada et al. [50]	Teeth structure, dental caries	
Fernandes et al. [51]	Gingivae	

1.2 Speckle

1.2.1 Fundamentals of speckle theory

Speckle are random spatial intensity fluctuations that can be observed when coherent light is reflected or transmitted through the medium with a large number of scattering particles (scatterers). Thus, the obtained distribution of the intensity is referred to as a speckle pattern. Its statistical characteristics depend on the properties of both the incident light and the scattering medium [12]. From the physics standpoint speckle occurs in a signal when it is composed of a number of complex components having random amplitudes and phases. The summation of these components constitutes a random walk in a complex plane, schematically presented in figure 1.4. Consequently, the amplitude of the resultant phasor may be represented by the sum

$$A(x,y,z) = \sum_{k=1}^{N} \frac{1}{\sqrt{N}} a_k(x,y,z) = \frac{1}{\sqrt{N}} \sum_{k=1}^{N} |a_k| e^{i\phi_k}, \tag{1.1}$$

where $a_k(x,y,z)/\sqrt{N},\ k = 1,2,...,N$ is the amplitude and $\phi_k,\ k = 1,2,...,N$ is the phase of the kth elementary phasor. To preserve finite second moments of the sum when the number of elementary phasors tends to infinity, the scaling factor $1/\sqrt{N}$ is included here.

The investigation of statistical properties of the resultant complex field is based on the following assumptions [52], [53]:

(i) The amplitude a_k and the phase ϕ_k of the kth elementary phasor are random variables, statistically independent from each other and from a_j and ϕ_j for all $k \neq j$.

(ii) The phase ϕ_k is uniformly distributed on the interval $[-\pi, \pi]$.

The above-mentioned assumptions are essential to calculate average values of the real and imaginary parts of the resultant field as follows

$$\langle A^{(r)} \rangle = \langle \mathrm{Re}\{A\} \rangle = \frac{1}{\sqrt{N}} \sum_{k=1}^{N} \langle |a_k| \cos\phi_k \rangle = \frac{1}{\sqrt{N}} \sum_{k=1}^{N} \langle |a_k| \rangle \langle \cos\phi_k \rangle = 0, \tag{1.2}$$

$$\langle A^{(i)} \rangle = \langle \mathrm{Im}\{A\} \rangle = \frac{1}{\sqrt{N}} \sum_{k=1}^{N} \langle |a_k| \sin\phi_k \rangle = \frac{1}{\sqrt{N}} \sum_{k=1}^{N} \langle |a_k| \rangle \langle \sin\phi_k \rangle = 0, \tag{1.3}$$

where $\langle \cdot \rangle$ denotes ensemble average. Because of the statistical independence of amplitude and phase, which is provided by the assumption (i), the averaging can be performed over $|a_k|$ and ϕ_k separately. The uniform distribution of the phase, described in assumption (ii), provides zero values for $\langle \cos\phi_k \rangle$ and $\langle \sin\phi_k \rangle$.

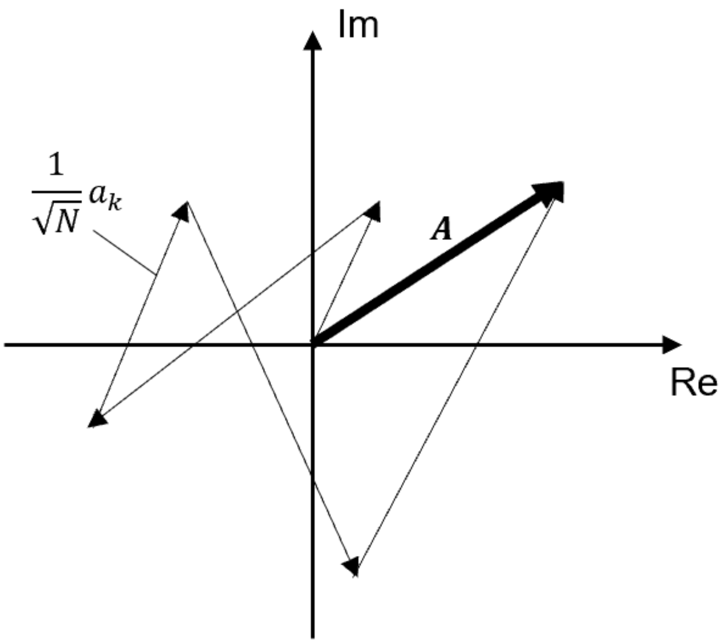

FIGURE 1.4: The summation of amplitude components $\frac{1}{\sqrt{N}}a_k$ to the resultant phasor A, presented as a random walk in a complex plane (author's own artwork based on [54]).

When the number N of elementary phasors is large, $A^{(r)}$ and $A^{(i)}$ amplitude components are asymptotically Gaussian due to the central limit theorem. Thus the joint probability density function (PDF) of the real and imaginary parts of the field is in the form [54]

$$p_{r,i}(A^{(r)}, A^{(i)}) = \frac{1}{2\pi\sigma^2} \exp\left\{ - \frac{[A^{(r)}]^2 + [A^{(i)}]^2}{2\sigma^2} \right\}, \tag{1.4}$$

where

$$\sigma^2 = \lim_{N\to\infty} \frac{1}{N} \sum_{k=1}^{N} \frac{\langle |a_k|^2 \rangle}{2}. \tag{1.5}$$

As such a PDF (equation 1.4) is referred to as a circular Gaussian density function, the phasor amplitude A is a circular complex Gaussian random variable.

The real and imaginary parts of the complex amplitude are connected with intensity I and phase θ of the resultant field as follows

$$A^{(r)} = \sqrt{I}\cos\theta, \tag{1.6}$$

$$A^{(i)} = \sqrt{I}\sin\theta. \tag{1.7}$$

Above dependencies may be equivalently written

$$I = [A^{(r)}]^2 + [A^{(i)}]^2\,, \tag{1.8}$$

$$\theta = \tan^{-1}\frac{A^{(i)}}{A^{(r)}}\,. \tag{1.9}$$

Having above-mentioned relationships, the distributions of amplitude, intensity and phase of the speckle field may be obtained using basic transformations [55]. Since the amplitude of the speckle field is considered as a phasor in the complex plane with its real and imaginary parts noted as $A^{(r)}$ and $A^{(i)}$, respectively, the length of this phasor may be calculated as follows

$$|A| = \sqrt{[A^{(r)}]^2 + [A^{(i)}]^2}\,, \tag{1.10}$$

where $A^{(r)} \sim \mathcal{N}(0,\sigma^2)$ and $A^{(i)} \sim \mathcal{N}(0,\sigma^2)$ are independent normal random variables. Then $|A|$, calculated due to the formula (1.10), is a Rayleigh distributed random variable with the scale parameter σ and with the PDF described by the equation

$$p_X(x) = \frac{x}{\sigma^2}\exp\left\{-\frac{x^2}{2\sigma^2}\right\}, \quad x \geq 0\,, \tag{1.11}$$

where the random variable $X = |A|$.

For this distribution the ratio of the standard deviation to the mean is known as contrast ratio (CR) [56] and is equal to

$$\mathrm{CR} = \sqrt{(4/\pi - 1)} \approx 0.52\,. \tag{1.12}$$

High values of CR indicate that the distortion caused by speckle (described by the standard deviation) is large compared to the imaged underlying structure, characterized by the mean [11].

Similarly, as the speckle field intensity is described by the formula (1.8), so it is squared amplitude modulus, then it follows the exponential distribution with the scale parameter $2\sigma^2$, described by the PDF

$$p_X(x) = \frac{1}{2\sigma^2}\exp\left\{-\frac{x}{2\sigma^2}\right\}\,, \tag{1.13}$$

where the random variable $X = I$.

The phase, described by (1.9), is uniformly distributed on the interval $[-\pi, \pi]$ with the PDF

$$p_X = \frac{1}{2\pi}\,, \tag{1.14}$$

where the random variable $X = \theta$.

1.2.2 Sum of speckle patterns

The statistical properties presented so far are applied to the complex amplitude and intensity at one or more points in a speckle pattern. In practice, the speckle pattern is rather averaged over some area, for example by a scanning aperture. As a result the integrated intensity $I'(x,y)$ is obtained, which is related to the intensity of a speckle pattern $I(x_1,y_1)$ by a convolution

$$I'(x,y) = \int_{-\infty}^{\infty}\int_{-\infty}^{\infty} I(x_1,y_1)B(x-x_1,y-y_1)dx_1dy_1\,, \tag{1.15}$$

where $B(x,y)$ is the intensity point spread function of the averaging device, normalized that the volume of $B(x,y)$ is equal to 1 [12]. It can be proved that after appropriate transformations an approximate distribution of the integrated intensity is the gamma distribution with following probability density functions for $X = |A|$

$$p_X(x) = \frac{1}{\Gamma(\nu)}a^{\nu}x^{\nu-1}\exp(-ax)\,, \quad x > 0\,, \tag{1.16}$$

for $X = I'$ [1]

$$p_X(x) = \frac{1}{2\Gamma(\nu)}a^{\nu}x^{\frac{\nu}{2}-1}\exp(-a\sqrt{x})\,, \quad x > 0\,, \tag{1.17}$$

with the shape parameter ν, the scale parameter a and $\Gamma(\cdot)$ denoting the gamma function [57].

Following [12], gamma distribution parameters can be linked to the speckle properties via $\nu = n_0$ and $a = n_0/\langle I\rangle$, where n_0 is interpreted as the number of independent correlation cells (speckles) within the scanning aperture and $\langle\cdot\rangle$ denotes ensemble average.

1.2.3 Small number of scatterers

Sometimes the number of scattering particles which contribute to the amplitude at a point in the observation plane is not sufficient to make the central limit theorem applicable. Then, the distribution of the complex amplitude is no longer complex Gaussian. The statistics of the speckle field in this case are strongly dependent on the statistics of the scattering medium [12], [58]. The number N of contributions to the speckle field is then assumed to fluctuate in accordance with the negative binomial distribution [53], [59]. That leads to the K distribution statistics for both the amplitude and intensity, described by following probability density functions

---

[1] $I = |A|^2$ so the PDF for the intensity is obtained by the change of variable due to the formula $f_Y(y) = f_X(g^{-1}(y))|d/dy(g^{-1}(y))|$ where X and Y denote random variables and $g^{-1}(\cdot)$ is the inverse function.

for $X = |A|$

$$p_X(x) = \frac{4}{\Gamma(\nu)}\sqrt{\frac{\nu}{\langle x^2\rangle}}\left(\frac{\nu x^2}{\langle x^2\rangle}\right)^{\nu/2} K_{\nu-1}\left(2\sqrt{\frac{\nu x^2}{\langle x^2\rangle}}\right), \tag{1.18}$$

for $X = I$

$$p_X(x) = \frac{2}{\Gamma(\nu)}\sqrt{\frac{\nu}{x\langle x\rangle}}\left(\frac{\nu x}{\langle x\rangle}\right)^{\nu/2} K_{\nu-1}\left(2\sqrt{\frac{\nu x}{\langle x\rangle}}\right). \tag{1.19}$$

In both of the above equations $\langle\cdot\rangle$ denotes mean value, $\Gamma(\cdot)$ is the gamma function and $K_{\nu-1}(\cdot)$ is the modified Bessel function of the second kind of order $\nu - 1$. The shape parameter of the K distribution, ν, is given by the formula

$$\nu = \frac{2}{\sigma_I^2 - 1}, \tag{1.20}$$

where σ_I^2 is the variance of the relative intensity $I/\langle I\rangle$ [60].

In practical applications the average number of scattering particles is defined within the probed optical resolution element, that is coherence volume for volumetric scattering or coherence area for surface scattering [61]. Based on experimental results, the number of scatterers in coherence volume should be less than ~ 10 to consider non-Gaussian scattering statistics [62].

1.2.4 Coherence volume

An important issue in speckle characterization is the initial evaluation if the speckle field results from scattering that can be described by Gaussian statistics. For that, it is essential to assess the number of scatterers in coherence volume, referred also as a scatterer density. The calculation of coherence volume is based on the properties of a light beam and scattering medium. It is defined as the volume of an ellipsoid described by the equation

$$V_C = \frac{4\pi r_1^2 r_2}{3n_M}, \tag{1.21}$$

where r_1 is the radius of the light beam lateral spot (i.e., half of the width at $1/e^2$-light-intensity-maximum), r_2 is half width at $1/e$ amplitude of OCT signal and n_M is the refraction index of the scattering medium. It is assumed that the OCT signal for a particular location in the sample has contributions only from scatterers within the coherence volume around this location [61], [63].

1.2.5 Fully developed speckle field

Another issue in the statistical analysis of speckle in OCT scans is to consider if the imaged speckle field is fully developed. That is critical for choosing proper statistical description of speckle. Fundamental statistics for the fully developed speckle field were presented by Goodman [52]. The amplitudes and phases of the speckle field are statistically independent and phases come from the uniform distribution over $[-\pi, \pi]$. Based on that, the distributions of speckle amplitude, intensity and phase are obtained and they are presented in this work in section 1.2.1. Speckle field described by these statistics is referred to as fully developed.

Fully developed speckle field was also studied by Uozumi and Asakura [64], who showed that the phase of the speckle field does not always approach uniform distribution on the interval $[-\pi, \pi]$ and is dependent on the phase distribution of scattering object. Wang [65] concluded that to constitute fully developed speckle field, the ensemble average of the complex amplitude at a particular point should be equal to zero, so the following conditions need to be satisfied

$$\langle A_r \rangle = 0 \text{ and } \langle A_i \rangle = 0\,. \tag{1.22}$$

The above-mentioned definitions may seem confusing and they are difficult to validate in practical applications. Usually the assumption of fully developed speckle field is made when known or assessed number of scatterers in coherence volume of analysed object is large enough to consider Gaussian scattering statistics (see section 1.2.3) [19], [56].

1.2.6 Amplitude and intensity — nomenclature

In publications regarding statistical analysis of speckle pattern, the parameters of probability distributions are usually estimated for pixel values from the specified region of interest (ROI) in OCT B-scans. To evaluate accuracy of distribution fitting, the PDF is usually compared with the histogram of these pixel values. They represent in greyscale the amplitude or intensity of the light backscattered from the sample. Both terms, amplitude and intensity, are used in literature and that may be confusing which of them is relevant for the description of speckle in OCT images. It is noteworthy due to different statistics of speckle field amplitude and intensity, described in section 1.2.1.

There are different approaches to that problem in literature. Some works consider pixel values in OCT images as amplitude and use Rayleigh distribution to model them [63], [66]. Sugita et al. [61] presented histograms of intensities considered as squared amplitude from pixel values in OCT B-scans. In other works, pixel values are treated as intensity [67]–[69]. Ge et al. [57] in his work presented statistical analysis for both amplitude and intensity separately, fitting theoretically justified probability distributions to each of them (Rayleigh, K, gamma and Burr type XII distributions for amplitude and exponential, K, gamma and Lomax distributions for intensity). There is also a number of publications in which pixel values are referred as "pixel intensities" for probability distribution fitting [27], [70]–[73] and there is no information which of the light characteristics they represent in OCT B-scans. It is also worth noting that typically in OCT images the logarithm of amplitude/intensity is presented for better visualization.

In this work pixel values are considered as amplitude. Apart from the literature, it is also supported by the example presenting the histogram of pixel values from OCT B-scan, originally log-transformed in the device software, also, the histogram of pixel values after inverse-log transformation, treated as amplitude and the histogram of the squared values of amplitude, corresponding to intensity. Figure 1.5 shows the selected ROI from which pixel values are taken to create three described histograms. Also, PDFs of theoretically supported Rayleigh and exponential distributions, for amplitude and intensity, respectively, are shown for comparison. It is clearly visible from this image that pixel values can be described by Rayleigh statistics while their squared values are consistent with the exponential statistics of intensity in OCT images.

1.2.7 Speckle modelling

Parametric approach

A common approach to speckle modelling is based on the distribution fitting to pixel intensities from the specified ROI in the OCT image. Since speckle arises from the light scattered on particles smaller than OCT resolution, the distributional parameters are thought to be associated with some properties of sample microstructure. Thus, their estimation allows to indirectly obtain some information about this microstructure.

A number of distributions were considered for this purpose, some of them resulting from the theory of speckle formation and some chosen based on the goodness of fit (GoF) to the histogram of appropriately transformed, when needed, pixel values. The fundamental theoretical distribution of speckle amplitude is the Rayleigh distribution, provided that the speckle field is fully developed. Almasian et al. [63] showed a good fitting (Pearson correlation coefficient, $R > 0.980$) of the Rayleigh distribution to the amplitude in the OCT images of silica microspheres suspended in water. The number of scattering particles in the coherence volume was in the order of $10^2 - 10^4$ and the mean diameter of the particles was about $0.47 - 1.60$ μm.

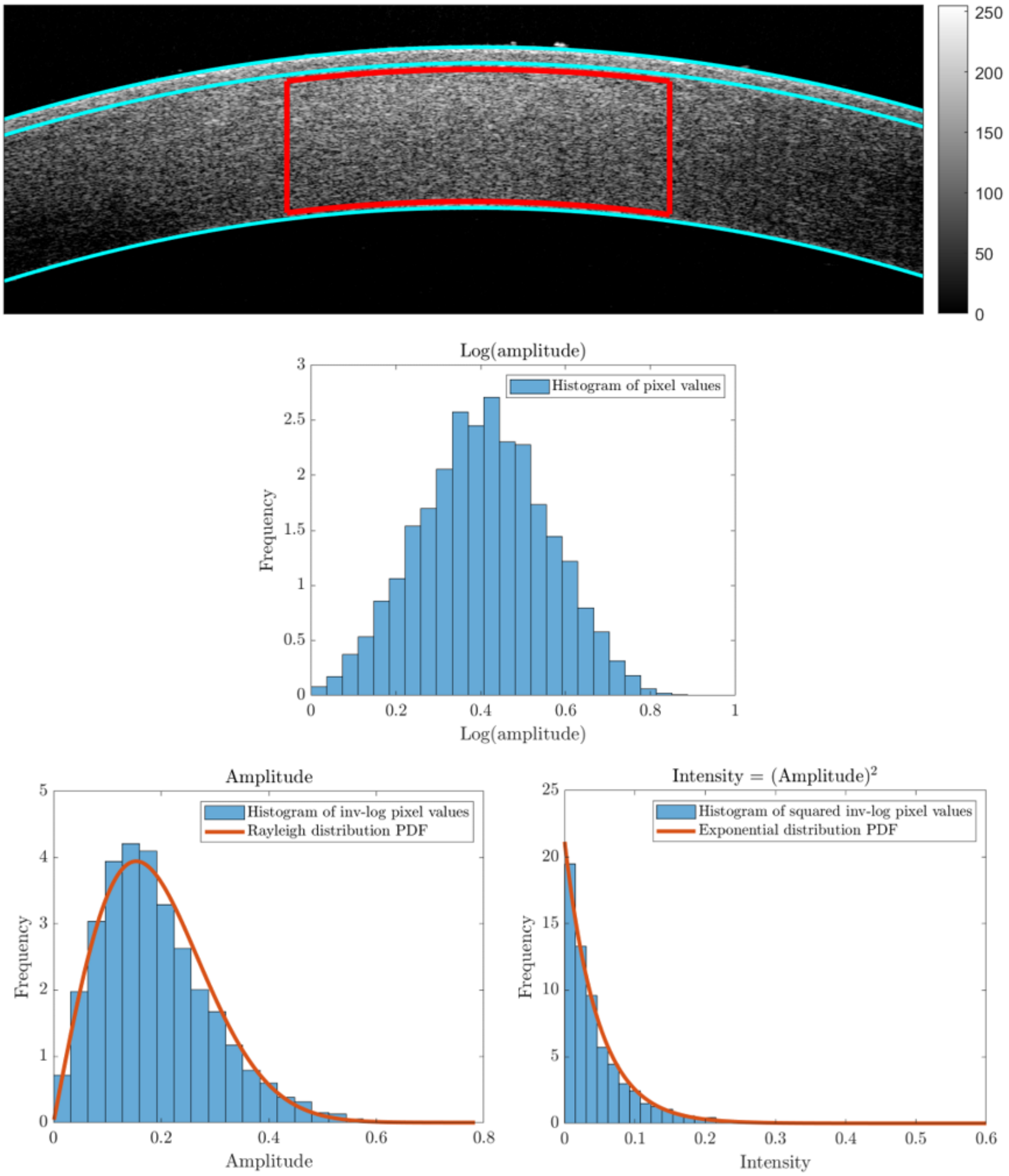

FIGURE 1.5: Illustrative OCT B-scan of cornea with the ROI indicated by red lines and the histogram of pixel values from the ROI (Log(amplitude)). In the bottom panel the histograms of amplitude (inverse-log transformed original pixel values) and intensity (squared amplitude values) are presented together with PDFs of corresponding theoretical distributions.

Some researchers considered K distribution for the description of speckle statistics when the number of scatterers in coherence volume is less than ~ 10 (see section 1.2.3). Weatherbee et al. [60] presented that for the microspheres suspensions in water decreasing number of particles per voxel caused the fitting deterioration of the Rayleigh and negative exponential distribution for the OCT images amplitude and intensity, respectively. The K distribution was showed to better fit both amplitude and intensity and also its shape parameter was proportional to the average number of scatterers in coherence volume.

Lindenmaier et al. [71] obtained a good fitting ($R^2 \sim 0.985$) of gamma distribution for histograms of pixel values from OCT B-scans showing normal and solid tumour mouse tissue. They showed statistically significant differences in values of the ratio of gamma distribution shape and scale parameters for normal and tumour tissues (p-value < 0.001). Kirillin et al. [70] experimentally showed the relationship between the scale parameter of gamma distribution and the concentration of scattering particles.

Ge et al. [57] proposed another approach to OCT speckle modelling based on the work of Parker and Poul [74], who derived amplitude and intensity distribution for ultrasound speckle using power law. They used Burr type XII and Lomax (Pareto type II) distributions for the fitting of speckle amplitude and intensity, respectively. It was shown, that these distributions fit OCT amplitude/intensity histograms better compared to Rayleigh/exponential, K and gamma distributions. Moreover, both Burr type XII and Lomax distributions have exponent parameter, which was shown to have different values depending on tissue type with smaller values for relatively transparent tissues (e.g., hand, cornea) and higher values for optically denser ones (e.g., brain, liver).

Table 1.2 contains the summary of statistical distributions used for speckle modelling in the literature and types of analysed scattering medium. It shows a variety of distributions considered in parametric approach to speckle analysis.

Non-parametric approach

There are also some methods for speckle analysis that do not require the estimation of distributional parameters, hereafter referred as non-parametric. They are based on CR, defined by the equation 1.12, and changes of its values in OCT images. The purpose of these methods, similarly to the parametric ones, is to correlate some speckle characteristics with sample optical properties.

Hillman et al. [19] showed that CR of OCT speckle is dependent on the density of scattering particles in a sample. For the number of scatterers in coherence volume less than 5, CR is a decreasing function of scatterer density, while for a large number of scatterers it approaches a constant value of ≈ 0.52, consistent with Rayleigh distribution. Li et al. [75], [76] presented theoretically that for the superficial region of a sample the contrast ratio is a linear function of depth with the proportionality coefficient α dependent on the scattering coefficient of the sample. Therefore, the slope α may be useful for differentiating imaged tissues based on their scattering properties. Moreover, it was shown that for the deep tissue there is a noise superiority over OCT signal and the contrast ratio becomes constant, independent of depth. Similarly, Lee et al. [77] presented the dependence of contrast ratio on sample depth and also on the scattering coefficient of analysed medium.

TABLE 1.2: Distributions used in literature for the fitting of pixel values in OCT B-scans.

Publication	Scattering medium / tissue type	Distribution (best considered)
Ge et al. [57]	pig cornea and brain, mouse liver and brain, chicken muscle gelatine phantom, human hand	Burr type XII
Lindenmaier et al [71]	mouse normal and tumour tissue	gamma
Kirillin et al. [70]	polystyrene microspheres in water	
Jesus et al. [72], [78]	human cornea	generalized gamma
Iskander et al. [27]	human cornea	
Danielewska et al. [79]	rabbit cornea	
Seevaratnam et al. [73]	polystyrene microspheres in glycerin	
Sugita et al. [61]	polystyrene microspheres in water, human skin and fingernail	K
Weatherbee et al. [60]	polystyrene microspheres in water	
Sugita et al. [80]	rat brain and liver	
Dubose et al. [67]	retina	
Sowa et al. [68]	teeth	lognormal
Mcheik et al. [81]	human skin	Nakagami
Almasian et al. [63]	silica microspheres in water	Rayleigh
Pircher et al. [82]	human skin	
Adabi et al. [14]	human retina	
Demidov et al. [66]	mouse skin and tumour tissue	three-parameter Rayleigh
Grzywacz et al. [69]	human retina	stretched exponential

Textural approach

Another methods of speckle analysis consider texture features to be useful in the evaluation of the optical properties of the sample. The spatial grey-level dependence matrices also known as grey-level co-occurrence matrices (GLCM) are used to characterize image texture. They are determined by the estimation of the probability distribution of different spatial combinations of grey-level pixel values. Some statistical measures, such as contrast, correlation, homogeneity, energy and entropy, can be calculated from these matrices and used for image texture characterization.

Gossage et al. [83] used texture parameters of speckle in OCT images for differentiation between tissue phantoms with various distributions and sizes of scatterers. Statistically significant differences were obtained between values of analysed parameters when comparing different endothelial cells concentrations in gelled collagen and different sizes and concentrations of silica microspheres in gelatine. Also, Kasaragod et al. [84] showed the successful usage of texture parameters for the classification of different concentrations of scatterers in tissue phantoms.

1.3 Cornea

1.3.1 Structure

Cornea is a transparent, avascular anterior layer of the eye, that forms a 'window' for the light to entry into the eye. Figure 1.6 shows its position among other ocular structures. Cornea constitutes the outer shell of the eyeball together with the sclera, with which it is connected through the highly vascularized transition zone called limbus. Interwoven collagen fibres, which are main components of the cornea and sclera, provide mechanical strength to maintain the ocular contour and protect inner eye structures from physical injury [85]. The main function of the cornea is to provide the eyeball stiffness and also to transmit the light into the eye with focusing it together with the lens [86].

Figure 1.7 shows the scheme of corneal layers. The stroma is the main layer of the cornea which constitutes about 90% of its thickness. Stroma is bounded on two sides by limiting membranes, Bowman's layer and Descemet's membrane, and associated cellular layers — epithelium and endothelium. Epithelium is the outermost segment of the cornea. It is composed of several stratified, nonkeratinized, squamous cellular layers. It is characterized by the uniform structure for entire width of the cornea. The epithelial thickness is about 50 μm. Between epithelium and stroma there is a Bowman's layer, the acellular condensate of the most anterior part of the stroma, composed of randomly oriented collagen fibrils. It is about 15 μm thick and its main function is supporting the corneal shape [87]. The major part of the cornea, stroma, is composed of collagen fibres. These collagen fibres create bundles called fibrils. They are surrounded by proteoglycans supporting the regulation of hydration, maintaining the space between the fibrils and their size. Parallel fibrils, embedded in a viscous extrafibrillar matrix, form layers, called lamellae,

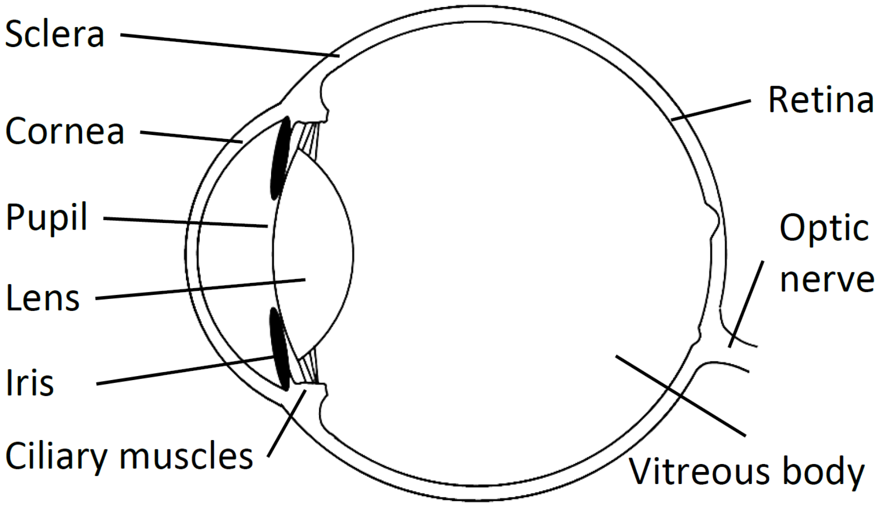

FIGURE 1.6: Scheme of the eyeball with main structures marked (author's own artwork).

stacked almost parallel to the corneal surface. Corneal stroma consists of about 200 to 250 lamellae, each of 1–2 μm thick. Between stromal lamellae there are keratocytes involved in maintaining the stromal structure and also able to synthesize collagen molecules. A specific three-dimensional architecture of collagen fibrils provides the corneal transparency [88]. Because of the hydrophilic character of proteoglycans, the corneal stroma has a strong tendency to absorb water and swell [87], [89], [90]. In the posterior stroma, there is a slightly different region, containing higher lamellae density and increased distances between collagen fibrils. It is extracted as a separate structure, called Pre-Descemet's layer or Dua's layer [91]. Under the stroma there is a Descemet's membrane, composed of collagen fibres different than that of stroma. They form a structure separate from the stroma, but tightly adhering to it. Its thickness is of about 8–10 μm. The most posterior part of the cornea is endothelium, consisting of the single layer of endothelial cells. The primary function of these cells is the transport of solutes and nutrients into the cornea and allowing water flow in the opposite direction [85].

Corneal thickness increases gradually through the cornea from about 500 μm in its centre to about 700 μm at the periphery [90]. The posterior part of the cornea has contact with the anterior chamber of the eye (space between cornea's endothelium and iris) filled with aqueous humor [85]. The anterior part of the cornea is covered by the tear film which is smoothing out the microirregularities on the epithelial surface, providing proper light refraction as the cornea accounts for about 70% of the eye total refractive power [87], [92].

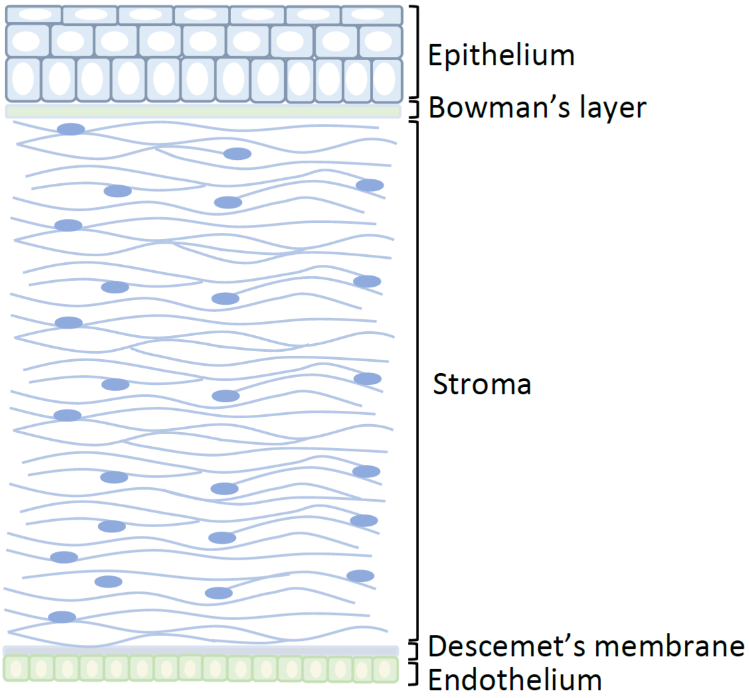

FIGURE 1.7: Scheme of the structure of human cornea, not to scale (author's own artwork based on [92]).

1.3.2 Physical and optical properties

Average adult human cornea measures 11 to 12 mm horizontally and 9 to 11 mm vertically. The radius of curvature is about 7.5 to 8 mm at the central 3 mm of the cornea and it has greater values in the peripheral part. The cornea's refractive power is 40 to 44 diopters [85].

The refractive index of the cornea if varying through the depth and it has values of about 1.400, 1.380, and 1.373 at the epithelium, Bowman's layer and endothelium, respectively. In the mid stroma refractive index value approaches about 1.369 [93]. There are also differences in values of refractive index of internal stromal structures. For the collagen fibres it approaches the value of about 1.411, while for the extracellular matrix it is equal to 1.365 [94]. These differences in refractive index values inside the stroma induce light scattering.

The collagen fibrils in corneal stroma are thought to be responsible for light scattering. The electromagnetic wave radiated by a fibril depends on its radius and the difference in refractive index between the fibril and the medium around it. Also, the amplitude of the electric component of the oscillatory electromagnetic field surrounding a fibril is determining the emitted light and in addition it may be altered by adjacent fibrils. The light radiated by individual fibrils interferes and the amount of scattered energy is dependent on whether the interference is constructive or destructive. The dominating interference type is strongly related to the fibrils arrangement. If they are spaced out regularly within the lamella, the scattered light interferes destructively in all directions except that of the incident beam. For that reason the cornea is perceived as transparent [95]. Ávila et al. [96] showed on the group of healthy subjects that the corneal transparency is not altered by the thickness of the cornea.

1.3.3 Influence of IOP and age on the cornea

In this work the effect of the increase of intraocular pressure (IOP) on the corneal properties, assessed indirectly using the statistics of speckle, is considered. Additionally, the aging of the cornea is another factor which influences these properties, so it is also taken into consideration. To better understand these processes and their possible results on corneal microstructure, a short literature review in this topic is presented here.

Wu and Yeh [97] used nonlinear optical microscopy to image the corneal microstructure in rabbit eyes exposed to the increase of IOP. They showed the decrease of the size of gaps between lamellae with increasing IOP. To examine the potential effect of IOP on human corneal collagen fibres, Bell et al. [98] exposed human corneas to tensile strain. Using X-ray scattering, he showed a decrease in collagen fibrils diameter with increasing strain. Moreover, a corneal deformation induced by tensile strain was the greatest in the peripheral region, but it was also greater in the central ~2 mm of the cornea than in the adjacent para-central regions.

Liu and He [99] presented in their study an inflation test on porcine eyeballs in which higher raise in IOP was observed for corneas which were stiffened. The corneal stiffening is one of the processes that occurs during aging. In the *ex-vivo* study on human corneas, Elsheikh et al. [100] observed statistically significant association between stiffness and age. Among a variety of processes that occur during cornea aging, increase in collagen fibril diameter and decrease in interfibrillar spacing, were observed [101], [102], as well as the decrease in stromal keratocytes density [103], [104].

Chapter 2

Methodology

2.1 Experimental procedures

2.1.1 Phantom study

Preliminary research was conducted on OCT images of purposely designed phantoms to assess the effect of scatterers concentration on speckle statistics. They were made of a transparent epoxy resin L-285 (Havel composited, Cieszyn, Poland). Liquid resin was carefully mixed with a blue dye powder, with scatterer particles of various sizes from few to tens micrometers. The mixtures of different amounts of the blue dye uniformly distributed in the resin were poured on the microscope slides to obtain convex discs of an approximate diameter of 10 mm and thickness of about 1 mm. Then they were carefully placed aside to cure. Figure 2.1 presents phantoms after drying with increasing concentrations (C_1, C_2, ..., C_9) of scattering particles. The C_1 concentration was obtained by adding about 10 mm^3 of the blue dye to 1 cm^3 of epoxy resin. Consecutive concentrations were prepared by adding twice as much dye as for the previous phantom, so about 20 mm^3 of the dye was added to the resin in the C_2 phantom, 40 mm^3 in the C_3 phantom, and so on. The volumes of the resin and the blue dye were not precisely controlled but the increasing scatterers concentration was well maintained for subsequent phantoms. For OCT imaging, the microscope slides were attached to the headholder in front of the device imaging head. The B-scans of size 3077×708 pixels (about 10×2 mm) were registered for the central part of each phantom. The scans were collected using an instrument protocol with an external adapting lens to get scan of width 10 mm. The OCT device used in this and consecutive studies in this work was SOCT Copernicus REVO (Optopol Technology, Zawiercie, Poland) with centre wavelength of 830 nm, half bandwidth of 50 nm, axial resolution of 5 μm, transversal resolution of 15 μm and scanning speed of 80 000 A-scans per second.

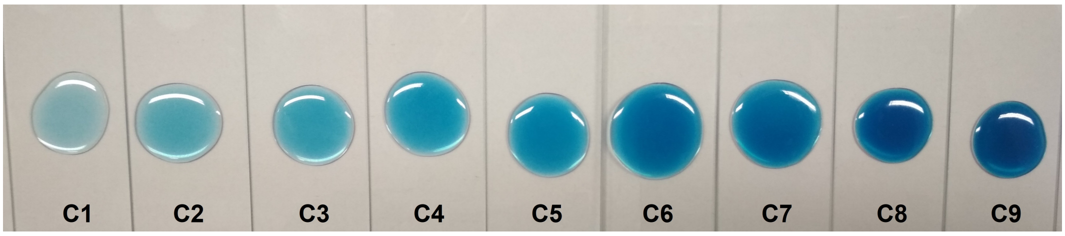

FIGURE 2.1: The resin phantoms used in the study (author's own photograph).

2.1.2 *Ex-vivo* study on porcine eyes

The main part of the research presented in this thesis is performed using OCT scans of *ex-vivo* porcine eyes. It is a collaborative study from which OCT images are used in this research. The short description of experimental procedure as well as the scheme of the setup are presented here for completeness. Detailed information is presented in works [105], [106].

In the study on porcine eyes, fresh eyeballs were acquired from a local abattoir (Meat Processing Plant, Otmuchow, Poland) and then stored at 4°C in phosphate-buffered saline (PBS) solution for no longer than 6 hours. Only eyeballs with transparent corneas and with no damage or edema were selected for further data collection. Before taking measurements, the eyeball was placed in a specially designed holder, padded with the cotton moistened with PBS to restrain dehydration. Also, the optic nerve was attached with a polyamide sewing thread to the post behind the holder, so eyeball movements were substantially minimized. Next, for such prepared eyeballs a 20-gauge needle was inserted into the anterior chamber through the corneo-scleral area and conected to a WIKA P-30 pressure transducer (WIKA Alexander Wiegand SE & Co. KG, Klingenberg, Germany). This sensor is a part of a closed feedback loop, together with a syringe pump, a reservoir column and a control unit, to set and maintain desired IOP levels. The system automatically adjusts the volume of PBS infused or withdrawn to obtain the set value of IOP in the anterior chamber of the eyeball. The entire system is placed on a XY-linear translation platform to enable eyeball positioning for OCT imaging using SOCT Copernicus REVO (described in section 2.1.1) and for ocular biometry measurements using the IOL Master 700 (Carl Zeiss Meditec AG, Jena, Germany). The described setup is presented in figure 2.2.

Two experiments were performed on porcine eyeballs. In first of them, referenced as Experiment 1, IOP was increased from 10 mmHg to 40 mmHg in steps of 5 mmHg. To stabilize the pressure, a 3-minute break was provided after setting IOP value. At each IOP level ocular biometric parameters were also measured, involving central corneal thickness (CCT), axial length (AL), aqueous depth (AQD) and keratometry parameters, translated next into power vectors to calculate mean equivalent spherical power (M) and astigmatic components

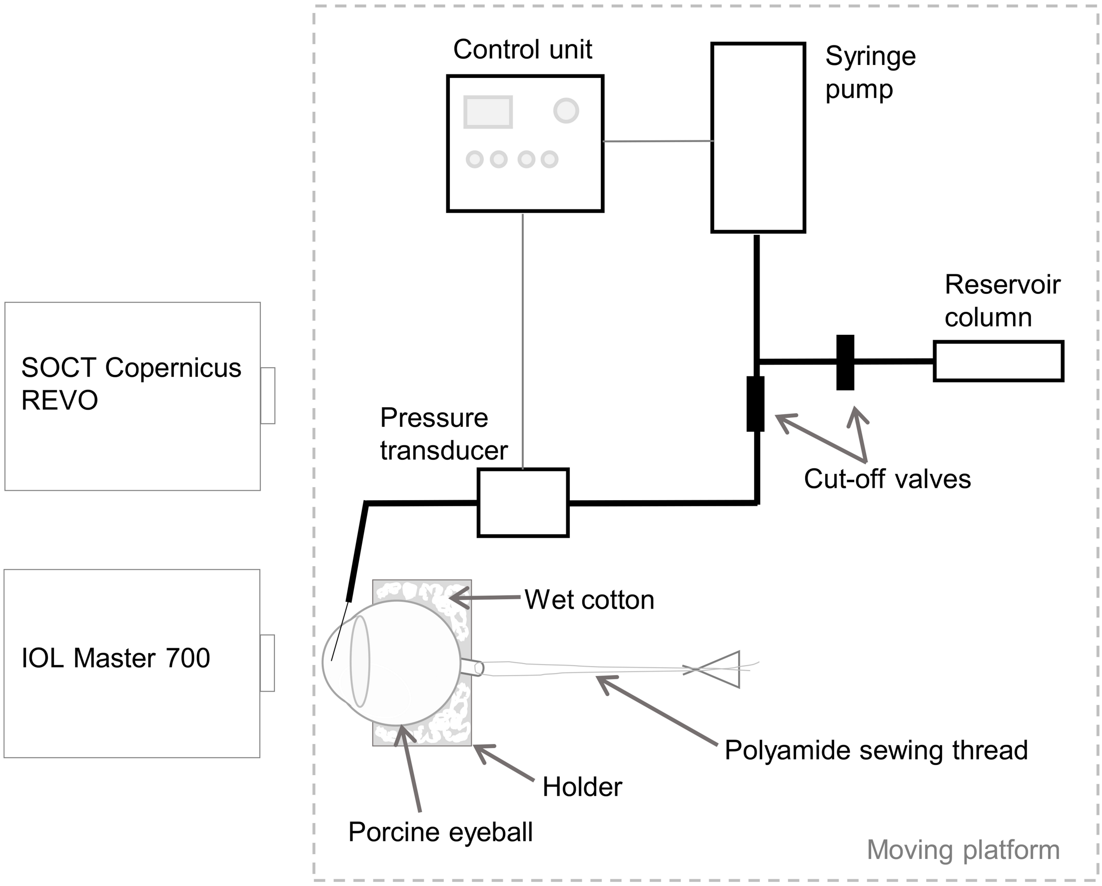

FIGURE 2.2: A scheme of the setup used for porcine eyes measurements in Experiment 1 (increasing IOP) and Experiment 2 (constant IOP). Source: co-authored paper [105].

of Jackson cross-cylinder (J_0 and J_{45}). The biometric parameters are described in detail in section 2.2.5. Next, the platform was moved to place the eyeball in front of the OCT device and three single, non-averaged B-scans of central cornea were collected, each of them of size 1536×736 pixels (about 5 × 2 mm). Afterwards, IOP was increased by 5 mmHg by setting desired value in the control unit interface, and entire procedure was being repeated until reaching an IOP value of 40 mmHg.

The second experiment, referenced as Experiment 2, was performed to investigate how the duration of the experiment influences OCT speckle statistics. Porcine eyeballs were examined in the same manner as in Experiment 1, with the only difference that IOP was maintained constant at the level of 15 mmHg, selected as the typical value for porcine eyes [107].

The entire measurement procedure for one eyeball took about 70 minutes for seven considered IOP levels in Experiment 1 and corresponding time points ($t_1, t_2, ..., t_7$) in Experiment 2. That resulted in taking measurements every 10 minutes. In both experiments the average ambient temperature was 22.5 ±1.9°C (mean ± standard deviation) and the humidity was 50.2 ± 4.5%. The eyeballs were chosen to have CCT from the assumed population limit from 800 μm to 950 μm [107]. After verification, 23 eyeballs were included in Experiment 1 and 10 eyeballs in Experiment 2.

2.1.3 *In-vivo* study on human eyes

In the third study, a retrospective data set was analysed, containing a set of OCT images derived from the measurements performed on a group of 56 healthy Caucasian subjects. They were divided into two groups, according to age, referred as OLD and YOUNG. First of them involved 29 subjects with the mean ($\pm$ standard deviation) age of 58.9 $\pm$ 8.4 (range from 50 to 87) and the second contained 27 subjects with the mean age of 24.8 $\pm$ 2.7 (range from 21 to 30). The analysed data set included also measurements of IOP, performed using the air-puff tonometer Corvis Scheimpflug Technology (Corvis ST, OCULUS, Wetzlar, Germany).

2.2 Data processing

2.2.1 Image analysis

All calculations in this thesis were performed using MATLAB programming language (MathWorks, Inc. Natick, MA, USA). Analysed B-scans were in a logarithmic scale, set automatically in the OCT software to better visualize imaged structures. To obtain raw data, the inverse log-transformation was applied to every image.

The statistical analysis of phantom OCT images was performed for pixel values from the ROI of size 600 × 220 pixels (about 2 × 0.6 mm), with its centre set 600 pixels on the left from the central reflection and with its top border set 20 pixels below the phantom top border (figure 2.3). For OCT images from studies on porcine and human corneas ROI of width 600 pixels (about 2 mm) was set centrally in relation to the corneal apex. The top border of the ROI was placed 10 pixels below Bowman's layer and the lower border was 10 pixels above endothelium (figures 2.4 and 2.5). The pixel values from the ROIs were treated as a random variable X. The statistical analysis for them is described below.

2.2.2 Parametric approach

The fundamental problem in a parametric approach to statistical modelling of speckle is choosing the proper probability distribution to fit the pixel values from the B-scan. There are two main approaches in the literature for the speckle

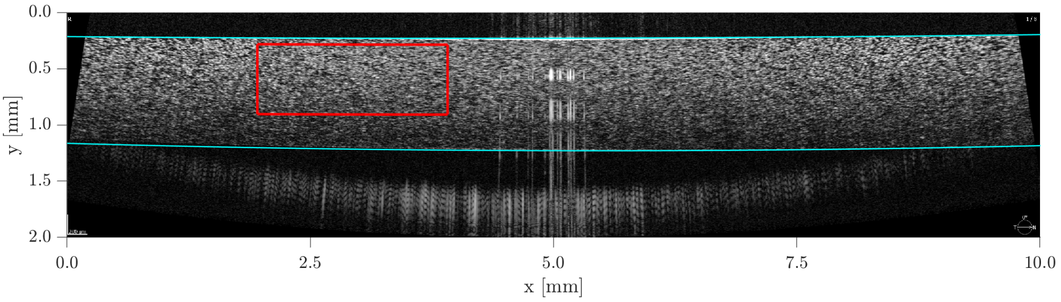

FIGURE 2.3: Illustrative OCT scan of phantom with its borders indicated by cyan lines and ROI marked with red lines.

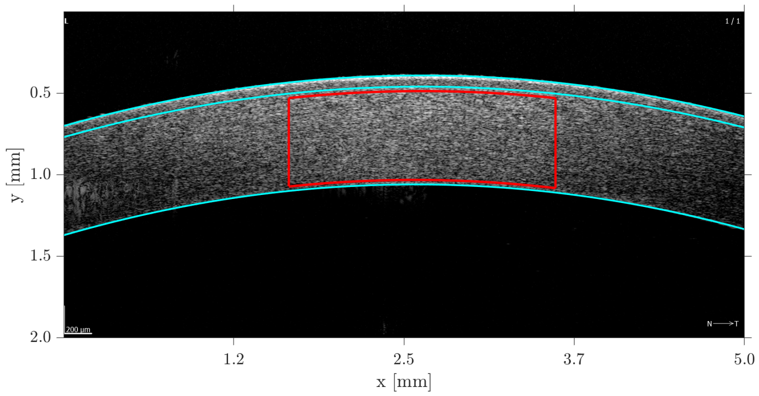

FIGURE 2.4: Illustrative OCT scan of porcine cornea from the *ex-vivo* study with epithelium, Bowman’s layer and endothelium indicated by cyan lines and ROI marked with red lines.

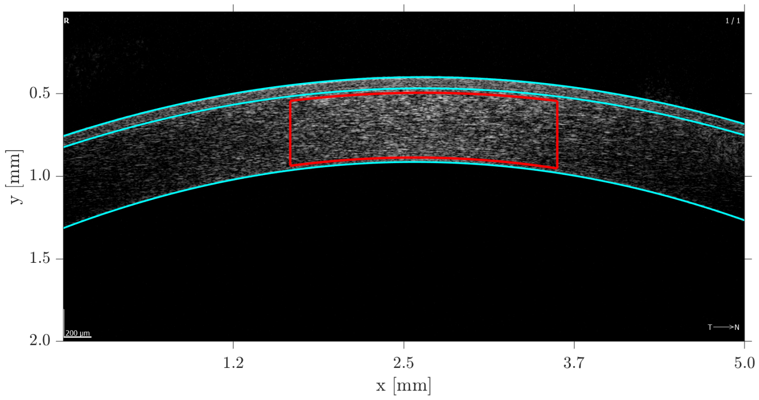

FIGURE 2.5: Illustrative OCT scan of human cornea from the *in-vivo* study with epithelium, Bowman’s layer and endothelium indicated by cyan lines and ROI marked with red lines.

statistical model selection. The first option is based on GoF, that can be construed as an arbitrary measure of difference between, e.g., PDF and kernel density estimator calculated from pixel values. This measure can be also based on other distribution characteristics, such as cumulative distribution function (CDF) or characteristic function (CF). The second approach for speckle model selection involves using distributions, which are theoretically justified (described in chapter 1.2), without paying attention to their GoF to experimental data.

First, the evaluation of GoF for different distributions is presented in this work. It is defined as a mean square error between PDFs of the distributions and kernel density estimator calculated for pixel values from the ROI in OCT images. A set of distributions, selected based on the literature, is assessed for the suitability for speckle modelling. The considered distributions are presented below along with their PDFs.

(i) Burr type XII (hereinafter referred as Burr3)

$$p(x;a,\nu,c) = \frac{\nu c}{a}\left(\frac{x}{a}\right)^{c-1}\left(1+\left(\frac{x}{a}\right)^{c}\right)^{-(\nu+1)}, \quad x>0, \tag{2.1}$$

where a is a scale parameter and ν and c are two shape parameters.

(ii) Burr type XII with one of its shape parameters, c, set as 2 (hereinafter referred as Burr2)

$$p(x;a,\nu) = \frac{2\nu x}{a^2}\left(1+\left(\frac{x}{a}\right)^{2}\right)^{-(\nu+1)}, \quad x>0, \tag{2.2}$$

where a is a scale parameter and ν is a shape parameter.

(iii) gamma

$$p(x;a,\nu) = \frac{1}{a^{\nu}\Gamma(\nu)}x^{\nu-1}e^{-x/a}, \quad x>0, \tag{2.3}$$

where a is a scale parameter, ν is a shape parameter and $\Gamma(\cdot)$ is the gamma function.

(iv) generalized gamma

$$p(x;a,\nu,c) = \frac{px^{\nu c-1}}{a^{\nu c}\Gamma(\nu)}\cdot e^{-(x/a)^{c}}, \quad x>0, \tag{2.4}$$

where a is a scale parameter, ν and c are shape parameters and $\Gamma(\cdot)$ is the gamma function.

(v) K

$$p(x;a,\nu) = \frac{2}{a\Gamma(\nu+1)}\left(\frac{x}{2a}\right)^{\nu+1}K_{\nu}\left(\frac{x}{a}\right), \quad x>0, \tag{2.5}$$

where a is a scale parameter, ν is a shape parameter and $K_{\nu}(\cdot)$ is the modified Bessel function of the second kind of order ν.

(vi) Nakagami

$$p(x;a,\nu) = \left(\frac{\nu}{a}\right)^{\nu} \frac{2}{\Gamma(\nu)} x^{(2\nu-1)} e^{x^2(-\nu/a)}, \quad x > 0\,, \tag{2.6}$$

where a is a scale parameter and ν is a shape parameter.

(vii) Rayleigh

$$p(x;\sigma) = \frac{x}{\sigma^2} e^{(-x^2/2\sigma^2)}, \quad x > 0\,, \tag{2.7}$$

where σ is a scale parameter.

(viii) Weibull

$$p(x;a,\nu) = \frac{\nu}{a}\left(\frac{x}{a}\right)^{\nu-1} e^{-(x/a)^{\nu}}, \quad x > 0\,, \tag{2.8}$$

where a is a scale parameter and ν is a shape parameter.

The distributions fitting was based on the estimation of their parameters for pixel values from ROI. For the most of the distributions (Burr3, gamma, generalized gamma, Nakagami, Rayleigh, Weibull) the maximum likelihood estimation (MLE) was performed. For the K distribution the parameters were estimated using the method of Raghavan [108]. The Burr2 distribution parameters were estimated using self-developed equations based on the sample mean and sample median of the Burr3 distribution. Using equations presented in [109] and setting the value of the shape parameter c equal to 2, the scale parameter estimator takes the form

$$\hat{a} = \frac{x_M}{\sqrt{2^{1/\hat{\nu}} - 1}}, \tag{2.9}$$

where x_M is a sample median and $\hat{\nu}$ is an estimator of the shape parameter of Burr2 distribution. To obtain the value of the scale parameter described above, the estimator of the shape parameter ν needs to be calculated numerically first, using following equation

$$\overline{x} = \frac{x_M}{2\sqrt{2^{1/\hat{\nu}} - 1}} \beta\left(\frac{1}{2}, \hat{\nu} - \frac{1}{2}\right), \tag{2.10}$$

where $\overline{x}$ is a sample mean, x_M is a sample median, and $\beta(\cdot)$ is the beta function.

To prove the validity of proposed method for the estimation of Burr2 distribution parameters, random samples of different size from the Burr2 distribution were generated. For that purpose a MATLAB function, allowing generation of random sample from Burr3 distribution, was used with a shape parameter c set as 2. After generating the random sample for $a = 0.5$ and $\nu = 1.5$, the parameters estimation was performed using proposed method.

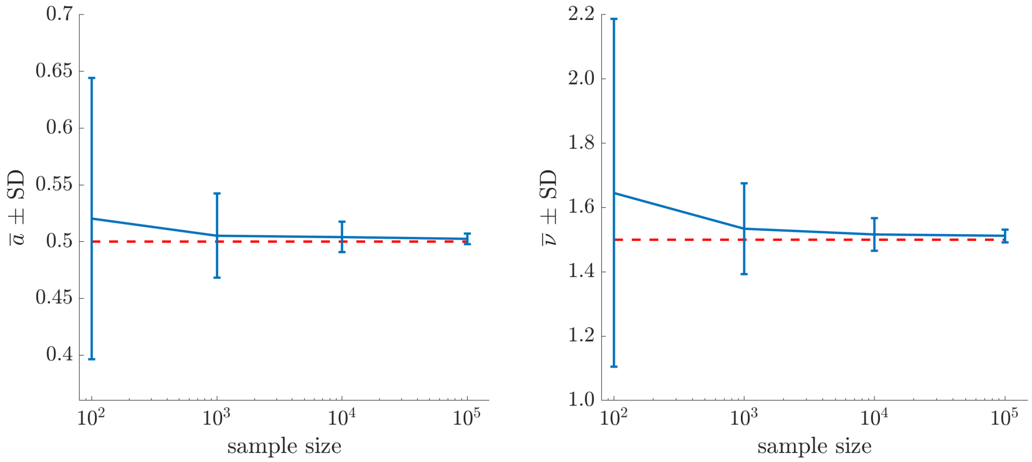

FIGURE 2.6: Mean values of the estimators of Burr2 distribution parameters with error bars denoting standard deviation for different sample sizes. Red dashed lines indicate a set value of parameter used for generating a random sample.

Figure 2.6 shows the mean values of estimators together with error bars. It proves that proposed estimators asymptotically achieve the set parameter value and the estimator values dispersion, expressed as standard deviation, decreases with the increasing sample size, suggesting that the proposed estimator is unbiased and consistent. In case of presented here analysis of OCT scans, the sample size for Burr2 parameter estimation is of the order of 10^5.

For the analysis of OCT images from the study on porcine eyeballs, the gamma distribution was selected as a statistical model of the amplitude of speckle field on the grounds of the theory presented in chapter 1.2.2, as OCT devices have scanning apertures, which are thought to average the speckle pattern. For this distribution, an additional study was performed to assess the influence of averaging of OCT images on the distributional parameters. The methodology and the results of this study are presented in Appendix A. It was revealed in this study that the background noise in OCT images follows gamma distribution. Based on these results, in Appendix B a product distribution of two gamma distributed random variables is proposed for corneal OCT speckle modelling. The PDF of such distribution as well as estimators of its parameters were calculated and next, simulations were performed to evaluate the obtained estimators. Finally, the proposed model was validated on corneal OCT images of 5 subjects in an *in-vivo* study. It was shown that parameter estimation is not accurate for corneal OCT speckle and that the considered model is too intricate to be practical in speckle modelling, pointing to simpler models to be more beneficial.

2.2.3 Spatial maps of distribution parameters

For the OCT images of porcine eyes, the spatial changes in distributional parameters were of interest. To visually evaluate them, the maps of gamma distribution parameter values were prepared for the corneal stroma, according to the scheme in figure 2.7. At the beginning, the Bowman's layer and epithelium were delineated, as they comprise stroma borders. Next, the window of size 41×41 pixels was scanning the stroma image with a step of 10 pixels in both horizontal and vertical directions. For each window position, the MLE estimators of gamma distribution parameters were calculated for pixel values from the window. These estimates were set as a value of central pixel for a particular window position. The window size was chosen empirically, having regard to a requirement for the sufficient number of pixel values within the window to accurately estimate gamma distribution parameters. The step of the moving window was a compromise between the resolution of the map resolution and the time needed to calculate the parameter values for the map.

As a first and basic approach to the analysis of the maps, the mean values of shape and scale parameters of the gamma distribution were calculated within the ROI. The ROI was encompassing the central 2 mm (600 pixels) horizontally and the entire thickness of the stroma vertically. After visual assessment of the maps, spatial differences in parameter values for increasing IOP were observed. Hence, the ROI was also divided in half to calculate mean parameter values for the anterior and posterior part of stroma, as it is presented in figure 2.7c.

2.2.4 Non-parametric approach

There are different approaches in literature for the normalization of the pixel values representing amplitude of the speckle field. The amplitude normalization is done by dividing it by its root mean square (RMS) value, described as $\sqrt{\langle A^2 \rangle}$ [57], [61], [110]. For some distributions amplitude normalization leads to constant values of the scale parameter. Such situation is observed also for the Rayleigh distribution as presented below.

The scale parameter of the Rayleigh distribution can be estimated using various methods. The most frequently used is MLE, which gives estimator in the form

$$\hat{\sigma}_{\mathrm{MLE}} = \sqrt{\frac{1}{2n} \sum_{i=1}^{n} X_i^2}, \tag{2.11}$$

where X_i, $i = 1, 2, \ldots, n$ are discrete samples of the random variable X which denotes speckle amplitude and n is the number of samples. For the normalized

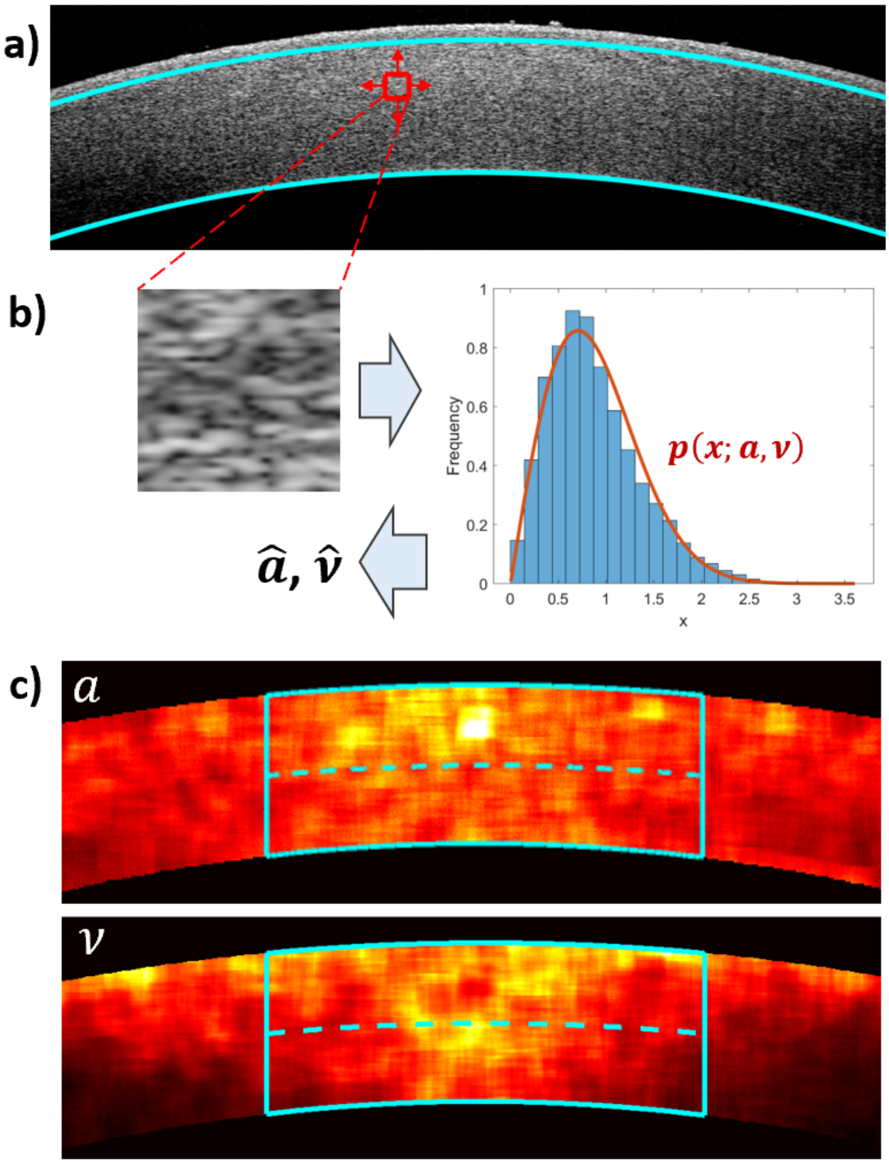

FIGURE 2.7: The scheme of preparation of the spatial maps of gamma distribution parameters for the corneal stroma. (a) The moving window is scanning the OCT image of cornea within the borders designated by the Bowman's layer and the endothelium (cyan lines). (b) The gamma distribution shape (ν) and scale (a) parameters are estimated using pixel values within the scanning window in each position. (c) The spatial maps of gamma distribution parameters are prepared by setting the parameter estimates as values of central pixel in each window position. Cyan lines indicate ROI selected for statistical analysis.

amplitude the above-mentioned estimator reduces to

$$\hat{\sigma}_{\text{MLE}} = \sqrt{\frac{1}{2n} \cdot \frac{1}{\frac{1}{n}\sum_{i=1}^{n} X_i^2} \cdot \sum_{i=1}^{n} X_i^2} = \frac{\sqrt{2}}{2}, \tag{2.12}$$

so the Rayleigh distribution is obtained with the constant value of the scale parameter equal to $\sqrt{2}/2$, independent of the sample distribution.

In order to verify the above-mentioned results, another estimation method, proposed by Ardianti et al. [111], was used for the validation. That is Bayes method with the estimator of the form

$$\hat{\sigma}_{\text{Bayes}} = \frac{\sqrt{2}\Gamma(n+2)}{2\Gamma\left(n+\frac{5}{2}\right)}\sqrt{\sum_{i=1}^{n} X_i^2}\,. \tag{2.13}$$

Again, for the normalized speckle amplitude following estimator is obtained

$$\hat{\sigma}_{\text{Bayes}} = \frac{\sqrt{2}\Gamma(n+2)}{2\Gamma\left(n+\frac{5}{2}\right)}\sqrt{\frac{1}{\frac{1}{n}\sum_{i=1}^{n} X_i^2}\cdot\sum_{i=1}^{n} X_i^2} = \frac{\sqrt{2}}{2}\cdot\frac{\Gamma(n+2)}{\Gamma\left(n+\frac{5}{2}\right)}\cdot\sqrt{n}\,. \tag{2.14}$$

The estimator in this form asymptotically for $n \to \infty$ approaches $\sqrt{2}/2$.

Above results show that regardless of the estimation method, for any normalized random sample, the scale parameter σ of the Rayleigh distribution has constant value. Due to this property, in this work the Rayleigh distribution with $\sigma = \sqrt{2}/2$ is used in non-parametric approach as a benchmark.

Having such a benchmark, some measures needed to be defined to evaluate the difference between it and empirical distribution of the sample. They were determined based on presented below characteristics of empirical distribution of inverse-log transformed pixel values from ROIs in OCT images, treated as a random variable X.

- Empirical cumulative distribution function (eCDF) [112]

$$\text{eCDF} = \frac{1}{n}\sum_{i=1}^{n} \mathbf{1}\{X_i \leq t\}\,, \tag{2.15}$$

  where n is the number of samples and $\mathbf{1}\{X_i \leq t\}$ is the indicator of the event that the value of a random variable X_i is less than or equal to t.

- Kernel density estimator (KDE) [113]

$$\text{KDE} = \frac{1}{n}\sum_{i=1}^{n} \frac{1}{h}\mathcal{K}\left(\frac{x-X_i}{h}\right), \tag{2.16}$$

  where $\mathcal{K}(\cdot)$ is the non-negative kernel function and h is the bandwidth of the estimator. The kernel function was of Gaussian type with the bandwidth $h = (0.75n)^{(-1/5)}\hat{\sigma}_x$, where $\hat{\sigma}_x$ is the sample standard deviation. For KDE calculated from the sample, a boundary effect, resulting from the limitation of the pixel values only to non-negative values, had to be corrected by excluding KDE values for abscissa less than 0.05 [114].

- Empirical characteristic function (eCF) [115]

$$\mathrm{eCF} = \frac{1}{n}\sum_{i=1}^{n} e^{jtX_i}, \quad j = \sqrt{-1}\,. \tag{2.17}$$

To quantify the differences between empirical distributions and the benchmark distribution (BD), three distances were defined as follows:

- Kolmogorov–Smirnov distance between eCDF and the CDF of the benchmark distribution [116]

$$D_{\mathrm{KS}} = \sup_x \left|\mathrm{eCDF}(x) - \mathrm{CDF}_{\mathrm{BD}}(x)\right|, \tag{2.18}$$

  where $\sup_x$ is the supremum of the set of distances across all x values,

- mean square error (MSE) distance, between KDE and the PDF of the benchmark distribution

$$D_{\mathrm{MSE}} = \frac{1}{n}\sum_{i=1}^{n}(\mathrm{KDE}(x_i) - \mathrm{PDF}_{\mathrm{BD}}(x_i))^2, \tag{2.19}$$

- maximum mean discrepancy (MMD) distance, between eCF and the CF of the benchmark distribution [117]

$$D_{\mathrm{MMD}} = \left\|\frac{1}{n}\sum_{i=1}^{n}\mathrm{eCF}(x_i) - \frac{1}{n}\sum_{i=1}^{n}\mathrm{CF}_{\mathrm{BD}}(x_i)\right\|. \tag{2.20}$$

Additionally, for the pixel values from the ROI the contrast ratio was calculated due to the following definition [52]

$$\mathrm{CR} = \frac{\hat{\sigma}_x}{\overline{x}}, \tag{2.21}$$

where $\overline{x}$ is the sample mean. The calculated values of contrast ratio could be then compared with the theoretical value for Rayleigh distribution, approximately equal to 0.52.

2.2.5 Biometric parameters

In the *ex-vivo* study on porcine eyeballs, the measurements of the eye biometric parameters were taken as it was described in section 2.1.2. Here, the explanation of measured parameters will be presented.

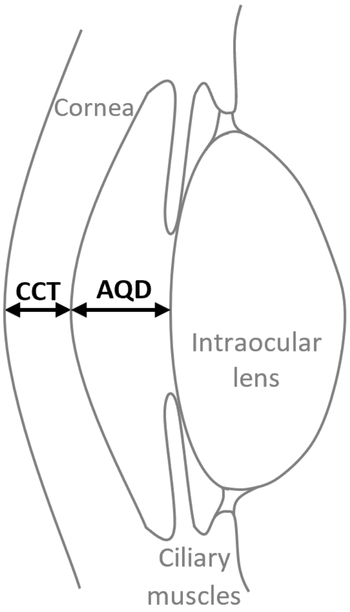

FIGURE 2.8: Scheme of the anterior chamber of the eye with CCT and AQD marked (author's own artwork).

- Central corneal thickness (CCT)

  CCT is the axial distance between the anterior and posterior corneal surfaces, measured in the most anterior point of the cornea, i.e., apex (see figure 2.8) [118], [119].

- Aqueous depth (AQD)

  The AQD is the axial distance measured between the central corneal endothelium and the centre of anterior surface of the intraocular lens (see figure 2.8) [120].

- Axial length (AL)

  The AL is the axial length of the eyeball, which is measured in a straight line between anterior corneal surface and the outer layer of the retina, i.e., retinal pigment epithelium [121].

- Mean equivalent spherical power (M) and astigmatic components of Jackson cross cylinder (J0 and J45)

  These parameters are calculated based on corneal keratometric parameters, so a few essential definitions will be presented here. Two principal meridians of the eye need to be characterized. Eye meridians correspond to the lines of longitude on a globe, with the pupil centre treated as a pole. The steeper meridian (K1 in figure 2.9) is where the corneal radius of curvature has the smallest value and the flat meridian (K2 in figure 2.9) is where the corneal radius of curvature is the greatest. The angle between

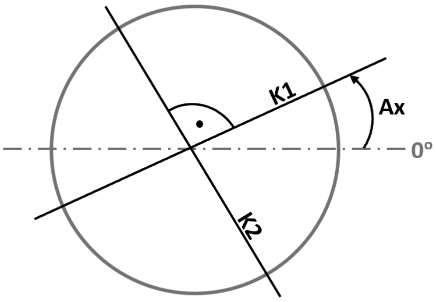

FIGURE 2.9: Schematic representation of the keratometric parameters. The circle represents a front view at the eye with a pupil in the center, K1 and K2 are steeper and flat meridians of the anterior corneal surface, respectively, and Ax is an angle between the 0° meridian and the steeper meridian.

the 0° meridian (horizontal line passing through the pupil center) and the steeper meridian, for which the optical power is the highest, is called astigmatism axis (Ax in figure 2.9). The orthogonality of K1 and K2 meridians is assumed, which is known as regular astigmatism [122].

Next, the refractive power F is calculated for the steeper and flat meridian using formula:

$$F = \frac{n_1 - n}{R_C}[\mathrm{D}]\,, \tag{2.22}$$

where n_1 is the standard keratometric index of refraction equal to 1.3375, corresponding to the combination of the refractive indices of the cornea and aqueous humor. The refractive index of air is denoted as n and equal to 1 and R_C is the anterior corneal radius of curvature (in meters) for the considered meridian [123].

Dioptric power of the eye is usually represented in terms of sphere and cylinder. The sphere indicates the refractive power assuming the equality of eye radii of curvature for all meridians and the cylinder indicates the refractive power connected with astigmatism, being the difference between the greatest and the weakest power of the eye. Using the notation with negative cylinder and denoting the refractive power for the K1 meridian as F_1 and for the K2 meridian as F_2, the sphere (S) and cylinder (C) powers are described by the following formulas

$$S = (F_1 + F_2)/2\,, \tag{2.23}$$

$$C = F_1 - F_2\,. \tag{2.24}$$

It is useful to represent the sphero-cylindrical refractive error using three fundamental dioptric components (M, J_0, J_{45}). The first component, M, is a spherical equivalent of the refractive error. After removing the spherical component, a Jackson cross cylinder (JCC) is obtained, which is equal to the power J of the conventional cylinder at axis Ax+90° crossed with a cylinder $-J$ at axis Ax. The astigmatic component is conventionally described as a JCC of power J at axis Ax. The JCC can be resolved into the sum of 2 JCC lenses with power J_0 at axis 0° and J_{45} at axis 45°. To calculate these components the formulas presented below can be used.

$$M = S + \frac{C}{2}, \tag{2.25}$$

$$J_0 = -\frac{C}{2}\cos(2\mathrm{Ax}), \tag{2.26}$$

$$J_{45} = -\frac{C}{2}\sin(2\mathrm{Ax}), \tag{2.27}$$

where Ax is the astigmatism axis given in radians and providing that the cylinder notation is with a minus sign [124], [125].

2.2.6 Statistical analysis

In the statistical analysis of the results from the study on porcine eyeballs, gamma distribution parameters in a parametric approach, statistical distances and CR in a non-parametric approach and ocular biometric parameters were taken into consideration. To evaluate how these parameters vary with IOP in Experiment 1 or with time in Experiment 2, a one-way repeated measures analysis of variance (rmANOVA) was applied. Post-hoc analysis, using paired t-test, was performed to evaluate differences in mean values of parameters between consecutive IOP levels or the adjacent time points. There was no correction in the post-hoc analysis because a large number of tests were carried out (21 for 7 considered levels of IOP) without a preplanned hypothesis [126]. The results of this analysis are presented in the plots of the mean values of parameters in a form of horizontal bars with asterisks denoting statistical significance of test results (* $p < 0.05$; ** $p < 0.01$; *** $p < 0.001$).

In the *ex-vivo* study on porcine eyeballs, partial correlation analysis with IOP (Experiment 1) or time (Experiment 2) set as a control variable, was performed for the parameters of the gamma distribution and ocular biometry. In the *in-vivo* study on human corneas, Pearson correlation coefficient (R) was computed to assess if distributional parameters as well as statistical distances and CR values are correlated with IOP. Also, in correlation analyses p-values are presented for testing the hypothesis that there is no correlation between analysed variables.

Chapter 3

Results

3.1 Phantom study

3.1.1 Parametric approach

In this approach the goodness of fit was first assessed for the considered set of distributions for nine phantoms of different concentrations (C_1, C_2, ..., C_9). Based on the results presented in figure 3.1, the best fit to pixel values is obtained for the generalized gamma distribution. Also gamma, Weibull and both Burr distributions provide a comparable good fit. It is worth noting that the fit of all presented distributions remains at a similar level for higher concentrations of scattering particles (C_9–C_6) and then it gradually deteriorates (GoF values increase) with decreasing scatterer density. The greatest rise in GoF values for the concentrations from C_6 to C_1 is observed for the Rayleigh distribution.

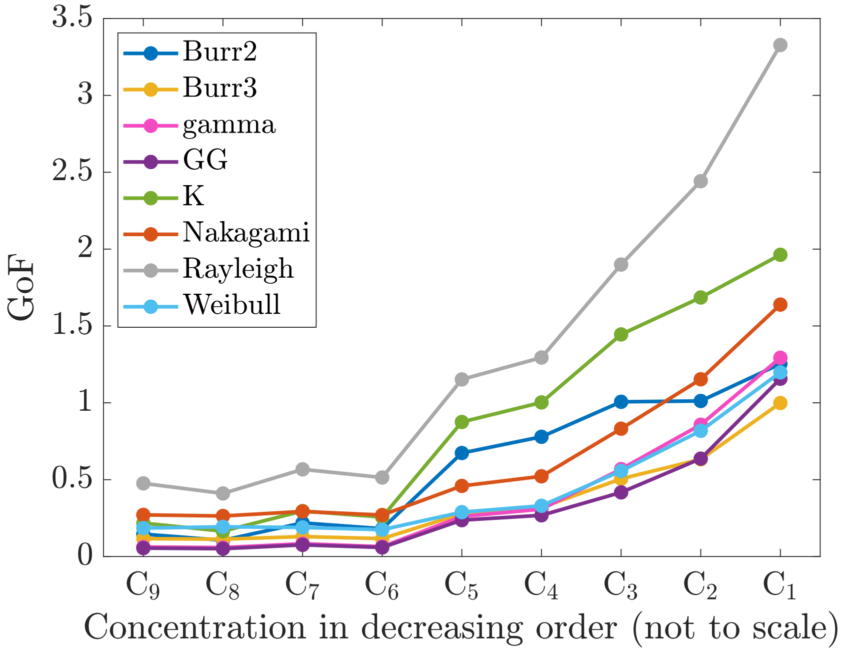

FIGURE 3.1: Values of GoF of considered distributions fitted to pixel values from the ROI in OCT images of phantoms. GG denotes generalized gamma distribution.

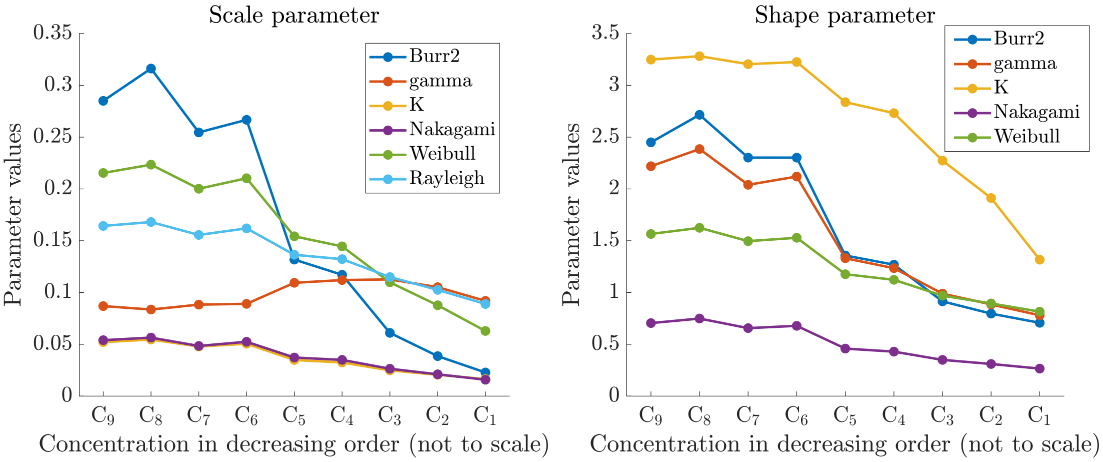

FIGURE 3.2: Values of the scale and shape parameters of considered two-parameter distributions for decreasing concentration of scattering particles in the phantom study.

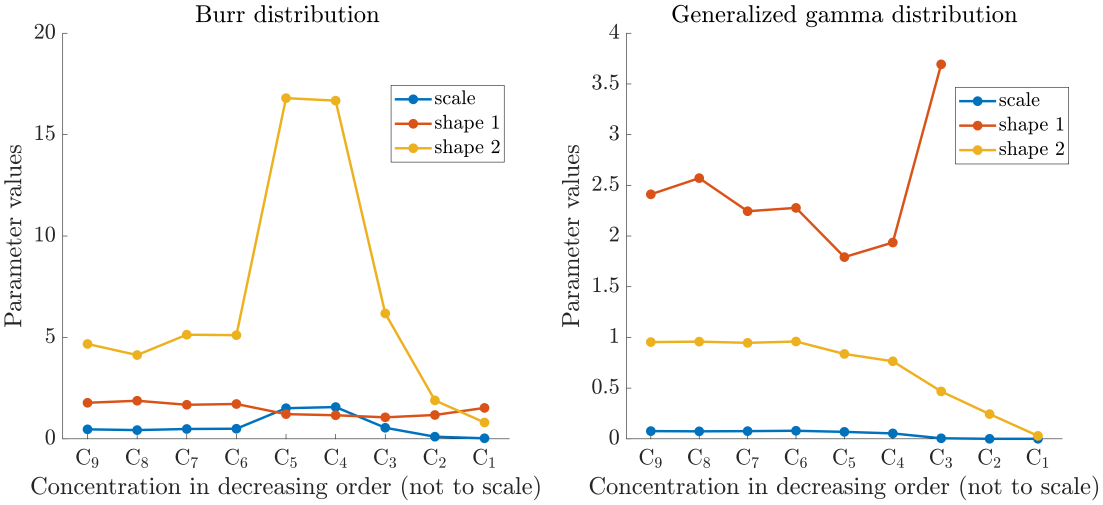

FIGURE 3.3: Values of the parameters of considered three-parameter distributions for decreasing concentration of scattering particles in the phantom study.

Values of the parameters of the considered distributions are presented in figures 3.2 and 3.3. Despite good fitting of the three-parameter distributions, their parameters show weak trend with scatterer concentration. Moreover, the shape 1 parameter of the generalized gamma distribution for two lowest concentrations encountered huge values, which were removed from the plot for better visualization. For all considered distributions with two parameters, the shape parameter shows descending trend with decreasing concentration of scatterers in phantoms, with a saturation for concentrations from C_9 to C_6. The scale parameter also shows dependence on scatterer concentration for different distributions, especially it is the most pronounced for the Burr2 distribution.

For the two-parameter distributions, the parameters were also estimated for the speckle amplitude after normalization, as described in chapter 2.2.4. The results are presented in figure 3.4. Comparing to figure 3.2, for most

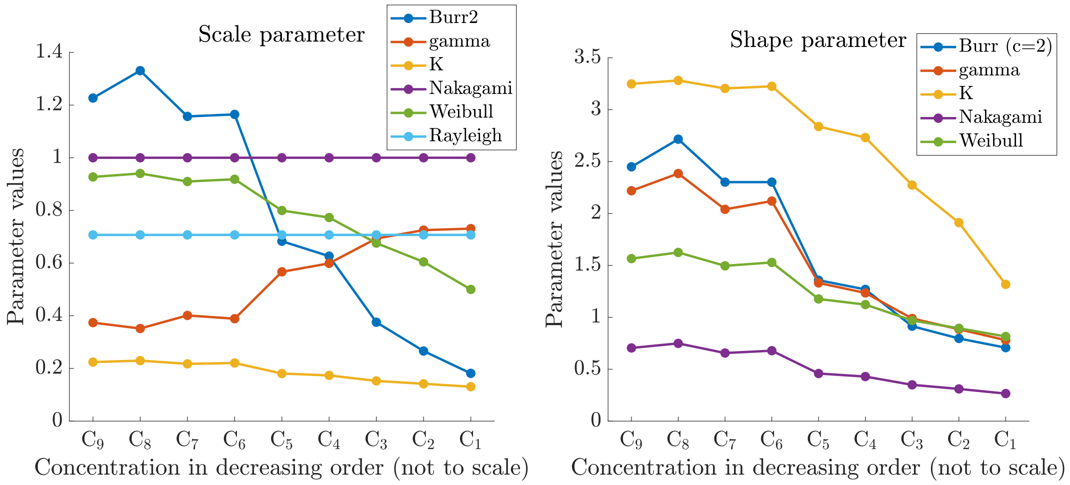

FIGURE 3.4: Values of scale and shape parameters of the considered two-parameter distributions estimated for the normalized speckle amplitude in OCT images of phantoms for decreasing concentration of scattering particles.

distributions there are only slight differences in the changes of parameter values with concentration of scattering particles. The Nakagami and Rayleigh distributions are two exceptions for which the scale parameter, estimated for normalized amplitude, has constant value, regardless of scatterer density.

3.1.2 Non-parametric approach

The consistency of the Rayleigh distribution scale parameter estimated for normalized speckle amplitude was used as a foundation for the development of the non-parametric approach, explained in chapter 2.2.4. In this approach, all considered statistical distances in figure 3.5 show similar trend for decreasing scatterer concentration. For the concentrations from C_9 to C_6 the D_{MSE}, D_{KS} and D_{MMD} distances have almost constant value of about 0.1. For the lower concentrations their values are increasing, so the empirical distribution of speckle field amplitude is deviating from the benchmark Rayleigh distribution. Similar trend is observed for CR, which values for concentrations from C_9 to C_6 are slightly larger than theoretical value of 0.52 for the Rayleigh distribution and from the C_6 concentration it starts to increase to finally approach the value of about 1.45.

3.2 *Ex-vivo* study on porcine eyes

3.2.1 Parametric approach

In the *ex-vivo* study on porcine eyeballs GoF was also first evaluated for the analysed set of distributions. The results are presented in figure 3.6 and show

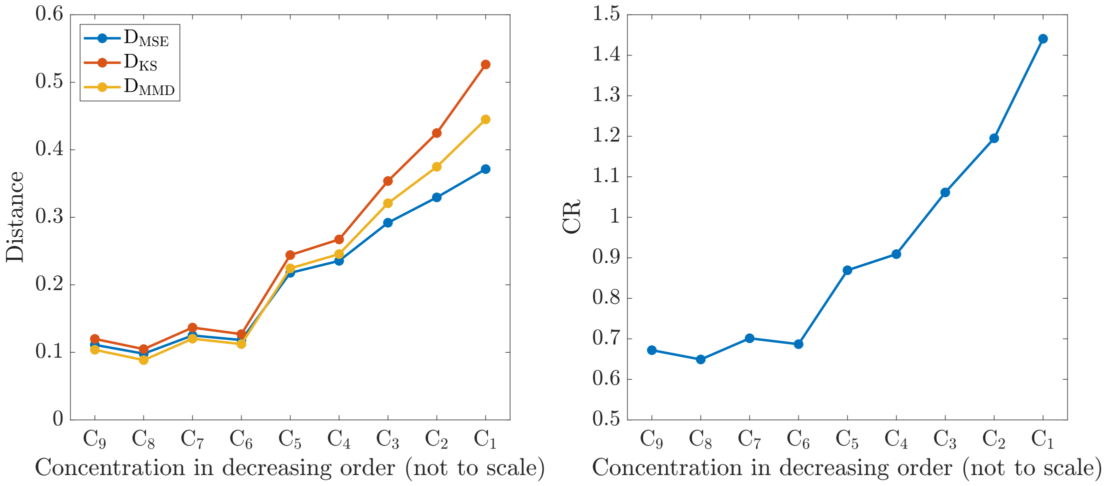

FIGURE 3.5: Values of statistical distances (left) and contrast ratio (right) for decreasing concentration of scattering particles in the phantom study.

that both three-parameter distributions (Burr3 and generalized gamma) best fit the experimental data. Slightly increasing trend of GoF with increasing IOP is observed for almost all distributions, except gamma and K distribution. For the Rayleigh distribution changes of GoF values with IOP are the highest.

For non-normalized pixel values from ROIs in OCT images, the values of parameters of considered distributions were estimated. One-way repeated measures ANOVA (rmANOVA) was used to evaluate if these parameters vary with IOP in Experiment 1 or with time in Experiment 2. The results are presented in table 3.1. Statistically significant changes with IOP in Experiment 1 are observed for all distributions, except for the shape 2 parameter of Burr3 distribution. In Experiment 2 the changes in values of parameters are significant for both parameters of Burr2, gamma, K and Weibull distributions, for the shape parameter of the Nakagami distribution, and for one of the shape parameters for Burr3 and generalized gamma distributions.

For one of the distributions the analysis of parameters was performed to assess the potential of using them as markers of changes in corneal speckle statistics induced by elevated IOP. Gamma distribution was selected from the considered set of distributions on the basis of speckle theory, as it was described in chapter 2.2.3, and also taking into account that both parameters of this distribution change significantly with IOP and time (see table 3.1).

Gamma distribution parameters were estimated for non-normalized pixel values and results are presented in figure 3.7 for two experiments performed on porcine eyeballs. Statistical significance of differences between values of parameters was evaluated using paired t-test for consecutive IOP levels in Experiment 1 or consecutive time points in Experiment 2. The shape parameter of gamma distribution shows similar, declining trend in both experiments. Better differentiation between experiments is observed for the scale parameter,

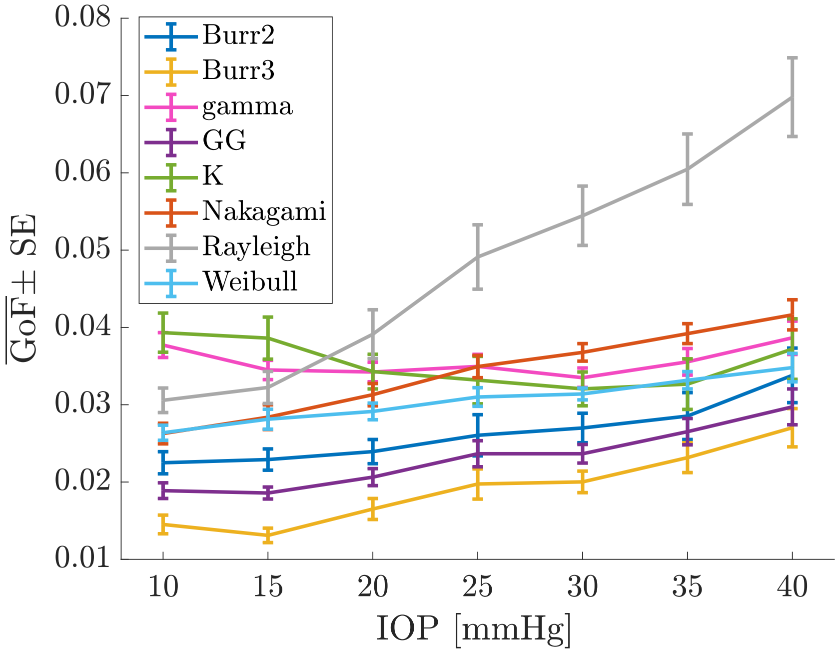

FIGURE 3.6: Mean values (± standard error) of the GoF of considered distributions fitted to pixel values from the ROI in OCT images of porcine corneas for increasing IOP. GG denotes generalized gamma distribution.

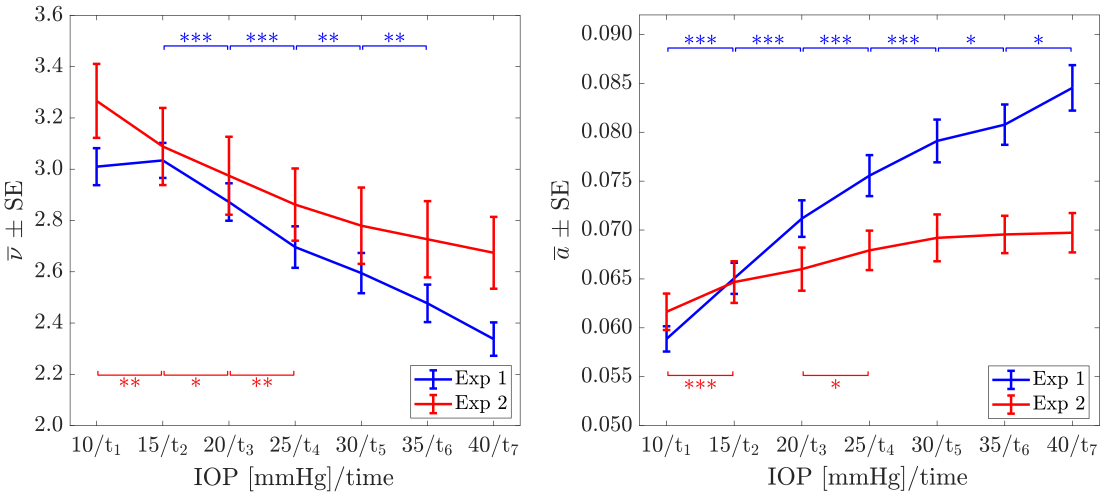

FIGURE 3.7: Mean values (± standard error) of gamma distribution shape (ν) and scale (a) parameter, estimated for pixel values within the ROI in OCT images of porcine corneas, as functions of IOP (Experiment 1) or time (Experiment 2).

which values are increasing with statistically significant differences for all adjacent IOP levels in Experiment 1. In Experiment 2 the changes in parameter values are lower with significant differences only between t_1 and t_2 and also t_3 and t_4 time points.

TABLE 3.1: Results of rmANOVA for the changes of parameters of considered distributions with IOP or time in Experiment 1 and Experiment 2, respectively, in the study on porcine eyeballs.

Distribution	Parameter	rmANOVA	
		Experiment 1	Experiment 2
Burr2	scale	$F = 15.59, p < 0.001$	$F = 7.59, p < 0.001$
	shape	$F = 17.84, p < 0.001$	$F = 7.69, p < 0.001$
Burr3	scale	$F = 8.17, p < 0.001$	$F = 0.69, p = 0.658$
	shape 1	$F = 28.59, p < 0.001$	$F = 9.21, p < 0.001$
	shape 2	$F = 1.89, p = 0.088$	$F = 0.72, p = 0.639$
gamma	scale	$F = 86.90, p < 0.001$	$F = 17.97, p < 0.001$
	shape	$F = 37.73, p < 0.001$	$F = 21.20, p < 0.001$
generalized gamma	scale	$F = 9.12, p < 0.001$	$F = 0.96, p = 0.459$
	shape 1	$F = 6.49, p < 0.001$	$F = 1.31, p = 0.270$
	shape 2	$F = 11.44, p < 0.001$	$F = 5.74, p < 0.001$
K	scale	$F = 10.87, p < 0.001$	$F = 5.56, p < 0.001$
	shape	$F = 28.33, p < 0.001$	$F = 14.04, p < 0.001$
Nakagami	scale	$F = 27.30, p < 0.001$	$F = 1.94, p = 0.091$
	shape	$F = 39.78, p < 0.001$	$F = 23.46, p < 0.001$
Rayleigh	scale	$F = 29.09, p < 0.001$	$F = 2.18, p = 0.059$
Weibull	scale	$F = 15.71, p < 0.001$	$F = 3.93, p = 0.003$
	shape	$F = 41.34, p < 0.001$	$F = 26.18, p < 0.001$

3.2.2 Ocular biometric parameters

In experiments on porcine eyeballs ocular biometry measurements were taken at each IOP level in Experiment 1 and for each time point in Experiment 2. To evaluate changes in values of biometric parameters, rmANOVA was utilized, and the results are presented in table 3.2. Statistically significant changes of CCT, AQD and M are observed in Experiment 1 and CCT and AL in Experiment 2.

Figures 3.8 and 3.9 present changes in values of biometric parameters with IOP (Experiment 1) or with time (Experiment 2). Statistically significant decrease of CCT is observed for IOP from 10 to 20 mmHg in Experiment 1 and between t_1 and t_2 time points in Experiment 2. The values of AQD parameter slightly increase in both experiments and declining trend is observed for AL parameter only in Experiment 2. For IOP from 10 to 20 mmHg also values of M parameter decrease significantly. Astigmatic components of Jackson cross cylinder, J_0 and J_{45}, remain at the similar level during both experiments.

TABLE 3.2: Results of rmANOVA for ocular biometric parameters in Experiment 1 and Experiment 2 in the study on porcine eyes.

	CCT	AQD	AL	M	J_0	J_{45}
Experiment 1	$F = 3.24$ $p = 0.005$	$F = 7.44$ $p < 0.001$	$F = 0.45$ $p = 0.841$	$F = 9.33$ $p < 0.001$	$F = 0.32$ $p = 0.928$	$F = 0.38$ $p = 0.888$
Experiment 2	$F = 2.39$ $p = 0.040$	$F = 1.48$ $p = 0.203$	$F = 5.15$ $p < 0.001$	$F = 1.44$ $p = 0.218$	$F = 0.52$ $p = 0.792$	$F = 0.69$ $p = 0.659$

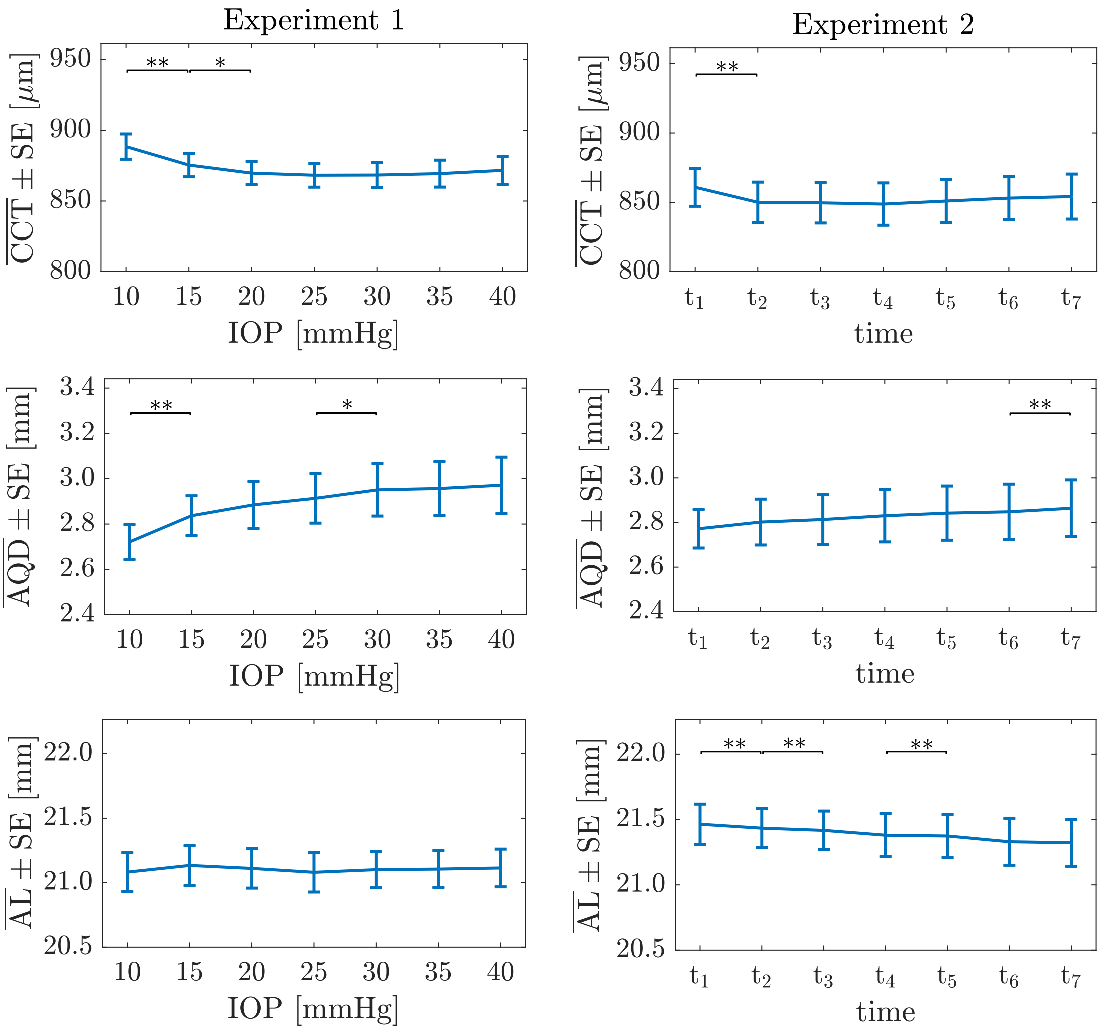

FIGURE 3.8: Mean values (± standard error) of ocular biometric parameters as functions of set IOP (Experiment 1, left panel) or time (Experiment 2, right panel).

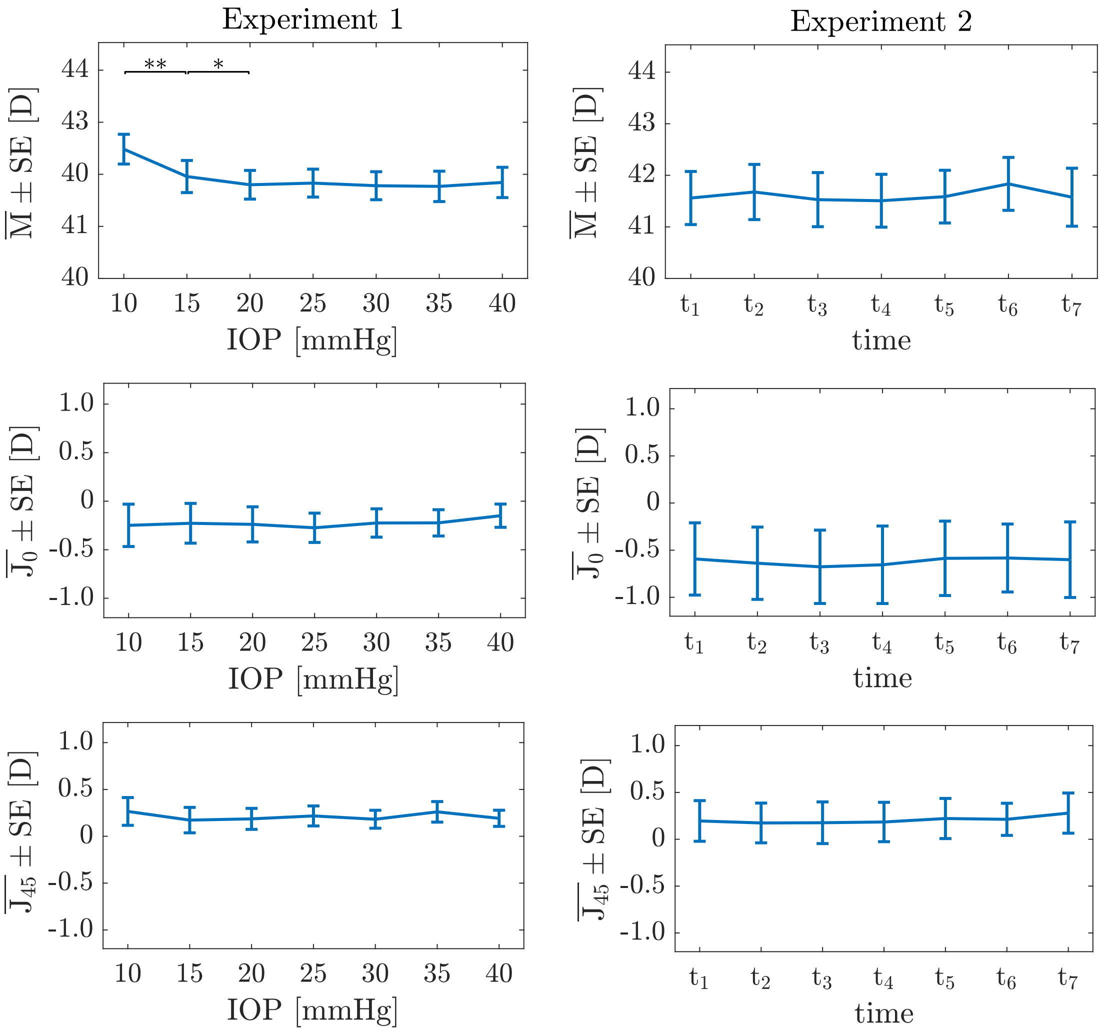

FIGURE 3.9: Mean values (± standard error) of the mean equivalent spherical power (M) and astigmatic components of the Jackson cross cylinder (J_0 and J_{45}) as functions of set IOP (Experiment 1, left panel) or time (Experiment 2, right panel).

Partial correlation analysis was performed for the parameters of gamma distribution and biometric parameters with IOP and time set as a control variable for the results from Experiment 1 and Experiment 2, respectively. In the analysis the sample size was taken into consideration for the evaluation of statistical significance of the results. Based on the work of Bujang and Baharum [127], in testing for zero correlation statistically significant values of correlation coefficient (in absolute terms) should be larger than 0.6 for the sample size of 23 in Experiment 1 and larger than 0.8 for the sample size of 10 in Experiment 2. According to that work, the obtained results, showed in table 3.3, do not show statistically significant correlations between considered parameters.

TABLE 3.3: Results of partial correlation analysis (partial correlation coefficient, ρ, and p-values for testing for zero correlation) between gamma distribution parameters and ocular biometric parameters with IOP and time set as a control variable for the results from Experiment 1 and Experiment 2, respectively.

	Experiment 1		Experiment 2	
	ν	a	ν	a
CCT	$\rho = 0.012$ $p = 0.880$	$\rho = -0.291$ $p < 0.001$	$\rho = -0.290$ $p = 0.016$	$\rho = 0.103$ $p = 0.401$
AQD	$\rho = 0.133$ $p = 0.094$	$\rho = -0.313$ $p < 0.001$	$\rho = 0.006$ $p = 0.960$	$\rho = -0.363$ $p = 0.002$
AL	$\rho = 0.208$ $p = 0.009$	$\rho = -0.088$ $p = 0.271$	$\rho = -0.174$ $p = 0.153$	$\rho = -0.313$ $p = 0.009$
M	$\rho = 0.015$ $p = 0.853$	$\rho = -0.157$ $p = 0.048$	$\rho = 0.150$ $p = 0.226$	$\rho = 0.331$ $p = 0.006$
J_0	$\rho = 0.027$ $p = 0.735$	$\rho = -0.009$ $p = 0.908$	$\rho = -0.512$ $p < 0.001$	$\rho = 0.193$ $p = 0.118$
J_{45}	$\rho = -0.114$ $p = 0.153$	$\rho = -0.056$ $p = 0.482$	$\rho = 0.396$ $p < 0.001$	$\rho = 0.291$ $p = 0.017$

3.2.3 Spatial maps of distribution parameters

Spatial maps of shape and scale parameter of gamma distribution are presented in figures 3.10 and 3.11, respectively, together with corresponding OCT scans of porcine corneas for IOP levels of 10, 20, 30 and 40 mmHg. These exemplary maps show the potential of such analysis of parameter values since changes in their spatial distribution with increasing IOP are evident. The values of both parameters are higher in the central cornea comparing to the periphery. For increasing IOP there is an evident rise of values of scale parameter. The shape parameter has higher values located more centrally comparing to scale parameter, but there is not obvious trend to clearly characterize the changes of parameter values. Differences in pixel values for OCT scans are more difficult to observe, but the spatial changes in pixel brightness for increasing IOP seem to be comparable rather to the spatial changes of the shape parameter values than to the maps of scale parameter.

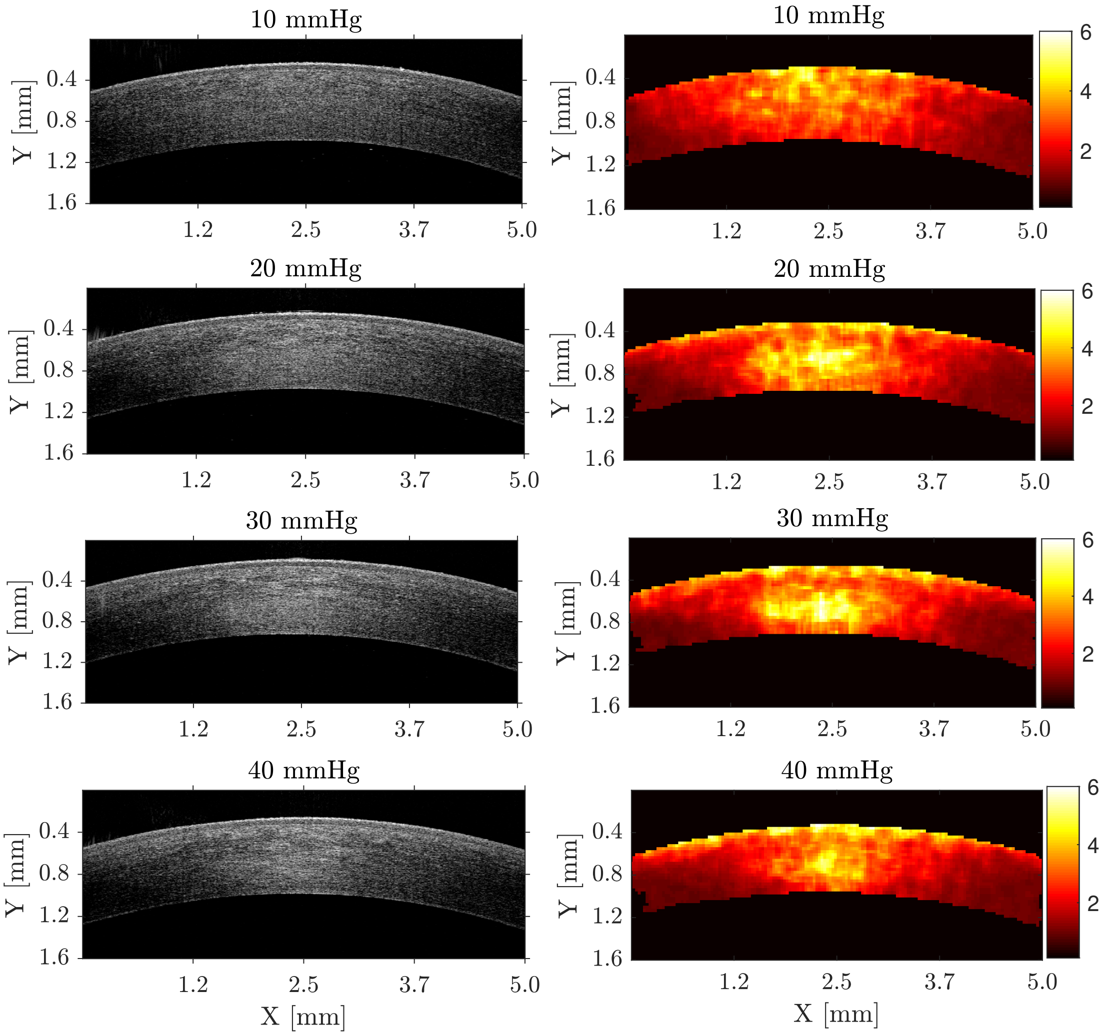

FIGURE 3.10: An example of spatial maps of the gamma distribution shape parameter (ν) together with corresponding OCT scans for four out of seven IOP levels in Experiment 1.

The visual evaluation of the maps gave information about spatial changes in speckle statistics, however, a quantitative analysis was required to obtain some measures of changes in parameter values. As a first approach for such analysis, mean values of parameters were calculated from the maps within the ROI presented in figure 2.7c. The calculations were performed for the ROI encompassing entire corneal thickness as well as for its anterior and posterior halves separately.

The results for the entire corneal thickness are presented in figure 3.12. They show similar trends as for the values of parameters estimated directly from pixel values in OCT scans (figure 3.7). In both cases there is an increase of shape parameter values between 10 and 15 mmHg while for the remaining IOP levels the decreasing trend of parameter values is observed. Statistically significant differences in scale parameter values occur for IOP from 10 to 30 mmHg in Experiment 1 and are almost not observed for Experiment 2.

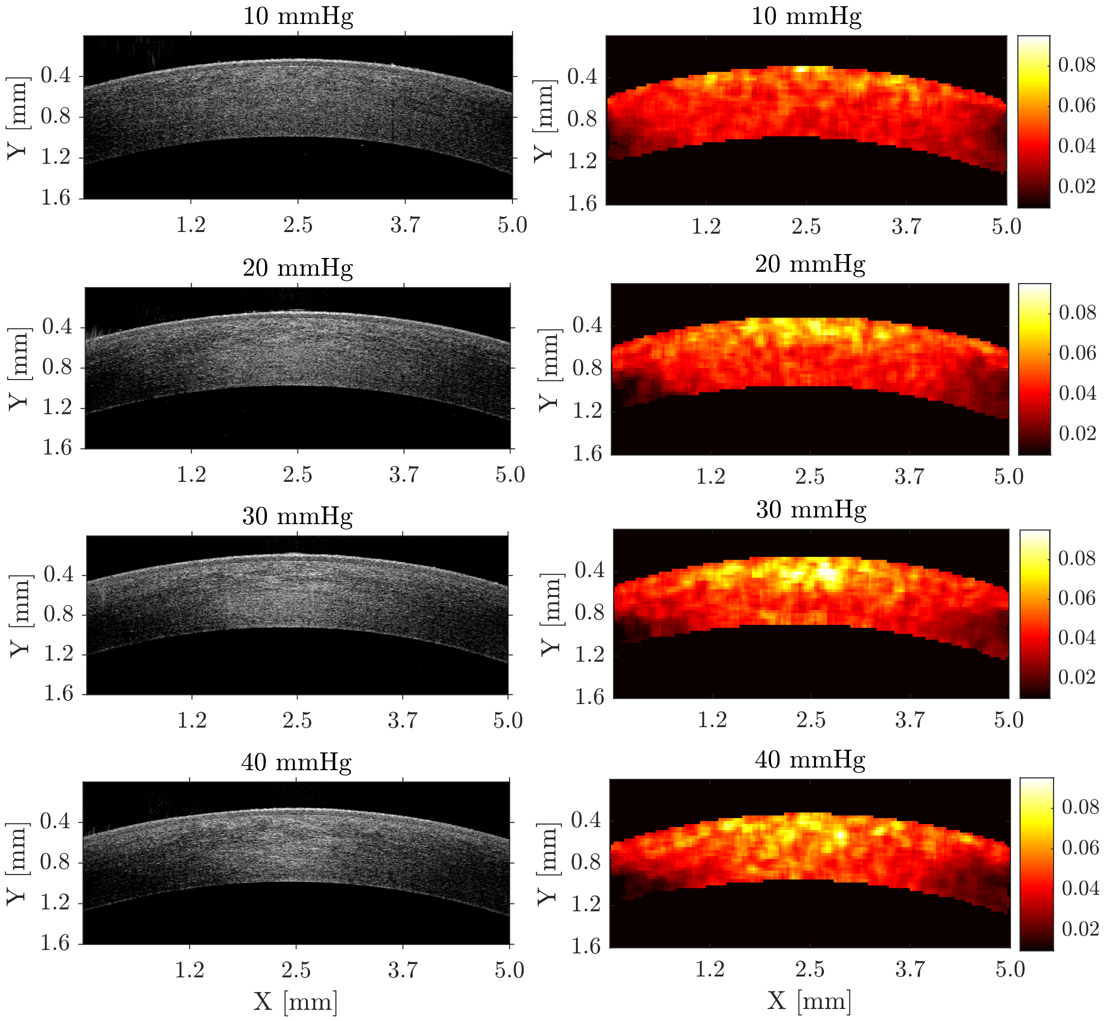

FIGURE 3.11: An example of spatial maps of the gamma distribution scale parameter (a) together with corresponding OCT scans for four out of seven IOP levels in Experiment 1.

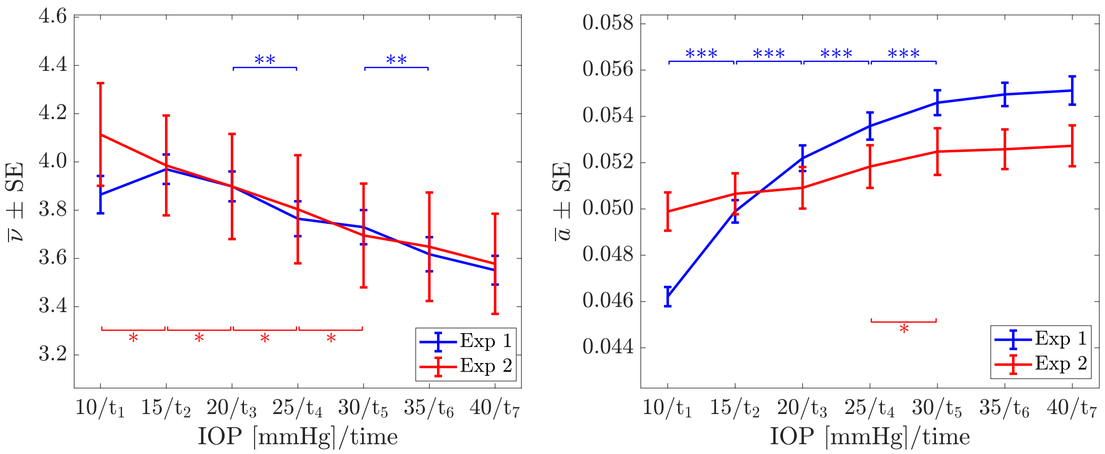

FIGURE 3.12: Mean values (± standard error) of gamma distribution shape (ν) and scale (a) parameters, calculated from the ROI encompassing entire cornea thickness in the spatial maps of parameters, as functions of IOP (Experiment 1) or time (Experiment 2).

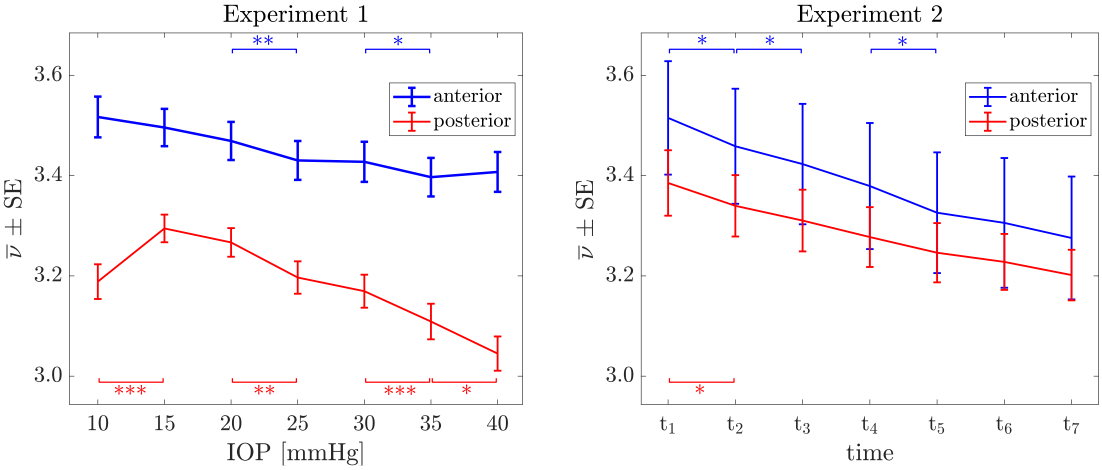

FIGURE 3.13: Mean values (± standard error) of gamma distribution shape parameter ν, calculated separately for the anterior and posterior halves of the cornea in the spatial maps of parameters, as functions of IOP (Experiment 1) or time (Experiment 2).

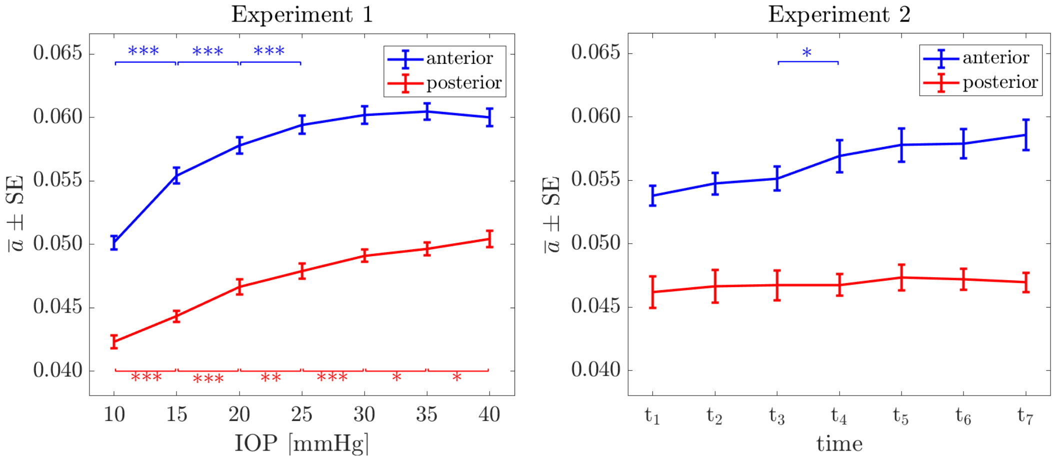

FIGURE 3.14: Mean values (± standard error) of gamma distribution scale parameter a, calculated separately for the anterior and posterior halves of the cornea in the spatial maps of parameters, as functions of IOP (Experiment 1) or time (Experiment 2).

Also, the anterior and posterior halves of ROI were analysed separately to roughly assess the location of changes in parameters values. Figures 3.13 and 3.14 show results for the shape and scale parameter of the gamma distribution, respectively. The plots of the shape parameter values in Experiment 2 are similar for anterior and posterior parts of cornea. In Experiment 1 the shape parameter in the posterior part has lower values and decreases faster comparing to the anterior part. It is also revealed that the statistically significant increase in shape parameter values between 10 and 15 mmHg, observed for entire corneal thickness, occurs only in the posterior cornea. The scale parameter has higher values in the anterior cornea comparing to the posterior half in both experiments. The significant increase of its values is observed in Experiment 1 for the posterior part between all consecutive IOP levels and in the anterior part

TABLE 3.4: The results of rmANOVA for values of statistical distances and CR in the study on porcine eyeballs.

Statistical distance	rmANOVA	
	Experiment 1	Experiment 2
D_{MSE}	$F = 28.37, p < 0.001$	$F = 2.68, p = 0.024$
D_{KS}	$F = 33.69, p < 0.001$	$F = 7.30, p < 0.001$
D_{MMD}	$F = 29.11, p < 0.001$	$F = 3.74, p = 0.004$
CR	$F = 38.54, p < 0.001$	$F = 23.10, p < 0.001$

only from 10 to 25 mmHg. This analysis revealed that the changes in gamma distribution parameters values are more pronounced in the posterior half of the cornea in spatial maps of distributional parameters.

3.2.4 Non-parametric approach

In the non-parametric approach to corneal speckle analysis, rmANOVA was first used to assess the significance of changes in values of statistical distances and CR with IOP in Experiment 1 or time in Experiment 2. This analysis, presented in table 3.4, showed that all statistical distances and CR values change significantly in both experiments.

Figure 3.15 presents mean values of considered distances and CR together with the results of post-hoc analysis. All distances and values of CR show similar increasing trend in Experiment 1 with statistically significant differences between IOP levels from 15 to 35 mmHg. Analysing results from Experiment 2 there are some significant changes in values of distances, but the mean values only slightly increase with time.

3.3 *In-vivo* study on human eyes

3.3.1 Parametric approach

In the analysis of the results obtained in the *in-vivo* study on human corneas, Pearson correlation coefficient was calculated between IOP and parameters of considered distributions estimated for pixel values from selected ROI in OCT scans. The greatest values of correlation coefficient were obtained for the shape parameter of Burr2 distribution for both YOUNG and OLD groups. Taking into account sample size (27 subjects in the YOUNG group and 29 subjects in the OLD group), the values of correlation coefficient should be greater than 0.6 to be considered as statistically significant due to the guidelines described by Bujang and Baharum [127]. None of the correlations satisfy this condition, nevertheless

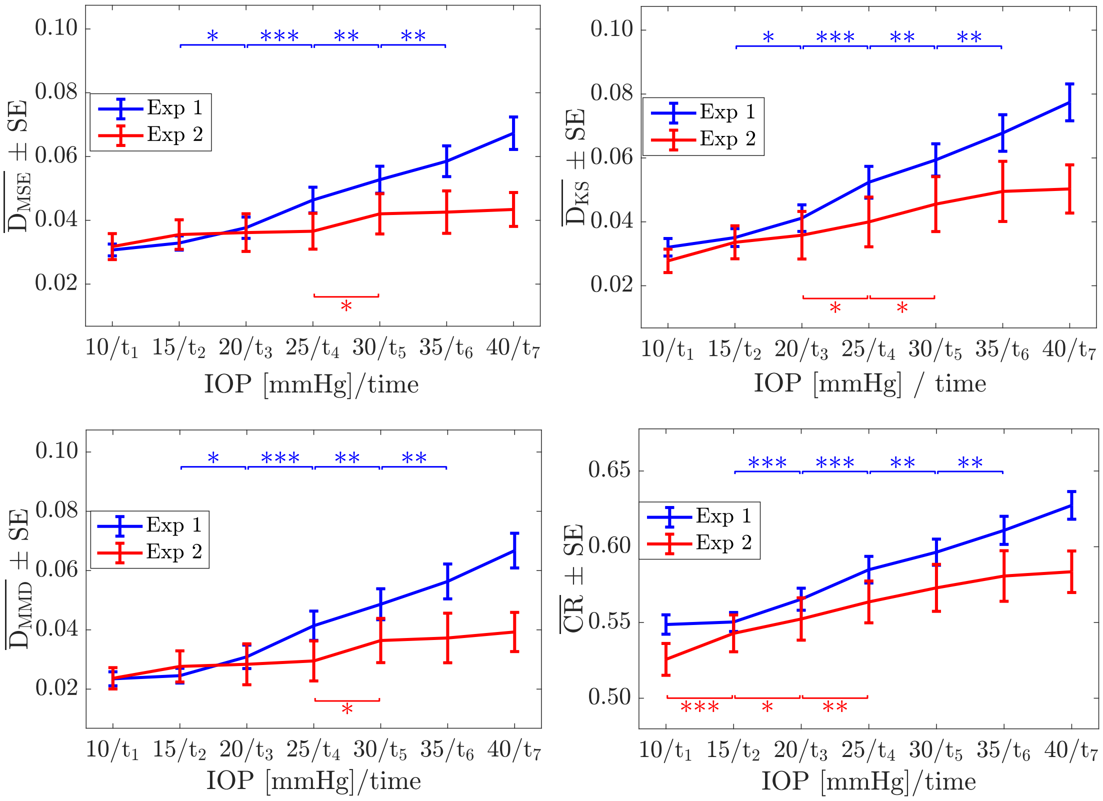

FIGURE 3.15: Mean values (± standard error) of statistical distances and CR as functions of IOP in Experiment 1 or time in Experiment 2 in *ex-vivo* study on porcine eyeballs.

the shape parameter of the Burr2 distribution shows the highest correlation with IOP among analysed set of distributions. In general, correlations are higher for the YOUNG group except for the gamma distribution scale parameter and the shape parameter of Burr2 and generalized gamma distribution.

3.3.2 Non-parametric approach

In the non-parametric approach Pearson correlation coefficient was calculated to assess if changes in statistical distances and CR are associated with IOP. Analysing the results presented in figures 3.16 and 3.17 it can be concluded that the statistical distances as well as CR show higher correlations for the YOUNG group of patients than for the OLD group. The greatest correlation is observed for D_{MSE} distance in the OLD group and for D_{KS} distance in the YOUNG group. In both groups CR shows the weakest correlation with IOP.

TABLE 3.5: The values of Pearson correlation coefficient (R) between IOP and parameters of considered distributions for YOUNG and OLD groups of subjects together with the p-values for testing for zero correlation.

Distribution	Parameter	Pearson correlation coefficient	
		YOUNG	OLD
Burr2	scale	$R = -0.386, p = 0.047$	$R = -0.308, p = 0.105$
	shape	$R = -0.432, p = 0.024$	$R = -0.503, p = 0.005$
Burr3	scale	$R = 0.358, p = 0.066$	$R = 0.215, p = 0.264$
	shape 1	$R = -0.338, p = 0.085$	$R = -0.240, p = 0.210$
	shape 2	$R = -0.358, p = 0.066$	$R = 0.021, p = 0.912$
gamma	scale	$R = 0.166, p = 0.407$	$R = 0.417, p = 0.025$
	shape	$R = -0.354, p = 0.070$	$R = -0.269, p = 0.159$
generalized gamma	scale	$R = 0.085, p = 0.675$	$R = 0.072, p = 0.710$
	shape 1	$R = -0.173, p = 0.390$	$R = -0.067, p = 0.731$
	shape 2	$R = 0.054, p = 0.789$	$R = -0.274, p = 0.151$
K	scale	$R = -0.265, p = 0.181$	$R = -0.013, p = 0.945$
	shape	$R = -0.406, p = 0.036$	$R = -0.227, p = 0.236$
Nakagami	scale	$R = -0.202, p = 0.313$	$R = 0.060, p = 0.757$
	shape	$R = -0.370, p = 0.058$	$R = -0.280, p = 0.141$
Rayleigh	scale	$R = -0.206, p = 0.302$	$R = 0.079, p = 0.684$
Weibull	scale	$R = -0.246, p = 0.216$	$R = 0.023, p = 0.908$
	shape	$R = -0.391, p = 0.044$	$R = -0.278, p = 0.144$

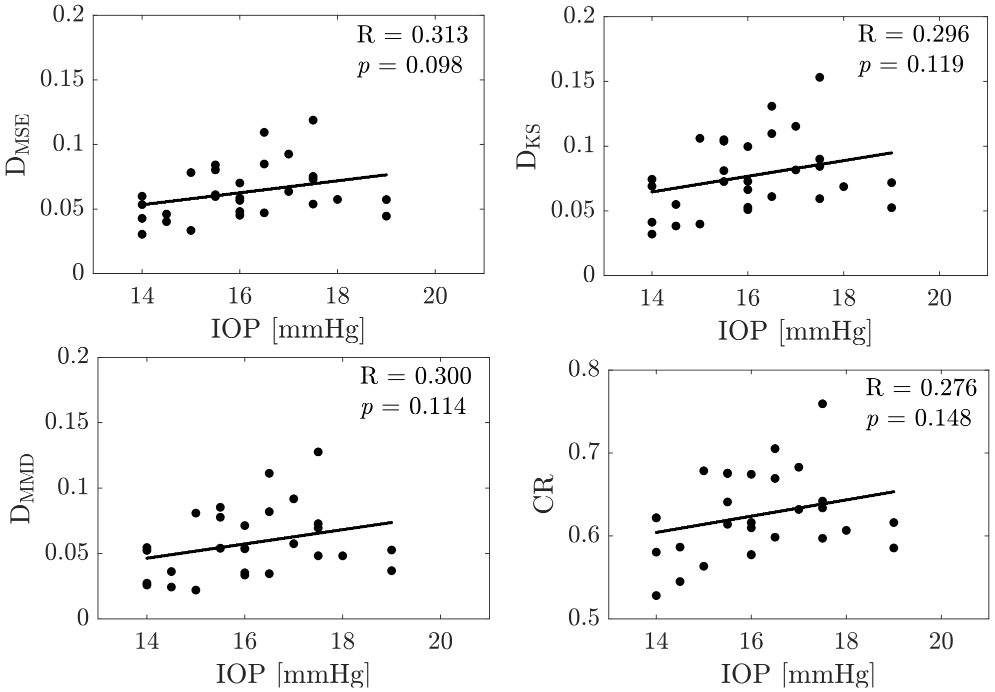

FIGURE 3.16: Values of statistical distances in the non-parametric approach to speckle analysis as functions of IOP for the OLD group. In top right corner of each plot there are values of Pearson correlation coefficient (R) and corresponding p-values. Straight line in the plots represents the linear fit to the experimental data.

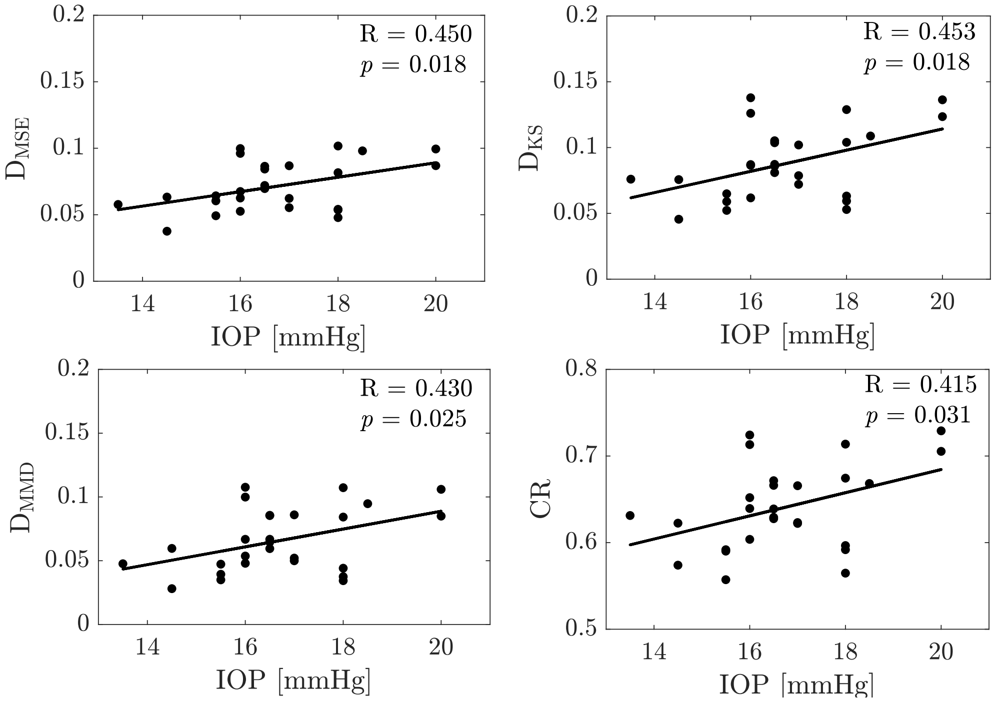

FIGURE 3.17: Statistical distances and CR as functions of IOP for the YOUNG group. In top right corner of each plot there are values of Pearson correlation coefficient (R) and corresponding p-values. Straight line in the plots represents the linear fit to the experimental data.

Chapter 4

Discussion and future directions

4.1 Discussion

Two approaches for corneal OCT speckle analysis were presented in this thesis: a parametric, involving estimation of distributional parameters, and a non-parametric, where the differences between the empirical distribution of normalized amplitude of a speckle field was compared to a benchmark Rayleigh distribution with a constant value of its scale parameter. These approaches were presented on tree different studies, in which OCT scans of phantoms, *ex-vivo* porcine corneas, and *in-vivo* human corneas were utilized.

In the phantom study, for the analysed set of distributions, GoF values were lower and almost constant for high concentrations of blue dye particles while they were increasing with the decrease of concentration. The observed changes and trend in the GoF suggest that the speckle field in OCT images is probably fully developed only for $C_9 - C_6$ concentrations of scattering particles. The more the speckle field departs from being fully developed, the worse is the distributions fitting to pixel values from ROI in OCT scans of phantoms. That is supported by the results obtained from the non-parametric approach, where trends similar to that of GoF were observed for considered statistical distances and CR values. It also suggests that speckle field departs from being fully developed for lower concentrations of blue dye particles, because according to the theory, the Rayleigh distribution is a fundamental distribution of the amplitude of a fully developed speckle field [54], [128].

For phantoms, distributional parameters estimated from the pixel values of OCT scans, usually show similar trends as GoF, with approximately constant values for higher concentrations of scattering particles and some trends for the $C_5 - C_1$ concentrations. According to figures 3.2 and 3.4, the normalization of amplitude is affecting scale parameters while shape parameters remains unchanged. It is important to pay attention to this fact in statistical analysis of speckle field. The results obtained from the phantom study confirm the first hypothesis put in this work that the scatterer density affects OCT speckle statistics.

In case of the three-parameter distributions, a good fitting to experimental data was observed in the study on phantoms as well as on *ex-vivo* porcine eyeballs. However, in the phantom study the distributional parameters showed weak trends with scatterer density (figure 3.3). That arises from correlation of the estimators of distributional parameters resulting in different well-fitted distributional representations obtained for more than one set of parameter estimates. The estimates orthogonality is rare in distributions with three or more parameters because of the high complexity of the differential equations required to construct orthogonal estimators [129]. Overall, despite better fitting of three-parameter distributions to experimental data, their estimators may have worse discriminating power (i.e., may provide worse tissue biomarkers) while compared with distributions with one or two parameters.

In the *ex-vivo* study on porcine eyeballs two experiments were performed to assess if observed changes in corneal OCT speckle statistics are related to changes in IOP (Experiment 1) and to differentiate observed results from the effect of the duration of *ex-vivo* experiment (Experiment 2). From a set of distributions, gamma distribution was selected as the most appropriate to model corneal OCT speckle owing to its theoretical justification for the sum of speckle patterns [52]. Since OCT device has some aperture, the speckle pattern may be assumed to be averaged over some area. Moreover, the gamma distribution showed quite good fitting to empirical distribution of pixel values in OCT images and invariance of its GoF for different levels of IOP (see figure 3.6). Also, gamma distribution is used in the literature for OCT speckle modelling [70], [71].

In this work the gamma distribution was utilized in two different ways. First, its parameters were estimated for pixel values (after inverse-log transformation) from a ROI within the OCT scan. The scale parameter showed statistically significant changes for IOP elevation while in the experiment with constant IOP there was only a slight increase of parameter values with time. That indicates the potential of using scale parameter values as a marker of changes in IOP. The changes in shape parameter were similar for both experiments and the decreasing trend with IOP and time was observed. Kirillin et al. [70] presented similar observations for OCT images of polystyrene microspheres phantoms. Based on simulations and experimental studies he showed the increase of the scale parameter values with increasing concentration of particles, while the values of shape parameter were almost constant or slightly decreasing.

The use of gamma distribution parameters as biomarkers is supported by theoretical calculations presented by Dainty [12], indicating that the shape parameter of gamma distribution is related to the number of speckles within the scanning aperture and the scale parameters is proportional to that number as well but also inversely proportional to the average intensity (or amplitude) of speckle field. Kirillin et al. [70] suggested that the shape parameter of gamma distribution is thought to be related to the scatterer density while the scale parameter is dependent on mean speckle amplitude which is connected with both scatterer concentration and cross-section.

Based on the analysis of the changes in gamma distribution parameters in the *ex-vivo* study using porcine eyeballs, another method for the analysis of OCT images was proposed. In this method distributional parameters are estimated in a small window moving through the image, giving as a result a spatial map of parameter values. Since the changes of values of both shape and scale parameter observed in maps are evident for increasing IOP, as a basic approach a simple quantitative analysis, based on mean parameter value calculation, was proposed. The results were similar to those obtained for parameters estimated from ROI in OCT scans. In both cases, the shape parameter showed similar trends for Experiment 1 and 2, so its values were influenced mostly by the effect of the experiment duration rather than the effect of IOP increase. Conversely, for the scale parameter there was a clear difference between experiments. The increase of parameter values with increasing IOP was observed in Experiment 1 with statistically significant differences between adjacent IOP levels. Such changes in scale parameter values were not observed for Experiment 2, so it could be concluded that they resulted from the effect of IOP increase.

Changes in mean values of gamma distribution parameters with IOP and time were also assessed for anterior and posterior half of stroma separately. Values of both parameters were lower in posterior stroma compared to the anterior part. Moreover, there were more statistically significant differences of both parameters between consecutive IOP levels in posterior stroma in Experiment 1. In Experiment 2 the trends in parameter values were comparable. That result suggests lower sensitivity of anterior stroma to changes in corneal properties induced by IOP. A possible explanation was presented by DelMonte and Kim [87]. Because the organization of collagen bundles is tighter in the anterior stroma, it contributed to tighter cohesive strength in this area and that may be a reason of higher resistance of this part of the cornea to changes in stromal hydration compared to the posterior stroma, which tends to more easily develop folds. The results of the study on porcine eyeballs confirmed the second hypothesis, which claimed that changes in corneal properties caused by the variations in IOP can be detected using speckle statistics in OCT images.

Analysing changes in biometric parameters of porcine eyeballs, statistically significant decrease in CCT is observed at the beginning of both experiments. Similar results were observed in the work of Kazaili et al. [130] who obtained 14% decrease in CCT of porcine corneas subjected to IOP elevation from 0 to 60 mmHg. In the study of Wu et al. [97], a decrease in size of gaps between lamellar structures with increasing IOP was observed for rabbit corneas using non-linear optical microscopy for increasing IOP. That may be one of possible causes of CCT decrease in Experiment 1 presented in this work. Nonetheless, slight but statistically significant decline in CCT occurred also between t_1 and t_2 time points in Experiment 2, where IOP was maintained at the constant level of 15 mmHg. Such small changes in CCT were also showed in the study of Vetter et al. [131] for untreated porcine eyeballs with constant IOP of 20 mmHg maintained for 120 minutes. It is likely that the CCT decrease is not only due to the effect of IOP but also results from eyeball adaptation to experimental conditions.

Another significant differences were observed for AL only in Experiment 2 and did not occur when IOP was increased, although in literature a correlation between AL and IOP can be found [132], [133]. One of possible explanations is that the changes of AL in the study presented in this work may be connected with some processes occurring postmortem, e.g., eyeball hydration loss, and in Experiment 1 they are compensated by IOP elevation.

Significant changes were also observed for AQD and M parameters in Experiment 1. Increase of AQD parameter is thought to be connected with the PBS injection directly to the anterior chamber of the eyeballs. The decrease of the M parameter is linked to the increase of corneal radius of curvature. It occurs only at the beginning of Experiment 1 when IOP is below the physiological value for porcine eyes [134]. For IOP values greater than 20 mmHg and for all time points in Experiment 2, where IOP was kept at the level of 15 mmHg all the time, no significant changes in M parameter were observed. Similarly, in the study of Pierscionek et al. [135] corneal curvature was unchanged for IOP elevation from 15 to 45 mmHg.

The last study presented in this work included OCT images of human corneas in the *in-vivo* study. Subjects were divided into two groups using their age to classify them. In the YOUNG group the age of subjects was less than 30 years and in the OLD group it was greater than 50 years. In the parametric approach, the majority of the correlations between distributional parameters and IOP were greater in the YOUNG group while compared to the OLD group. Also, in the non-parametric approach, correlations between IOP and statistical distances or CR were higher for younger subjects. Moreover, increasing trend of statistical distances and CR values with IOP is in accordance with the results obtained for porcine eyeballs, although the range of IOP in this study was much smaller compared to the study on porcine eyeballs.

It is likely that lower correlations between IOP and estimated parameters or calculated statistical distances in older subjects result from a number of factors affecting the aging eyes. Malik et al. [89] in his study showed the decrease with age in the interfibrillar spacing within human corneas for a fixed hydration, which may be related to changes in the proteoglycan composition of the interfibrillar matrix. He also showed increase in the cross-sectional area in corneal collagen associated with age. Also, Daxer et al. [101] demonstrated an increase in collagen fibril diameter with age. Elsheikh et al. [100] showed the corneal stiffening (increased resistance to deformation) with increasing age and indicated age-related changes in corneal microstructure as well as changes in collagen fibril strength as a possible reasons of that. It is worth noting that ocular changes due to aging should be considered as a nonlinear process, affected not only by environmental factors, but primarily by factors dependent on patient, such as diseases, genetics, lifestyle and others.

Intraocular pressure is affecting entire eyeball inducing changes also in corneal microstructure. Wu and Yeh [97] showed decrease in size of interlamellar gaps in rabbit corneas subjected to IOP elevation. In the study on rat corneas, decreasing collagen fibrils diameter was observed with IOP increase [136]. For the human corneas reorganization of stromal lamellae induced by IOP was revealed [137]. There is also a number of works showing changes not only in corneal microstructure but also in its geometry or biomechanical properties. Kazaili et al. [130] applied line-field OCT to measure mechanical properties of porcine corneas. Linear increase in corneal elastic modulus was observed for IOP from 20 to 60 mmHg. Higher values of elastic modulus are related to stiffening of examined material. Changes in statistics of corneal OCT speckle result from the properties of backscattered light, which is thought to contain information about variations in corneal microstructure. Thus, such methods of speckle analysis may be a valuable tool for indirect evaluation of corneal microstructure. In this work changes in statistical distances in the study on porcine eyeballs show similar trend as for decreasing scatterers concentration in the phantom study. It suggests that increasing IOP causes the reduction of corneal structures which scatter the light. Nevertheless, further studies combining statistical analysis of speckle and corneal imaging in micro- or nanoscale are required to better understand the relations between statistical parameters and corneal microstructure.

Comparing two approaches to speckle analysis presented in this work, the main difference is the computational complexity. In a parametric approach the estimation of parameters is required, usually using the method of maximum likelihood. That involves calculations that are usually more computationally intensive compared to the non-parametric approach, where no distributional parameters are estimated. Nevertheless, the results obtained using these two approaches are comparable. There are statistically significant differences in distributional parameters, statistical distances and CR values observed for changes in IOP or scatterer concentration. These observations lead to conclusion that simpler methods of speckle analysis should be considered before other more complicated approaches. That confirms the third hypothesis of this work that both proposed approaches (non-parametric and parametric) can be successfully utilized for speckle analysis with similar diagnostic power.

4.2 Limitations

The main limitation of the studies presented in this thesis is their relatively small sample sizes. The influence of scatterer density on speckle was presented on 9 phantoms with different concentration of blue dye particles. Although that was only a preliminary study, which aim was to demonstrate that speckle statistics are influenced by the density of scatterers in examined medium, more samples would allow to perform a statistical analysis of obtained results. Also in the study on porcine eyeballs sample size was rather small, especially in Experiment 2. That resulted from limited availability of porcine eyeballs from the abattoir, which, moreover, were often damaged and thus excluded from experiments. In the *in-vivo* study on human corneas, the total number of subjects was 56 and that may appear small. Nevertheless, sample sizes in the study of porcine and human corneas was sufficient to obtain reliable results, perform statistical analysis and draw conclusions about the influence of IOP on speckle in OCT images.

In *ex-vivo* experiments there is a number of factors affecting the tissues which are subjected to non-physiological conditions, i.e., experiment duration, ambient temperature and humidity, moisturizing (frequency, type of utilized solution), processes occurring postmortem. The main problem with *ex-vivo* eyeball is fast loss of hydration, as the eyeball consists of water in 78% [138]. Another problem is corneal swelling caused by the hydrophilic character of proteoglycans in stroma [87]. Only slight changes in CCT were observed in this study suggesting that regular hydrating of the eyeballs prevented excessive corneal swelling. In *ex-vivo* experiments it is impossible to assure the conditions provided *in-vivo*. Nevertheless, such experiments on intact eyeballs are commonly used for mechanical testing of the eyeball properties [139], [140].

The main part of the analysis presented in this work was performed on porcine corneas, so the results cannot be translated directly for human corneas. The use of human corneas in *ex-vivo* studies is difficult due to their limited availability. Thus an important issue was the choice of a human eye model. The study of Subasinghe et al. [141] showed that there are statistically significant differences in collagen fibrillar diameter, interfibrillar distance and interlamellar distance between porcine, rabbit and human corneas, but all five corneal layers were observed for these three species. They concluded that despite porcine and rabbit corneas being not structurally identical to human cornea, they are similar enough to be used as research models.

Another limitation is that in the study on human corneas the true value of IOP was unknown. However, measurements performed by air-puff tonometer provide an estimate of the real value of IOP that can be used for analysis. This limitation did not occur in the study on porcine eyeballs as IOP was controlled and measured directly using the needle inserted into the anterior chamber of the eye connected to a pressure transducer. For obvious reasons such measurement was not possible in the *in-vivo* study, so it should be only taken into consideration in results analysis that IOP values were estimated with some limited accuracy.

4.3 Future directions

There are a lot of possibilities of future development of proposed speckle analysis methods. For higher concentrations of scattering particles in phantoms there are slight variations of parameters or statistical distances, so the speckle field is supposed to be fully developed. Thus, there is a need for development of measures sensitive to changes in speckle field which is fully developed.

Also, the gamma distribution used in this work for speckle modelling could be replaced by any other distribution or new distribution should be calculated with parameters reflecting specific features of scatterers. When analysing maps of parameters, only simple description, based on mean parameter value, was considered. Other measures, taking into account spatial variations of the values of parameters, should be developed. Images from only one OCT device were considered in this study, so it would be beneficial to compare the obtained results with those from similar studies performed using other devices.

4.4 Conclusions

To sum up, corneal OCT speckle reflects changes in corneal properties induced by IOP. The statistics of speckle may be used for indirect evaluation of these changes. That provides a background for the new interesting functionalities of OCT devices.

Appendix A

Averaging of OCT scans

Speckle noise in OCT images causes low image quality and as a result reduced distinguishing power of imaged structures. Due to the assumption that noise in images is randomly distributed, a common method of noise reduction is averaging of B-scans [142]. Some OCT devices provide in their software an image averaging function and even allow to select the number of single B-scans averaged in order to enhance image quality. However, there are also OCT devices that generate only averaged B-scans. For this reason, the impact of such averaging on speckle statistics should be considered.

The theoretical model of averaged corneal OCT speckle will be introduced here assuming that the speckle field in a single non-averaged OCT B-scan is a gamma distributed random variable. Next, the proposed model will be validated on a small data set containing averaged OCT images.

Let Y be a random variable representing speckle field of averaged OCT image and defined as follows

$$Y = \frac{1}{N} \sum_{1}^{N} X_i \,, \tag{A.1}$$

where $X_i \sim \Gamma(\nu, a),\ i = 1, ..., N$ are gamma distributed random variables with a shape parameter ν and a scale parameter a. The same distribution of speckle in all averaged images is assumed because in a short time of their acquisition no changes in corneal properties, influencing speckle statistics, are supposed to occur. The gamma distribution is described by the PDF

$$p_{X_i}(x; a, \nu) = \frac{1}{a^{\nu}\Gamma(\nu)} x^{\nu-1} e^{-x/a}, \quad x > 0\,, \tag{A.2}$$

where $\Gamma(\cdot)$ is the gamma function.

Based on the properties of gamma distribution, the summation of gamma distributed random variables $X_i \sim \Gamma(\nu, a)$ with the same shape and scale parameters results in a random variable, which also comes from the gamma

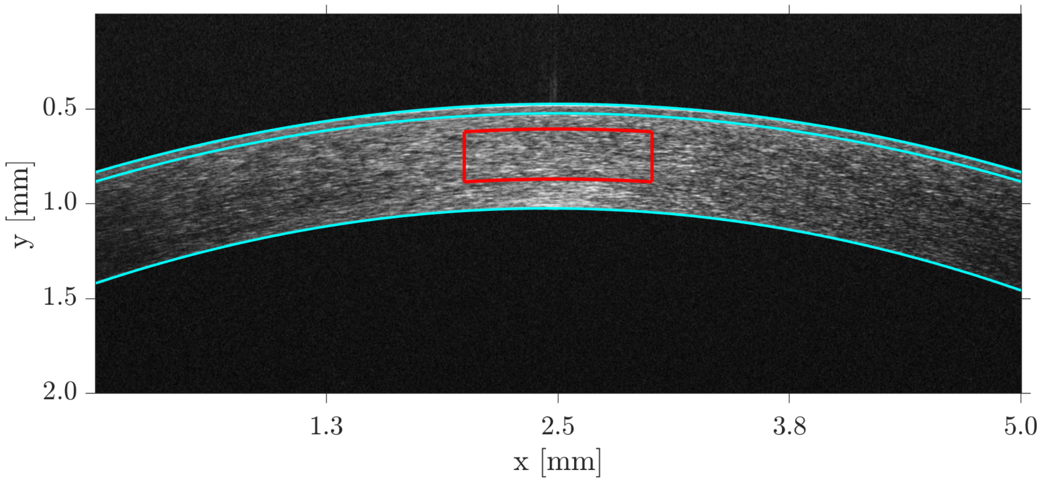

FIGURE A.1: Illustrative OCT image of the cornea, averaged from five single B-scans. Cyan lines indicate epithelium, Bowman's layer and endothelium. The ROI, marked with red lines, contains corneal speckle.

distribution in a form

$$\sum_{i=1}^{N} X_i \sim \Gamma\left(N\nu, a\right) . \tag{A.3}$$

The scaling of gamma distributed random variable $X \sim (\nu, a)$ gives for any $c > 0$

$$cX \sim \Gamma(\nu, ca) . \tag{A.4}$$

Combining properties of gamma distribution from equations A.3 and A.4 and applying them for the considered random variable Y, defined in equation A.1, one obtains

$$Y \sim \Gamma\left(N\nu, \frac{a}{N}\right) . \tag{A.5}$$

The presented theoretical distribution of averaged speckle field is compared with experimental results. OCT images used in this analysis were acquired using OCT Copernicus REVO for 5 healthy subjects, at the age from 25 to 30 years old. The number of B-scans averaged to obtain the final image was set in the device software. Images averaged from 1, 5, 10, 20, 30, 40, 50, and 100 B-scans were collected for each subject and then included in the study. Figure A.1 presents an illustrative image and marked ROI of size 300 × 80 pixels, from which pixel values, after inverse-log transformation, were utilized for the estimation of distributional parameters.

Gamma distribution parameters were estimated for all images of each subject and mean values of parameters for different number of averaged images are presented in figure A.2. The fitting of a linear function using least squares method was performed for the shape parameter and a power function was fitted for the mean values of the scale parameter. It is clear that presented values of

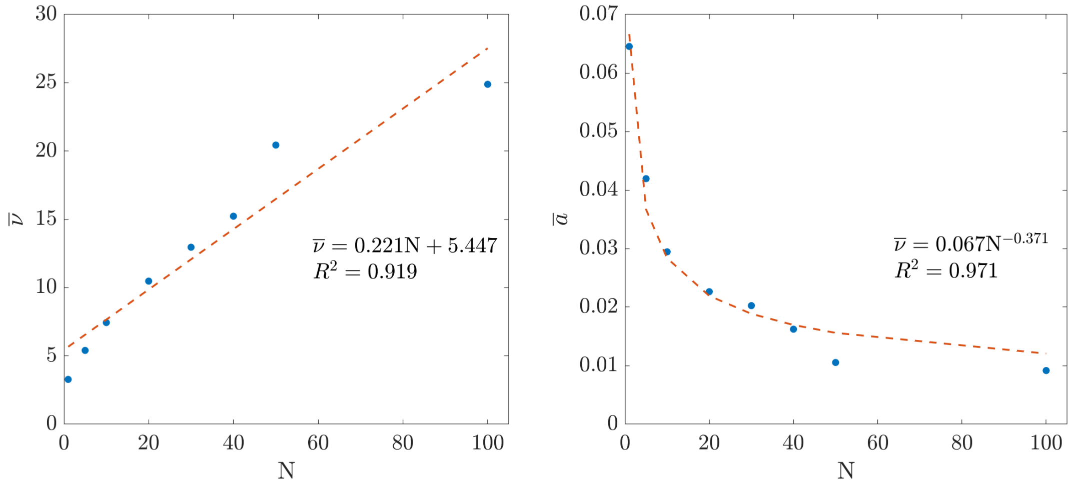

FIGURE A.2: Mean values of gamma distribution shape (ν) and scale (a) parameter, estimated for corneal speckle as functions of a number of averaged images N. Red dashed lines are linear and power functions fitted using the method of least squares for the shape and scale parameter values, respectively. Also, the equations of fitted functions are included in the plots together with the coefficient of determination R^2.

parameters do not satisfy the theoretical relation between gamma distribution parameters and the number of averaged images, showed in equation A.5.

Gamma distribution parameters were also estimated from ROI containing only background noise, presented in figure A.3, and their analysis, analogous to that presented above, was performed. Mean values of the shape and scale parameter, together with their fitting with linear and power function, respectively, are presented in figure A.4. In this case estimated values of parameters satisfy the relations from equation A.5. The shape parameter value of non-averaged image is 1.76, so it is close to the slope of fitted function, equal to 1.80. This indicates that next values of parameter are approximately equal to the number of averaged images N multiplied by the initial parameter value. Similarly, analyzing the equation of power function fitted to the plot of scale parameter values, the number of averaged images with a power of -1 is multiplied by 0.013, corresponding to the scale parameter value estimated for the non-averaged B-scan. That also satisfies the relation from equation A.5.

To sum up, the statistics of corneal speckle in averaged OCT images do not satisfy assumed theoretical model for averaging gamma random variables. However, the proposed model surprisingly is appropriate for background noise in OCT images. It suggests that gamma distributed background noise should be taken into consideration in calculations of statistics from OCT images.

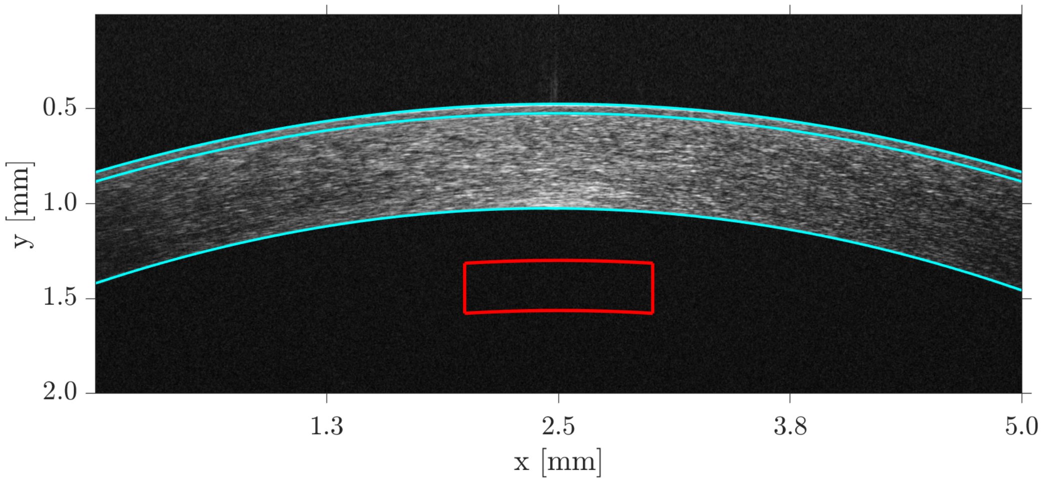

FIGURE A.3: Illustrative OCT image of the cornea, averaged from five single B-scans. Cyan lines indicate epithelium, Bowman's layer and endothelium. The ROI, marked with red lines, contains background noise.

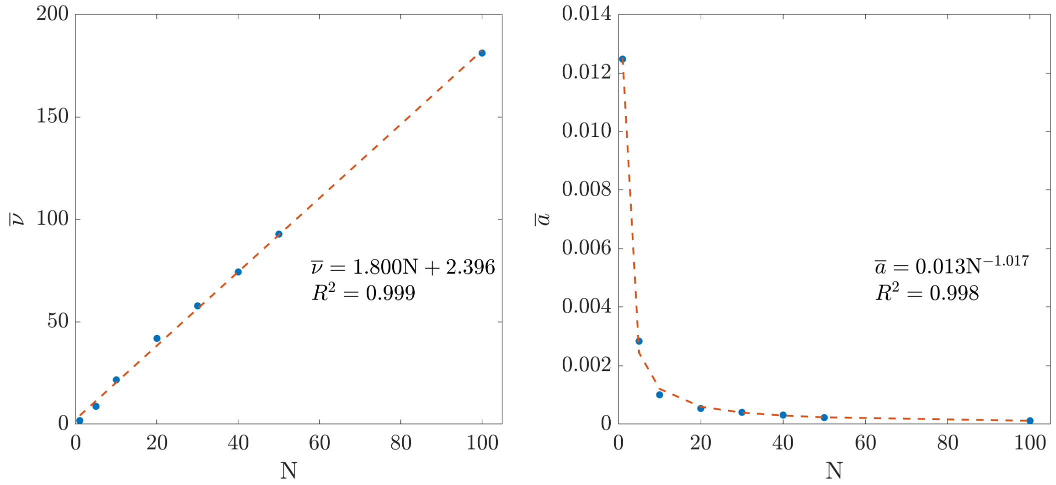

FIGURE A.4: Mean values of gamma distribution shape (ν) and scale (a) parameter, estimated for background noise as functions of a number of averaged images N. Red dashed lines are linear and power functions fitted using the method of least squares for the shape and scale parameter values, respectively. Also, the equations of fitted functions are included in the plots together with the coefficient of determination R^2.

Appendix B

Product distribution for OCT speckle modelling

An attempt to calculate an exact probability distribution of pixel values in OCT images was made in this work. Calculations leading to assumed product distribution and estimators of its parameters will be presented here.

A few assumptions about speckle statistics had to be made first. Taking into account the results from Appendix A, background noise is treated as a gamma distributed random variable. Based on speckle theory described by Goodman [52], OCT speckle, arising from light scattering on sample structures, are averaged by scanning aperture giving the sum of speckle patterns which is treated as another gamma distributed variable. The noise in the form of grainy structures, observed on the cornea in OCT scans is considered as the combination of multiplicative background noise and speckle. This concept is presented schematically in figure B.1.

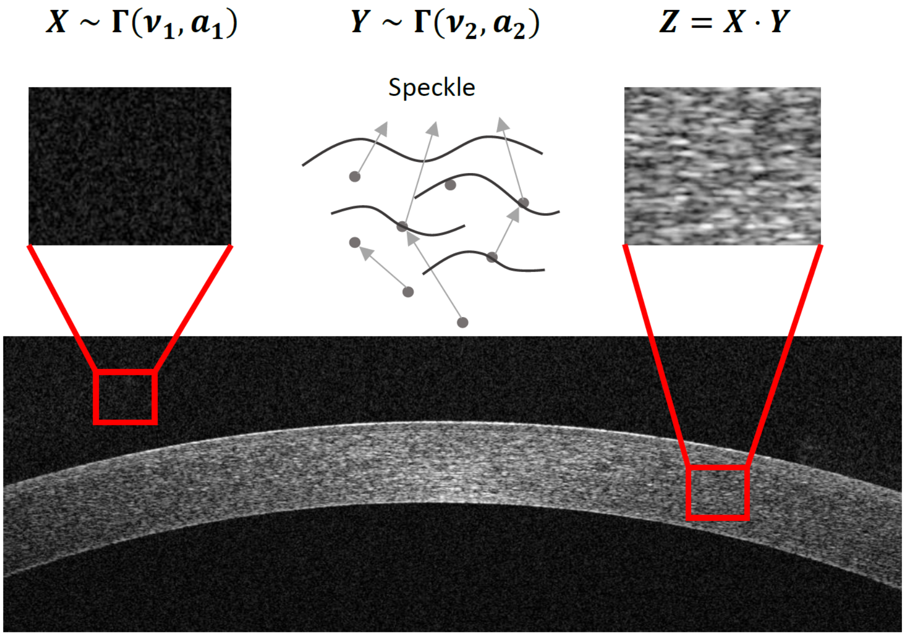

FIGURE B.1: Schematic representation of the idea of product distribution for modelling pixel values in OCT images.

Background noise is denoted as a random variable X from the gamma distribution $\Gamma(\nu_1, a_1)$ with a shape parameter ν_1 and a scale parameter a_1. Speckle are treated as a random variable Y from the gamma distribution $\Gamma(\nu_2, a_2)$ with a shape parameter ν_2 and a scale parameter a_2. Corresponding PDFs are presented below

$$X \sim \Gamma(\nu_1, a_1) \qquad p_X(x) = \frac{1}{\Gamma(\nu_1) a_1^{\nu_1}} x^{\nu_1 - 1} e^{-\frac{x}{a_1}}, \quad x \in (0, \infty), \tag{B.1}$$

$$Y \sim \Gamma(\nu_2, a_2) \qquad p_Y(y) = \frac{1}{\Gamma(\nu_2) a_2^{\nu_2}} y^{\nu_2 - 1} e^{-\frac{y}{a_2}}, \quad y \in (0, \infty) \tag{B.2}$$

where $\Gamma(\cdot)$ is the gamma function. Both parameters of gamma distribution should be positive, so following criteria are defined

$$\nu_1 > 0, \quad a_1 > 0, \quad \nu_2 > 0, \quad a_2 > 0. \tag{B.3}$$

To calculate a product distribution, a random variable Z is defined as

$$Z = X \cdot Y. \tag{B.4}$$

The PDF for the product distribution is described by the equation

$$p_Z(z) = \int_{-\infty}^{\infty} p_X(x) p_Y\left(\frac{z}{x}\right) \frac{1}{|x|} dx. \tag{B.5}$$

Using PDFs B.1 and B.2 in equation B.5 one obtains

$$\begin{aligned} p_Z(z) &= \int_0^{\infty} \frac{1}{\Gamma(\nu_1) a_1^{\nu_1}} x^{\nu_1 - 1} e^{-\frac{x}{a_1}} \cdot \frac{1}{\Gamma(\nu_2) a_2^{\nu_2}} \left(\frac{z}{x}\right)^{\nu_2 - 1} e^{-\frac{z}{x a_2}} \cdot \frac{1}{x} dx = \\ &= \frac{1}{\Gamma(\nu_1)\Gamma(\nu_2)} \cdot \frac{1}{a_1^{\nu_1} a_2^{\nu_2}} \cdot z^{\nu_2 - 1} \int_0^{\infty} x^{\nu_1 - \nu_2 - 1} \cdot e^{-\frac{x}{a_1} - \frac{z}{x a_2}} dx. \end{aligned} \tag{B.6}$$

Now the integral from the equation B.6 need to be resolved. First, the new variables $\nu = \nu_2 - \nu_1$ and $w = 2\sqrt{\frac{z}{a_1 a_2}}$ are defined giving

$$\int_0^{\infty} x^{-\nu - 1} \cdot e^{-\frac{x}{a_1} - \frac{w^2 a_1}{4x}} dx. \tag{B.7}$$

For solving such integral, the substitution $t = \frac{x}{a_1}$ is applied which results in

$$a_1^{-\nu} \int_0^{\infty} t^{-(\nu+1)} \cdot e^{-t-\frac{w^2}{4t}} dt\,. \tag{B.8}$$

From the theory of Bessel functions it is known that

$$\int_0^{\infty} e^{-t-\frac{w^2}{4t}} \cdot t^{-(\nu+1)} dt = 2\left(\frac{w}{2}\right)^{-\nu} K_\nu(w)\,, \tag{B.9}$$

where $K_\nu(\cdot)$ is the modified Bessel function of the second kind of order ν [143]. Using equation B.9, the integral B.8 can be resolved, which gives

$$a_1^{-\nu} \cdot 2\left(\frac{w}{2}\right)^{-\nu} K_\nu(w)\,. \tag{B.10}$$

As a result the PDF from equation B.6 is in the form

$$\begin{aligned} p_Z(z) &= \frac{1}{\Gamma(\nu_1)\Gamma(\nu_2)} \cdot \frac{1}{a_1^{\nu_1} a_2^{\nu_2}} \cdot z^{\nu_2-1} \cdot a_1^{-\nu} \cdot 2\left(\frac{w}{2}\right)^{-\nu} K_\nu(w) = \\ &= \frac{2}{\Gamma(\nu_1)\Gamma(\nu_2)} \cdot \frac{1}{a_1^{\nu_1} a_2^{\nu_2}} \cdot a_1^{\nu_1-\nu_2} \cdot z^{\nu_2-1} \cdot \left(\frac{z}{a_1 a_2}\right)^{\frac{\nu_1-\nu_2}{2}} K_{\nu_2-\nu_1}\left(2\sqrt{\frac{z}{a_1 a_2}}\right) = \\ &= \frac{2}{z \cdot \Gamma(\nu_1)\Gamma(\nu_2)} \cdot \left(\frac{z}{a_1 a_2}\right)^{\frac{\nu_1+\nu_2}{2}} \cdot K_{\nu_2-\nu_1}\left(2\sqrt{\frac{z}{a_1 a_2}}\right). \end{aligned} \tag{B.11}$$

Finally, the PDF of considered product distribution is given by

$$\boxed{p_Z(z) = \frac{2}{z \cdot \Gamma(\nu_1)\Gamma(\nu_2)} \cdot \left(\frac{z}{a_1 a_2}\right)^{\frac{\nu_1+\nu_2}{2}} \cdot K_{\nu_2-\nu_1}\left(2\sqrt{\frac{z}{a_1 a_2}}\right),\ z \in (0, \infty).} \tag{B.12}$$

Next, moments of the distribution are calculated using the general formula for the k-th moment

$$\mu_k = \int_{-\infty}^{\infty} x^k p(x) dx\,, \tag{B.13}$$

where $p(x)$ denotes PDF of distribution.

Using above formula, the first moment of considered product distribution can be obtained as follows

$$\begin{aligned}\mu_1 &= \int_0^\infty z \cdot \frac{2}{z\Gamma(\nu_1)\Gamma(\nu_2)} \cdot \left(\frac{z}{a_1a_2}\right)^{\frac{\nu_1+\nu_2}{2}} \cdot K_{\nu_2-\nu_1}\left(2\sqrt{\frac{z}{a_1a_2}}\right)dz = \\ &= \frac{2^{-(\nu_1+\nu_2)}(a_1a_2)^{\frac{1}{2}}}{\Gamma(\nu_1)\Gamma(\nu_2)} \int_0^\infty \left(2\sqrt{\frac{z}{a_1a_2}}\right)^{\nu_1+\nu_2+1} \cdot K_{\nu_2-\nu_1}\left(2\sqrt{\frac{z}{a_1a_2}}\right) \cdot z^{-\frac{1}{2}}dz\,.\end{aligned} \tag{B.14}$$

Applying $u = 2\sqrt{\frac{z}{a_1a_2}}$ to solve the integral by substitution one obtains

$$\mu_1 = \frac{2^{-(\nu_1+\nu_2)}a_1a_2}{\Gamma(\nu_1)\Gamma(\nu_2)} \int_0^\infty u^{\nu_1+\nu_2+1} \cdot K_{\nu_2-\nu_1}(u)du\,. \tag{B.15}$$

To resolve the integral from equation B.15, following relationship, obtained by applying Mellin transform to the modified Bessel function of the second kind [144], is involved

$$\int_0^\infty t^{s-1}K_\nu(t)dt = 2^{s-2} \cdot \Gamma\left(\frac{s}{2}+\frac{\nu}{2}\right)\Gamma\left(\frac{s}{2}-\frac{\nu}{2}\right). \tag{B.16}$$

Using above relation for the integral from equation B.15, after appropriate transformations, the formula for μ_1 is given by

$$\mu_1 = a_1a_2\frac{\Gamma(\nu_1+1)\Gamma(\nu_2+1)}{\Gamma(\nu_1)\Gamma(\nu_2)}\,. \tag{B.17}$$

The moments of 2nd and 3rd order were calculated in the same manner. Finally, the general formula for the kth moment of considered product distribution was obtained in the form

$$\boxed{\mu_k = (a_1a_2)^k \cdot \frac{\Gamma(\nu_1+k)\Gamma(\nu_2+k)}{\Gamma(\nu_1)\Gamma(\nu_2)}} \tag{B.18}$$

PARAMETER ESTIMATION

The estimation of distributional parameters is presented here using the following first three moments, calculated based on the formula B.18

$$\mu_1 = a_1 \cdot a_2 \cdot \nu_1 \cdot \nu_2 \tag{B.19}$$

$$\mu_2 = (a_1a_2)^2\nu_1(\nu_1+1)\nu_2(\nu_2+1) \tag{B.20}$$

$$\mu_3 = (a_1 a_2)^3 \nu_1(\nu_1+1)(\nu_1+2)\nu_2(\nu_2+1)(\nu_2+2)\,. \tag{B.21}$$

From equation B.19 following relationship is obtained

$$a_1 a_2 = \frac{\mu_1}{\nu_1 \nu_2}\,. \tag{B.22}$$

The ratios of moments μ_2/μ_1 and μ_3/μ_2 are given by

$$\frac{\mu_2}{\mu_1} = a_1 a_2(\nu_1+1)(\nu_2+1) \tag{B.23}$$

$$\frac{\mu_3}{\mu_2} = a_1 a_2(\nu_1+2)(\nu_2+2)\,. \tag{B.24}$$

Combining then equations B.22 and B.23 results in the formula linking two shape parameters as follows

$$\nu_1 = \frac{\nu_2+1}{\frac{\mu_2}{\mu_1^2}\nu_2 - \nu_2 - 1}\,. \tag{B.25}$$

Similarly, combining equations B.22 and B.24 gives another formula for ν_1 as follows

$$\nu_1 = \frac{2\nu_2+4}{\frac{\mu_3}{\mu_2\mu_1}\nu_2 - \nu_2 - 2} \tag{B.26}$$

Comparing equations B.25 and B.26 results in

$$\nu_2^2\left[2\frac{\mu_2}{\mu_1^2} - \frac{\mu_3}{\mu_2\mu_1} - 1\right] + \nu_2\left[4\frac{\mu_2}{\mu_1^2} - \frac{\mu_3}{\mu_2\mu_1} - 3\right] - 2 = 0\,, \tag{B.27}$$

which is a quadratic equation in the form

$$A\nu_2^2 + B\nu_2 + C = 0\,, \tag{B.28}$$

where

$$A = 2\frac{\mu_2}{\mu_1^2} - \frac{\mu_3}{\mu_2\mu_1} - 1 \tag{B.29}$$

$$B = 4\frac{\mu_2}{\mu_1^2} - \frac{\mu_3}{\mu_2\mu_1} - 3 \tag{B.30}$$

$$C = -2\,. \tag{B.31}$$

Then the roots are given by

$$\nu_2 = \frac{-B \pm \sqrt{B^2 - 4AC}}{2A}\,. \tag{B.32}$$

Note that equation B.27 is also valid for the ν_1 instead of ν_2, so ν_1 can be calculated as follows

$$\nu_1 = \frac{-B \pm \sqrt{B^2 - 4AC}}{2A} \tag{B.33}$$

with A, B and C described by equations B.29, B.30 and B.31, respectively.

The product of scale parameters may be obtained combining equations B.32 and B.33 with B.22, which results in

$$a_1 a_2 = \mu_1 \frac{A}{C} \, . \tag{B.34}$$

Combining equation B.34 with other formulas does not give a solution for a_1 and a_2 separately, because the multiplication $a_1 a_2$ is always present and these two scale parameters are inseparable. Because of that a parameter a is defined as follows

$$a = a_1 a_2 = \mu_1 \frac{A}{C} \tag{B.35}$$

and hereinafter referred as a scale parameter.

An attempt to calculate MLE estimators of considered product distribution was made. As a result convoluted functions for ν_1 and ν_2 were obtained, so shape parameters could not be uniquely estimated.

MODEL VALIDATION

Simulations were performed in MATLAB to validate proposed parameter estimation method. Two random samples were generated: first from the gamma distribution $\Gamma(\nu_1, a_1)$, where $\nu_1 = 1.5$ and $a = 0.01$ and the second from the distribution $\Gamma(\nu_2, a_2)$ with $\nu_1 = 3.5$ and $a = 0.5$. The values of parameters were selected to approximately correspond to parameters of gamma distribution estimated for pixel values from cornea and background in OCT image. The size of generated samples was from 10^3 to 10^6. Next, for the product of generated random samples, the estimators of parameters were calculated using formulas from equations B.32, B.33 and B.34. Figures B.2 and B.3 present mean values of parameters estimated in simulations together with the standard deviation. It is shown that the estimators asymptotically achieve set values of parameters and also standard deviation decreases with sample size, suggesting that proposed estimators are unbiased and consistent.

Proposed distribution was verified also experimentally using 5 non-averaged single OCT B-scans from the data set described in Appendix A. Pixel values from the ROI of size 300 × 80 pixels, encompassing corneal speckle and presented in figure A.1 in Appendix A, were used for the estimation of parameters of considered product distribution. To verify if proposed distribution could

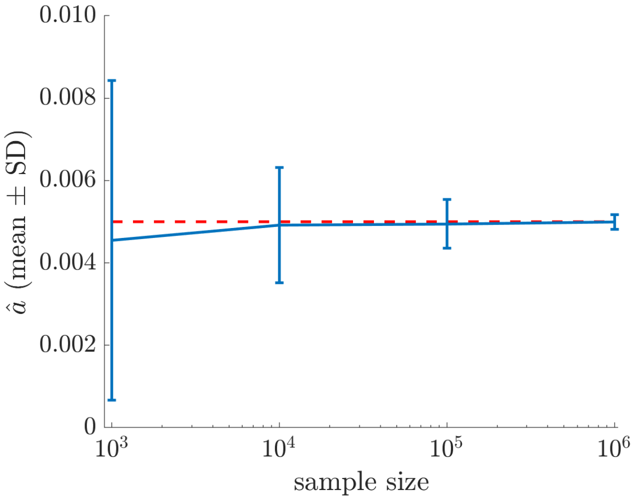

FIGURE B.2: Mean values of estimators of the scale parameter of considered product distribution with error bars denoting standard deviation for different sample sizes. Red dashed line indicates a set value of parameter used for generating a random sample.

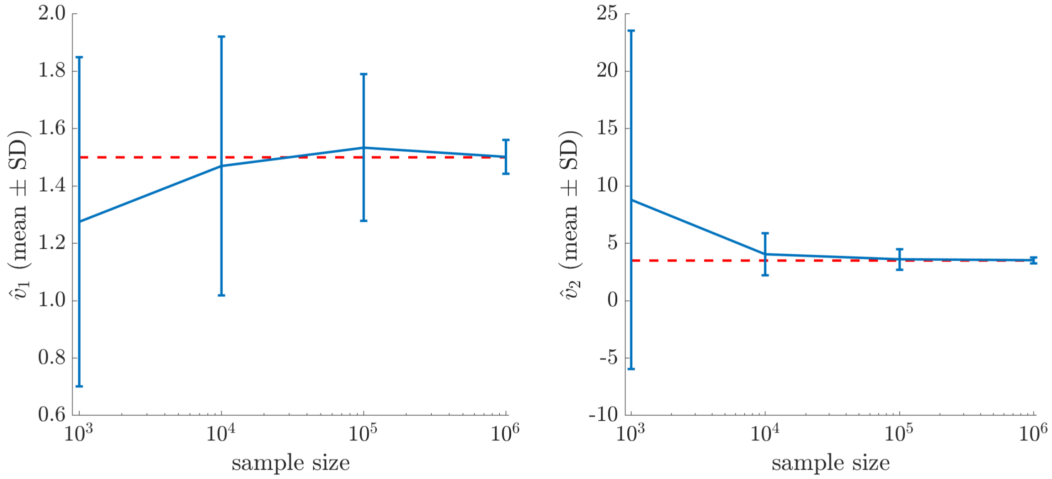

FIGURE B.3: Mean values of estimators of two shape parameters of considered product distribution with error bars denoting standard deviation for different sample sizes. Red dashed lines indicate set values of parameters used for generating a random sample.

be potentially a statistical model for pixel values in OCT images of cornea, parameters of gamma distribution were also estimated for the pixel values from the ROI of the same size containing background noise, presented in figure A.3 in Appendix A. Table B.1 shows values of estimated parameters of considered product distribution and the values of gamma distribution parameters estimated for the background noise. It is clear that the values of ν_2 parameter are comparable to the shape parameter of gamma distribution of background noise, which suggests that one component of the estimated product distribution corresponds to background noise. Two scale parameters are inseparable, its parts related to speckle and background are impossible to

TABLE B.1: Values of product distribution parameters estimated for pixel values from the cornea and gamma distribution parameters for background in OCT images for 5 subjects involved in the study.

Subject	Cornea			Background	
	a	ν_1	ν_2	a	ν
1	0.0013	-10.066	1.586	0.0125	1.724
2	0.0014	-10.052	1.655	0.0126	1.789
3	0.0015	-9.553	1.581	0.0128	1.719
4	0.0013	-10.159	1.648	0.0125	1.777
5	0.0013	-9.854	1.621	0.0121	1.768

be obtained separately, so it cannot be verified if the value of scale parameter estimated for background noise is included in parameters of product distribution. The ν_1 parameter has negative values, which suggests that the estimation of this parameter for pixel values from cornea is not correct referring to criteria defined in equation B.3.

The fact that one of the shape parameters of proposed product distribution is roughly equal to the shape parameter of the distribution of background noise, confirms that the proposed model potentially could be appropriate for pixel values in OCT images of cornea. On the other hand, the negative values of the estimator of ν_2 parameter and inability to obtain values of a_1 and a_2 parameters separately are a major problem of the proposed model. Moreover, the number of distributional parameters that need to be estimated causes that samples of greater size, compared to one- or two-parameter models, are required for the parameter estimation. That makes the considered product distribution impractical to speckle modelling. To conclude, in speckle modelling the use of distributions with one or two parameters rather than those more complicated is beneficial, even though their fitting for experimental data is worse.

Bibliography

[1] A. G. Podoleanu, “Optical coherence tomography,” *Journal of Microscopy*, vol. 247, pp. 209–219, 2012.

[2] A. F. Fercher, K. Mengedoht, and W. Werner, “Eye-length measurement by interferometry with partially coherent light,” *Optics Letters*, vol. 13, pp. 186–188, 1988.

[3] D. Huang, E. A. Swanson, C. P. Lin, *et al.*, “Optical coherence tomography,” *Science*, vol. 254, pp. 1178–1181, 1991.

[4] W. Drexler and J. G. Fujimoto, *Optical coherence tomography: technology and applications*. Springer, 2015.

[5] J. F. Bille, *High resolution imaging in microscopy and ophthalmology: new frontiers in biomedical optics*. Springer, 2019.

[6] A. F. Fercher, C. K. Hitzenberger, G. Kamp, and S. Y. El-Zaiat, “Measurement of intraocular distances by backscattering spectral interferometry,” *Optics Communications*, vol. 117, pp. 43–48, 1995.

[7] A. P. Lange, R. Sadjadi, J. Saeedi, J. Lindley, F. Costello, and A. L. Traboulsee, “Time-domain and spectral-domain optical coherence tomography of retinal nerve fiber layer in MS patients and healthy controls,” *Journal of Ophthalmology*, vol. 2012, 2012.

[8] J. F. De Boer, B. Cense, B. H. Park, M. C. Pierce, G. J. Tearney, and B. E. Bouma, “Improved signal-to-noise ratio in spectral-domain compared with time-domain optical coherence tomography,” *Optics Letters*, vol. 28, pp. 2067–2069, 2003.

[9] R. Forte, G. L. Cennamo, M. L. Finelli, and G. De Crecchio, “Comparison of time domain Stratus OCT and spectral domain SLO/OCT for assessment of macular thickness and volume,” *Eye*, vol. 23, pp. 2071–2078, 2009.

[10] R. Leitgeb, C. K. Hitzenberger, and A. F. Fercher, “Performance of fourier domain vs. time domain optical coherence tomography,” *Optics Express*, vol. 11, pp. 889–894, 2003.

[11] M. S. Hepburn, K. Y. Foo, A. Curatolo, P. R. T. Munro, and B. F. Kennedy, "Speckle in optical coherence tomography," in *Optical coherence elastography: imaging tissue mechanics on the micro-scale*, B. F. Kennedy, Ed., AIP Publishing, 2021.

[12] J. C. Dainty, "The statistics of speckle patterns," in ser. Progress in Optics, E. Wolf, Ed., vol. 14, Elsevier, 1976, pp. 1–46.

[13] D. C. Adler, T. H. Ko, and J. G. Fujimoto, "Speckle reduction in optical coherence tomography images by use of a spatially adaptive wavelet filter," *Optics Letters*, vol. 29, pp. 2878–2880, 2004.

[14] S. Adabi, S. Conforto, A. Clayton, A. G. Podoleanu, A. Hojjat, and M. R. N. Avanaki, "An intelligent speckle reduction algorithm for optical coherence tomography images," in *2016 4th International Conference on Photonics, Optics and Laser Technology*, IEEE, 2016, pp. 1–6.

[15] M. Bashkansky and J. Reintjes, "Statistics and reduction of speckle in optical coherence tomography," *Optics Letters*, vol. 25, pp. 545–547, 2000.

[16] J. Kim, D. T. Miller, E. K. Kim, S. Oh, J. H. Oh, and T. E. Milner, "Optical coherence tomography speckle reduction by a partially spatially coherent source," *Journal of Biomedical Optics*, vol. 10, p. 064 034, 2005.

[17] A. Ozcan, A. Bilenca, A. E. Desjardins, B. E. Bouma, and G. J. Tearney, "Speckle reduction in optical coherence tomography images using digital filtering," *Journal of the Optical Society of America A*, vol. 24, pp. 1901–1910, 2007.

[18] J. M. Schmitt, S. H. Xiang, and K. M. Yung, "Speckle in optical coherence tomography," *Journal of Biomedical Optics*, vol. 4, pp. 95–105, 1999.

[19] T. R. Hillman, S. G. Adie, V. Seemann, J. J. Armstrong, S. L. Jacques, and D. D. Sampson, "Correlation of static speckle with sample properties in optical coherence tomography," *Optics Letters*, vol. 31, pp. 190–192, 2006.

[20] G. J. Tearney, M. E. Brezinski, B. E. Bouma, *et al.*, "*In vivo* endoscopic optical biopsy with optical coherence tomography," *Science*, vol. 276, pp. 2037–2039, 1997.

[21] A. F. Fercher, W. Drexler, C. K. Hitzenberger, and T. Lasser, "Optical coherence tomography — principles and applications," *Reports on Progress in Physics*, vol. 66, pp. 239–303, 2003.

[22] M. R. Hee, J. A. Izatt, E. A. Swanson, *et al.*, "Optical coherence tomography of the human retina," *Archives of Ophthalmology*, vol. 113, pp. 325–332, 1995.

[23] I. Grulkowski, J. J. Liu, B. Potsaid, *et al.*, "Retinal, anterior segment and full eye imaging using ultrahigh speed swept source OCT with vertical-cavity surface emitting lasers," *Biomedical Optics Express*, vol. 3, pp. 2733–2751, 2012.

[24] V. Manjunath, J. Goren, J. G. Fujimoto, and J. S. Duker, "Analysis of choroidal thickness in age-related macular degeneration using spectral domain optical coherence tomography," *American Journal of Ophthalmology*, vol. 152, pp. 663–668, 2011.

[25] J. S. Schuman, M. R. Hee, C. A. Puliafito, *et al.*, "Quantification of nerve fiber layer thickness in normal and glaucomatous eyes using optical coherence tomography: a pilot study," *Archives of Ophthalmology*, vol. 113, pp. 586–596, 1995.

[26] B. Haouchine, P. Massin, R. Tadayoni, A. Erginay, and A. Gaudric, "Diagnosis of macular pseudoholes and lamellar macular holes by optical coherence tomography," *American Journal of Ophthalmology*, vol. 138, pp. 732–739, 2004.

[27] D. R. Iskander, M. A. Kostyszak, D. A. Jesus, M. E. Danielewska, M. Majewska, and P. Krzyzanowska-Berkowska, "Assessing corneal speckle in optical coherence tomography: a new look at glaucomatous eyes," *Optometry and Vision Science*, vol. 97, pp. 62–67, 2020.

[28] C. K. Leung, H. Li, R. N. Weinreb, *et al.*, "Anterior chamber angle measurement with anterior segment optical coherence tomography: a comparison between slit lamp OCT and Visante OCT," *Investigative Ophthalmology & Visual Science*, vol. 49, pp. 3469–3474, 2008.

[29] N. D. Gladkova, G. A. Petrova, N. K. Nikulin, *et al.*, "*In vivo* optical coherence tomography imaging of human skin: norm and pathology," *Skin Research and Technology*, vol. 6, pp. 6–16, 2000.

[30] A. Pagnoni, A. Knuettel, P. Welker, *et al.*, "Optical coherence tomography in dermatology," *Skin Research and Technology*, vol. 5, pp. 83–87, 1999.

[31] S. Z. Aydin, Z. Ash, F. Del Galdo, *et al.*, "Optical coherence tomography: a new tool to assess nail disease in psoriasis?" *Dermatology*, vol. 222, pp. 311–313, 2011.

[32] D. Capodanno, F. Prati, T. Pawlowsky, *et al.*, "Comparison of optical coherence tomography and intravascular ultrasound for the assessment of in-stent tissue coverage after stent implantation," *Eurointervention: Journal of Europcr in Collaboration with the Working Group on Interventional Cardiology of the European Society of Cardiology*, vol. 5, pp. 538–543, 2009.

[33] X. Xu, M. Li, R. Liu, *et al.*, "Optical coherence tomography evaluation of vertebrobasilar artery stenosis: case series and literature review," *Journal of NeuroInterventional Surgery*, vol. 12, pp. 809–813, 2020.

[34] T. Kume, T. Akasaka, T. Kawamoto, *et al.*, "Assessment of coronary arterial thrombus by optical coherence tomography," *The American Journal of Cardiology*, vol. 97, pp. 1713–1717, 2006.

[35] C. R. Chu, A. Williams, D. Tolliver, C. K. Kwoh, S. Bruno III, and J. J. Irrgang, "Clinical optical coherence tomography of early articular cartilage degeneration in patients with degenerative meniscal tears," *Arthritis & Rheumatism*, vol. 62, pp. 1412–1420, 2010.

[36] K. Zheng, S. D. Martin, C. H. Rashidifard, B. Liu, and M. E. Brezinski, "*In vivo* micron-scale arthroscopic imaging of human knee osteoarthritis with optical coherence tomography: comparison with magnetic resonance imaging and arthroscopy," *American Journal of Orthopedics*, vol. 39, pp. 122–125, 2010.

[37] H. R. Djalilian, J. Ridgway, A. S. Majestic Tam, Z. Chen, and B. J. F. Wong, "Imaging the human tympanic membrane using optical coherence tomography *in vivo*," *Otology & Neurotology*, vol. 29, pp. 1091–1094, 2008.

[38] B. J. F. Wong, R. P. Jackson, S. Guo, *et al.*, "*In vivo* optical coherence tomography of the human larynx: normative and benign pathology in 82 patients," *The Laryngoscope*, vol. 115, pp. 1904–1911, 2005.

[39] K. Lueerssen, H. Wisweh, M. Ptok, and H. Lubatschowski, "Optical characterization of vocal folds by OCT-based laryngoscopy," in *Photonic Therapeutics and Diagnostics III*, International Society for Optics and Photonics, vol. 6424, SPIE, 2007, 64241O.

[40] U. Mahmood, J. Ridgway, R. Jackson, *et al.*, "*In vivo* optical coherence tomography of the nasal mucosa," *American Journal of Rhinology*, vol. 20, pp. 155–159, 2006.

[41] B. E. Bouma, G. J. Tearney, C. C. Compton, and N. S. Nishioka, "High resolution imaging of the human esophagus *in vivo* using optical coherence tomography," *Gastrointestinal Endoscopy*, vol. 51, pp. 467–474, 2000.

[42] M. V. Sivak Jr, K. Kobayashi, J. A. Izatt, *et al.*, "High resolution endoscopic imaging of the GI tract using optical coherence tomography," *Gastrointestinal Endoscopy*, vol. 51, pp. 474–479, 2000.

[43] M. Arvanitakis, L. Hookey, G. Tessier, *et al.*, "Intraductal optical coherence tomography during endoscopic retrograde cholangiopancreatography for investigation of biliary strictures," *Endoscopy*, vol. 41, pp. 696–701, 2009.

[44] P. A. Testoni, A. Mariani, B. Mangiavillano, P. G. Arcidiacono, S. Di Pietro, and E. Masci, "Intraductal optical coherence tomography for investigating main pancreatic duct strictures," *Official Journal of the American College of Gastroenterology*, vol. 102, pp. 269–274, 2007.

[45] J. Gallwas, L. Turk, K. Friese, and C. Dannecker, "Optical coherence tomography as a non-invasive imaging technique for preinvasive and invasive neoplasia of the uterine cervix," *Ultrasound in Obstetrics and Gynecology*, vol. 36, pp. 624–629, 2010.

[46] M. Y. Kirillin, N. M. Shakhova, O. G. Panteleeva, E. Yunusova, and E. Donchenko, "Criteria for pathology recognition in optical coherence tomography of fallopian tubes," *Journal of Biomedical Optics*, vol. 17, p. 081 413, 2012.

[47] L. P. Hariri, G. T. Bonnema, K. Schmidt, *et al.*, "Laparoscopic optical coherence tomography imaging of human ovarian cancer," *Gynecologic Oncology*, vol. 114, pp. 188–194, 2009.

[48] R. Wessels, D. M. De Bruin, D. J. Faber, *et al.*, "Optical coherence tomography in vulvar intraepithelial neoplasia," *Journal of Biomedical Optics*, vol. 17, p. 116 022, 2012.

[49] H. Schneider, K. J. Park, M. Häfer, *et al.*, "Dental applications of optical coherence tomography (OCT) in cariology," *Applied Sciences*, vol. 7, p. 472, 2017.

[50] Y. Shimada, M. Yoshiyama, J. Tagami, and Y. Sumi, "Evaluation of dental caries, tooth crack, and age-related changes in tooth structure using optical coherence tomography," *Japanese Dental Science Review*, vol. 56, pp. 109–118, 2020.

[51] L. O. Fernandes, C. Mota, L. S. de Melo, M. da Costa Soares, D. da Silva Feitosa, and A. S. Gomes, "*In vivo* assessment of periodontal structures and measurement of gingival sulcus with optical coherence tomography: a pilot study," *Journal of Biophotonics*, vol. 10, pp. 862–869, 2017.

[52] J. W. Goodman, *Speckle phenomena in optics: theory and applications*. SPIE, 2007.

[53] E. Jakeman and P. N. Pusey, "Significance of K distributions in scattering experiments," *Physical Review Letters*, vol. 40, pp. 546–550, 1978.

[54] J. W. Goodman, "Statistical properties of laser speckle patterns," in *Laser speckle and related phenomena*, J. C. Dainty, Ed., Springer, 1975, pp. 9–75.

[55] C. Forbes, M. Evans, N. Hastings, and B. Peacock, *Statistical distributions*. John Wiley and Sons Ltd, 2011.

[56] B. Karamata, K. Hassler, M. Laubscher, and T. Lasser, "Speckle statistics in optical coherence tomography," *Journal of the Optical Society of America A*, vol. 22, pp. 593–596, 2005.

[57] G. R. Ge, J. P. Rolland, and K. J. Parker, "Speckle statistics of biological tissues in optical coherence tomography," *Biomedical Optics Express*, vol. 12, pp. 4179–4191, 2021.

[58] I. A. Popov, N. V. Sidorovsky, and L. M. Veselov, "Experimental study of intensity probability density function in the speckle pattern formed by a small number of scatterers," *Optics Communications*, vol. 97, pp. 304–306, 1993.

[59] E. Jakeman, "Speckle statistics with a small number of scatterers," *Optical Engineering*, vol. 23, pp. 453–461, 1984.

[60] A. Weatherbee, M. Sugita, K. Bizheva, I. Popov, and A. Vitkin, "Probability density function formalism for optical coherence tomography signal: a controlled phantom study," *Optics Letters*, vol. 41, pp. 2727–2730, 2016.

[61] M. Sugita, A. Weatherbee, K. Bizheva, I. Popov, and A. Vitkin, "Analysis of scattering statistics and governing distribution functions in optical coherence tomography," *Biomedical Optics Express*, vol. 7, pp. 2551–2564, 2016.

[62] E. Jakeman and P. Pusey, "A model for non-Rayleigh sea echo," *IEEE Transactions on Antennas and Propagation*, vol. 24, pp. 806–814, 1976.

[63] M. Almasian, T. G. Van Leeuwen, and D. J. Faber, "OCT amplitude and speckle statistics of discrete random media," *Scientific Reports*, vol. 7, pp. 1–11, 2017.

[64] J. Uozumi and T. Asakura, "First-order probability density function of the laser speckle phase," *Optical and Quantum Electronics*, vol. 12, pp. 477–494, 1980.

[65] Q. Wang, "Discussion on the fully developed speckle field," *Optik*, vol. 124, pp. 2948–2950, 2013.

[66] V. Demidov, L. A. Matveev, O. Demidova, A. L. Matveyev, V. Y. Zaitsev, and I. A. Vitkin, "Analysis of low-scattering regions in optical coherence tomography: Applications to neurography and lymphangiography," *Biomedical Optics Express*, vol. 10, pp. 4207–4219, 2019.

[67] T. B. Dubose, D. Cunefare, E. Cole, P. Milanfar, J. A. Izatt, and S. Farsiu, "Statistical models of signal and noise and fundamental limits of segmentation accuracy in retinal optical coherence tomography," *IEEE Transactions on Medical Imaging*, vol. 37, pp. 1978–1988, 2017.

[68] M. G. Sowa, D. P. Popescu, J. Friesen, M. D. Hewko, and L. P. Choo-Smith, "A comparison of methods using optical coherence tomography to detect demineralized regions in teeth," *Journal of Biophotonics*, vol. 4, pp. 814–823, 2011.

[69] N. M. Grzywacz, J. De Juan, C. Ferrone, *et al.*, "Statistics of optical coherence tomography data from human retina," *IEEE Transactions on Medical Imaging*, vol. 29, pp. 1224–1237, 2010.

[70] M. Y. Kirillin, G. Farhat, E. A. Sergeeva, M. C. Kolios, and A. Vitkin, "Speckle statistics in OCT images: Monte Carlo simulations and experimental studies," *Optics Letters*, vol. 39, pp. 3472–3475, 2014.

[71] A. A. Lindenmaier, L. Conroy, G. Farhat, R. S. DaCosta, C. Flueraru, and I. A. Vitkin, "Texture analysis of optical coherence tomography speckle for characterizing biological tissues *in vivo*," *Optics Letters*, vol. 38, pp. 1280–1282, 2013.

[72] D. A. Jesus, M. Majewska, P. Krzyzanowska-Berkowska, and D. R. Iskander, "Influence of eye biometrics and corneal microstructure on noncontact tonometry," *PLoS One*, vol. 12, e0177180, 2017.

[73] S. Seevaratnam, A. Bains, M. Farid, G. Farhat, and B. A. Standish, "Quantifying temperature changes in tissue-mimicking fluid phantoms using optical coherence tomography and envelope statistics," in *Optical Fibers and Sensors for Medical Diagnostics and Treatment Applications XIV*, SPIE, vol. 8938, 2014, pp. 134–143.

[74] K. J. Parker and S. S. Poul, "Burr, Lomax, Pareto, and logistic distributions from ultrasound speckle," *Ultrasonic Imaging*, vol. 42, pp. 203–212, 2020.

[75] Z. Li, H. Li, Y. He, and C. Shoudong, "Experimental correlation of OCT speckle contrast ratio with the detectable depth and scattering coefficient of the sample," *Advances in Biomedical Photonics and Imaging*, pp. 306–308, 2008.

[76] Z. Li, H. Li, Y. He, C. Shoudong, and S. Xie, "A model of speckle contrast in optical coherence tomography for characterizing the scattering coefficient of homogenous tissues," *Physics in Medicine and Biology*, vol. 53, pp. 5859–5866, 2008.

[77] P. Lee, W. Gao, and X. Zhang, "Speckle properties of the logarithmically transformed signal in optical coherence tomography," *Journal of the Optical Society of America A*, vol. 28, pp. 517–522, 2011.

[78] D. A. Jesus and D. R. Iskander, "Assessment of corneal properties based on statistical modeling of OCT speckle," *Biomedical Optics Express*, vol. 8, pp. 162–176, 2017.

[79] M. E. Danielewska, A. Antonczyk, D. A. Jesus, *et al.*, "Corneal optical coherence tomography speckle in crosslinked and untreated rabbit eyes in response to elevated intraocular pressure," *Translational Vision Science and Technology*, vol. 10, pp. 1–12, 2021.

[80] M. Sugita, R. A. Brown, I. Popov, and A. Vitkin, "K-distribution three dimensional mapping of biological tissues in optical coherence tomography," *Journal of Biophotonics*, vol. 11, e201700055, 2018.

[81] A. Mcheik, C. Tauber, H. Batatia, J. George, and J. M. Lagarde, "Speckle modelization in OCT images for skin layers segmentation," in *VISAPP International Conference on Computer Vision Theory and Applications*, 2008, pp. 347–350.

[82] M. Pircher, E. Götzinger, R. Leitgeb, A. F. Fercher, and C. K. Hitzenberger, "Speckle reduction in optical coherence tomography by frequency compounding," *Journal of Biomedical Optics*, vol. 8, pp. 565–569, 2003.

[83] K. W. Gossage, C. M. Smith, E. M. Kanter, *et al.*, "Texture analysis of speckle in optical coherence tomography images of tissue phantoms," *Physics in Medicine & Biology*, vol. 51, pp. 1563–1575, 2006.

[84] D. K. Kasaragod, Z. Lu, L. E. Smith, and S. J. Matcher, "Speckle texture analysis of optical coherence tomography images," in *Speckle 2010: Optical Metrology*, SPIE, vol. 7387, 2010, pp. 553–559.

[85] J. H. Krachmer, M. J. Mannis, and E. J. Holland, *Cornea. Fundamentals, diagnosis and management*. Elsevier, 2010.

[86] L. Spadea, G. Maraone, F. Verboschi, E. M. Vingolo, and D. Tognetto, "Effect of corneal light scatter on vision: a review of the literature," *International Journal of Ophthalmology*, vol. 9, pp. 459–464, 2016.

[87] D. W. DelMonte and T. Kim, "Anatomy and physiology of the cornea," *Journal of Cataract & Refractive Surgery*, vol. 37, pp. 588–598, 2011.

[88] D. E. Birk and R. L. Trelstad, "Extracellular compartments in matrix morphogenesis: collagen fibril, bundle, and lamellar formation by corneal fibroblasts," *The Journal of Cell Biology*, vol. 99, pp. 2024–2033, 1984.

[89] N. S. Malik, S. J. Moss, N. Ahmed, A. Furth, R. S. Wall, and K. M. Meek, "Ageing of the human corneal stroma: Structural and biochemical changes," *Biochimica et Biophysica Acta (BBA) — Molecular Basis of Disease*, vol. 1138, pp. 222–228, 1992.

[90] T. J. Freegard, "The physical basis of transparency of the normal cornea," *Eye*, vol. 11, pp. 465–471, 1997.

[91] H. S. Dua, L. A. Faraj, D. G. Said, T. Gray, and J. Lowe, "Human corneal anatomy redefined: a novel pre-Descemet's layer (Dua's layer)," *Ophthalmology*, vol. 120, pp. 1778–1785, 2013.

[92] S. Xiong, H. Gao, L. Qin, Y. G. Jia, and L. Ren, "Engineering topography: Effects on corneal cell behavior and integration into corneal tissue engineering," *Bioactive Materials*, vol. 4, pp. 293–302, 2019.

[93] S. Patel and L. Tutchenko, "The refractive index of the human cornea: a review," *Contact Lens and Anterior Eye*, vol. 42, pp. 575–580, 2019.

[94] D. Leonard and K. Meek, "Refractive indices of the collagen fibrils and extrafibrillar material of the corneal stroma," *Biophysical Journal*, vol. 72, pp. 1382–1387, 1997.

[95] D. M. Maurice, "The structure and transparency of the cornea," *The Journal of Physiology*, vol. 136, pp. 263–286, 1957.

[96] F. J. Ávila, M. C. Marcellán, and L. Remón, "On the relationship between corneal biomechanics, macrostructure, and optical properties," *Journal of Imaging*, vol. 7, p. 280, 2021.

[97] Q. Wu and A. T. Yeh, "Rabbit cornea microstructure response to changes in intraocular pressure visualized by using nonlinear optical microscopy," *Cornea*, vol. 27, pp. 202–208, 2008.

[98] J. Bell, S. Hayes, C. Whitford, *et al.*, "The hierarchical response of human corneal collagen to load," *Acta Biomaterialia*, vol. 65, pp. 216–225, 2018.

[99] J. Liu and X. He, "Corneal stiffness affects IOP elevation during rapid volume change in the eye," *Investigative Ophthalmology & Visual Science*, vol. 50, pp. 2224–2229, 2009.

[100] A. Elsheikh, B. Geraghty, P. Rama, M. Campanelli, and K. M. Meek, "Characterization of age-related variation in corneal biomechanical properties," *Journal of the Royal Society Interface*, vol. 7, pp. 1475–1485, 2010.

[101] A. Daxer, K. Misof, B. Grabner, A. Ettl, and P. Fratzl, "Collagen fibrils in human corneal stroma: structure and aging," *Investigative Ophthalmology & Visual Science*, vol. 39, pp. 644–647, 1998.

[102] A. Kanai and H. E. Kaufman, "Electron microscopic studies of corneal stroma: aging changes of collagen fibers," *Annals of Ophthalmology*, vol. 5, pp. 285–287, 1973.

[103] T. Zheng, Q. Le, J. Hong, and J. Xu, "Comparison of human corneal cell density by age and corneal location: an *in vivo* confocal microscopy study," *BMC Ophthalmology*, vol. 16, pp. 1–10, 2016.

[104] C. Gambato, E. Longhin, A. G. Catania, D. Lazzarini, R. Parrozzani, and E. Midena, "Aging and corneal layers: an *in vivo* corneal confocal microscopy study," *Graefe's Archive for Clinical and Experimental Ophthalmology*, vol. 253, pp. 267–275, 2015.

[105] M. Niemczyk, M. E. Danielewska, M. A. Kostyszak, D. Lewandowski, and D. R. Iskander, "The effect of intraocular pressure elevation and related ocular biometry changes on corneal OCT speckle distribution in porcine eyes," *PLoS One*, vol. 16, e0249213, 2021.

[106] M. M. Rogala, D. Lewandowski, J. Detyna, A. Antończyk, and M. E. Danielewska, "Corneal pulsation and biomechanics during induced ocular pulse. An *ex-vivo* pilot study," *PLoS One*, vol. 15, e0228920, 2020.

[107] I. Sanchez, R. Martin, F. Ussa, and I. Fernandez-Bueno, "The parameters of the porcine eyeball," *Graefe's Archive for Clinical and Experimental Ophthalmology*, vol. 249, pp. 475–482, 2011.

[108] R. S. Raghavan, "A method for estimating parameters of K-distributed clutter," *IEEE Transactions on Aerospace and Electronic Systems*, vol. 27, pp. 238–246, 1991.

[109] M. K. Okasha and M. Y. Matter, "On the three-parameter Burr type XII distribution and its application to heavy tailed lifetime data," *Journal of Advances in Mathematics*, vol. 10, pp. 3429–3442, 2015.

[110] T. K. Stanton, W. J. Lee, and K. Baik, "Echo statistics associated with discrete scatterers: a tutorial on physics-based methods," *The Journal of the Acoustical Society of America*, vol. 144, pp. 3124–3171, 2018.

[111] F. Ardianti, "Estimating parameter of Rayleigh distribution by using Maximum Likelihood method and Bayes method," in *IOP Conference Series: Materials Science and Engineering*, vol. 300, 2018, p. 012 036.

[112] A. W. van der Vaart, *Asymptotic statistics*. Cambridge University Press, 1998, ch. Empirical, pp. 265–290.

[113] B. W. Silverman, *Density estimation for statistics and data analysis*. Routledge, 2018.

[114] M. C. Jones, "Simple boundary correction for kernel density estimation," *Statistics and Computing*, vol. 3, pp. 135–146, 1993.

[115] H. Cramer, *Mathematical methods of statistics*. Asia Publishing House, 1946.

[116] F. J. Massey, "The Kolmogorov–Smirnov test for goodness of fit," *Journal of the American Statistical Association*, vol. 46, pp. 68–78, 1951.

[117] A. Gretton, K. M. Borgwardt, M. J. Rasch, B. Schölkopf, and A. Smola, "A kernel two-sample test," *Journal of Machine Learning Research*, vol. 13, pp. 723–773, 2012.

[118] N. Ehlers and J. Hjortdal, "Corneal thickness: measurement and implications," *Experimental Eye Research*, vol. 78, pp. 543–548, 2004.

[119] S. Mishima and B. O. Hedbys, "Measurement of corneal thickness with the haag-streit pachometer," *Archives of Ophthalmology*, vol. 80, pp. 710–713, 1968.

[120] G. Savini, K. Hoffer, and M. Carbonelli, "Anterior chamber and aqueous depth measurement in pseudophakic eyes: agreement between ultrasound biometry and Scheimpflug imaging," *Journal of Refractive Surgery*, vol. 29, pp. 121–125, 2013.

[121] V. Bhardwaj and G. P. Rajeshbhai, "Axial length, anterior chamber depth — a study in different age groups and refractive errors," *Journal of Clinical and Diagnostic Research*, vol. 7, pp. 2211–2212, 2013.

[122] A. Abass, J. Clamp, F. Bao, R. Ambrósio, and A. Elsheikh, "Non-orthogonal corneal astigmatism among normal and keratoconic Brazilian and Chinese populations," *Current Eye Research*, vol. 43, pp. 717–724, 2018.

[123] T. Olsen, "On the calculation of power from curvature of the cornea," *British Journal of Ophthalmology*, vol. 70, pp. 152–154, 1986.

[124] L. N. Thibos and D. Horner, "Power vector analysis of the optical outcome of refractive surgery," *Journal of Cataract & Refractive Surgery*, vol. 27, pp. 80–85, 2001.

[125] W. Harris, "Astigmatism," *Ophthalmic and Physiological Optics*, vol. 20, pp. 11–30, 2000.

[126] R. A. Armstrong, "When to use the Bonferroni correction," *Ophthalmic & Physiological Optics*, vol. 34, pp. 502–508, 2014.

[127] M. A. Bujang and N. Baharum, "Sample size guideline for correlation analysis," *World*, vol. 3, pp. 37–46, 2016.

[128] V. Y. Zaitsev, L. Matveev, A. Matveyev, G. Gelikonov, and V. Gelikonov, "A model for simulating speckle-pattern evolution based on close to reality procedures used in spectral-domain OCT," *Laser Physics Letters*, vol. 11, p. 105 601, 2014.

[129] V. S. Huzurbazar, "Probability distributions and orthogonal parameters," *Mathematical Proceedings of the Cambridge Philosophical Society*, vol. 46, pp. 281–284, 1950.

[130] A. Kazaili, S. Lawman, B. Geraghty, *et al.*, "Line-field optical coherence tomography as a tool for *in vitro* characterization of corneal biomechanics under physiological pressures," *Scientific Reports*, vol. 9, pp. 1–13, 2019.

[131] J. M. Vetter, S. Brueckner, M. Tubic-Grozdanis, U. Voßmerbäumer, N. Pfeiffer, and S. Kurz, "Modulation of central corneal thickness by various riboflavin eyedrop compositions in porcine corneas," *Journal of Cataract & Refractive Surgery*, vol. 38, pp. 525–532, 2012.

[132] S. A. Read, M. J. Collins, and D. R. Iskander, "Diurnal variation of axial length, intraocular pressure, and anterior eye biometrics," *Investigative Ophthalmology & Visual Science*, vol. 49, pp. 2911–2918, 2008.

[133] C. Leydolt, O. Findl, and W. Drexler, "Effects of change in intraocular pressure on axial eye length and lens position," *Eye*, vol. 22, pp. 657–661, 2008.

[134] T. M. Nguyen, J. F. Aubry, M. Fink, J. Bercoff, and M. Tanter, "*In vivo* evidence of porcine cornea anisotropy using supersonic shear wave imaging," *Investigative Ophthalmology & Visual Science*, vol. 55, pp. 7545–7552, 2014.

[135] B. K. Pierscionek, M. Asejczyk-Widlicka, and R. A. Schachar, "The effect of changing intraocular pressure on the corneal and scleral curvatures in the fresh porcine eye," *British Journal of Ophthalmology*, vol. 91, pp. 801–803, 2007.

[136] K. Wu, S. Li, A. Lo, *et al.*, "Micro-scale stiffness change of cornea tissues suffered from elevated intraocular pressure investigated by nanoindentation," *Soft Materials*, vol. 11, pp. 244–253, 2013.

[137] A. Benoit, G. Latour, S. K. Marie-Claire, and J. M. Allain, "Simultaneous microstructural and mechanical characterization of human corneas at increasing pressure," *Journal of the Mechanical Behavior of Biomedical Materials*, vol. 60, pp. 93–105, 2016.

[138] Z. D. Taylor, J. Garritano, S. Sung, *et al.*, "THz and mm-wave sensing of corneal tissue water content: electromagnetic modeling and analysis," *IEEE Transactions on Terahertz Science and Technology*, vol. 5, pp. 170–183, 2015.

[139] S. Kling, L. Remon, A. Pérez-Escudero, J. Merayo-Lloves, and S. Marcos, "Corneal biomechanical changes after collagen cross-linking from porcine eye inflation experiments," *Investigative Ophthalmology & Visual Science*, vol. 51, pp. 3961–3968, 2010.

[140] E. Pavlatos, H. Chen, K. Clayson, X. Pan, and J. Liu, "Imaging corneal biomechanical responses to ocular pulse using high-frequency ultrasound," *IEEE Transactions on Medical Imaging*, vol. 37, pp. 663–670, 2017.

[141] S. K. Subasinghe, K. C. Ogbuehi, L. Mitchell, and G. J. Dias, “Animal model with structural similarity to human corneal collagen fibrillar arrangement,” *Anatomical Science International*, vol. 96, pp. 286–293, 2021.

[142] D. Podkowinski, E. Sharian Varnousfaderani, C. Simader, *et al.*, “Impact of B-scan averaging on Spectralis optical coherence tomography image quality before and after cataract surgery,” *Journal of Ophthalmology*, vol. 2017, 2017.

[143] H. J. Malik, “Exact distribution of the product of independent generalized gamma variables with the same shape parameter,” *The Annals of Mathematical Statistics*, vol. 39, pp. 1751–1752, 1968.

[144] D. Zwillinger and A. Jeffrey, *Table of integrals, series, and products*. Elsevier, 2007.